THERMAL ENERGY TRANSPORT ACROSS ULTRAWIDE AND WIDE BANDGAP SEMICONDUCTOR INTERFACES

A Dissertation
Presented to
The Academic Faculty

by

Zhe Cheng

In Partial Fulfillment
of the Requirements for the Degree
Doctor of Philosophy in the
George W. Woodruff School of Mechanical Engineering

Georgia Institute of Technology
December 2019

THERMAL ENERGY TRANSPORT ACROSS ULTRAWIDE AND WIDE BANDGAP SEMICONDUCTOR INTERFACES

Approved by:

Dr. Samuel Graham, Advisor
School of Mechanical Engineering
Georgia Institute of Technology

Dr. Baratunde Cola, co-advisor
School of Mechanical Engineering
Georgia Institute of Technology

Dr. Ching Ping Wong
School of Materials Science and Engineering
Georgia Institute of Technology

Dr. Shannon Yee
School of Mechanical Engineering
Georgia Institute of Technology

Dr. Alan Doolittle
School of Electrical and Computer Engineering
Georgia Institute of Technology

Date Approved: November 7, 2019

To my family

ACKNOWLEDGEMENTS

I would like to thank Professors Samuel Graham and Baratunde Cola the most, who served as my doctoral co-advisors in Georgia Tech, for their tremendous support and encouragement. They are my role models with great passion, expertise, and hardworking work ethic which not only shaped my PhD research but also will have a lasting impact on my future career. I am very grateful to Dr. Graham for giving me large freedom on my research topic, sending me to Oak Ridge National Lab, and sending me to Nagoya University. Treating students as an equal with respect, trust, and patience, Dr. Graham is more than an advisor, but also a caring friend who is always approachable. Dr. Cola's tireless enthusiasm and full of energy to break through setbacks encouraged me significantly in my PhD research. I would also like to thank Prof. Ching Ping Wong, Prof. Shannon Yee, and Prof. Alan Doolittle for serving on my committee and for the interesting and inspiring discussions.

So many collaborators make this dissertation possible and ensure my success as a PhD student. First, I would like to thank Prof. Mark Goorsky for all the material characterization work from the DARPA diamond project to the Interface MURI project. Many thanks to the DARPA diamond project collaborators: Prof. Martin Kuball, Prof. Ken Goodson, Dr. Remaz Cheaito, Dr. Aditya Sood, Prof. Mehdi Asheghi, Dr. Firooz Faili; the Interface MURI collaborators: Prof. Alan Doolittle, Prof. Zhiting Tian, Prof. Asegun Henry, Prof. Patrick Hopkins, Prof. Tengfei Luo, Prof. Asif Khan, Prof. Tadatomo Suga, Dr. Marko Tadjer, Dr. Karl Hobart, Dr. Ginger Wheeler; the Ga_2O_3 MURI collaborators: Prof. Huili Grace Xing and Prof. Debdeep Jena, Prof. Jim Speck, Prof. Hongping Zhao,

Prof. Siddharth Ranjan, Dr. Yuewei Zhang. Special thanks to all the collaborators both listed here or not listed here for providing nice samples, simulation support, and interesting discussions. For my stay in Nagoya University, I would like to thank Prof. Hiroshi Amano for giving me the opportunity to stay in his group and the fruitful collaborations since then. I would also like to thank Prof. Shugo Nitta and Dr. Xu Yang for introducing me to their research and all the other members in the Amano group.

Further, I would like to thank Tom Bougher and Brian Foley for their mentoring, close collaboration and help on every part of my research during the early time of my PhD. I will never forget the days and nights in the five months Tom, Brian, Luke, and I aligned TDTR together during the DARPA diamond project and the one month Tom and I aligned Photoacoustic. I would like to thank Eric Tervo, Luke Yates, Jingjing Shi, Nick Hines, Mat Smith, and Erik Anderson for collaborations in different projects. Special thanks to all the members of Graham group, Cola Group, Yee Group, Doolittle Group, Vogel Group, Zhang Group, and Joshi Group, so many ideas and interesting discussions in the past four years! I would like to thank all my friends who keep me company for different times of my life.

Finally, I would especially thank my family. I could never have made it this far without their constant love and unconditional support.

TABLE OF CONTENTS

LIST OF TABLES

LIST OF FIGURES

LIST OF SYMBOLS AND ABBREVIATIONS

ABBREVIATIONS AND CHEMICAL FORMULAS

WBG	wide bandgap
UWBG	ultrawide bandgap
HEMT	High electron mobility transistor
IoT	Internet of Things
CVD	chemical vapor deposition
TBC	thermal boundary conductance
TBR	thermal boundary resistance
DOS	density of states
TDTR	time-domain thermoreflectance
FDTR	frequency-domain thermoreflectance
RF	Radio frequency
MBE	Molecular beam epitaxy
ALD	Atomic layer deposition
GaN	Gallium nitride
Ga_2O_3	Gallium oxide
SiC	Silicon carbide
AlN	Aluminum nitride
MD	molecular dynamics
PTTR	picosecond transient thermoreflectance
MD	molecular dynamics
AMM	acoustic mismatch model
DMM	diffusive mismatch model
MOCVD	metalorganic chemical vapor deposition
SAB	surface activated bonding
HR-STEM	high-resolution scanning transmission electron microscopy
EELS	electron energy loss spectroscopy

RMS	root-mean-square
RH	relative humidity
AFM	atomic force microscopy
FIB	focused ion beam
HPHT	high-pressure high-temperature
NEMD	non-equilibrium molecular-dynamics
XRD	X-ray diffraction
NCD	Nanocrystalline diamond
2DEG	two-dimensional electron gas

SYMBOLS

κ	Thermal conductivity
D	thermal diffusivity
ω_0	modulation frequency
R	Reflectance
T	Temperature
γ	bonding energy
S_i	sensitivity to parameter i
$-V_{in}/V_{out}$	TDTR signal
p_i	value of parameter i.
E_1 and E_2	Young's moduli
t_{w1} and t_{w2}	thickness of wafers
t_b	thickness of blade
L	crack length
D	phonon density of states
f_{BE}	Bose-Einstein distribution function
$\hbar$	the reduced Planck constant
ω	the phonon angular frequency

v	phonon group velocity
τ_{12}	transmission coefficient
θ	angle of incidence
M	phonon number of modes
S_p and S_{ref}	contact areas
L_t	top width
L_b	bottom width
h	height
C_v	volumetric heat capacity
n	the number of phonon branches
τ_{ph}	relaxation time
l_0	scattering length

SUMMARY

The development of ultrawide and wide bandgap semiconductors enables a variety of applications in power and RF electronics, including energy infrastructure, wireless communication, self-driving cars, and radar systems for defense. With the increasing power and frequency of these applications, Joule-heating induced hot-spots in the device channel degrade the device performance and reliability. Thermal management of these devices plays a very important role in achieving stable device operation and long lifetime, and correspondingly improving energy efficiency and reducing cost. The basic component, GaN HEMTs, is usually integrated with high thermal conductivity substrates such as SiC and CVD diamond to extract the generated heat. For instance, GaN is grown on SiC with an AlN transition layer. CVD diamond is grown on GaN with an interfacial dielectric layer. The AlN layer and the low quality of the GaN layer near the interface induces additional thermal resistance. The nanocrystalline nature of the CVD diamond near the GaN-diamond interface results in significantly reduced thermal conductivity and large thermal stress due to the high growth temperature and large thermal expansion coefficient mismatch. Additionally, great attention has been focused on β-Ga_2O_3 recently due to the potential of affordable large-area wafers for homo-epitaxial growth, large breakdown voltages, and its ultrawide bandgap. However, its thermal conductivity is more than one order of magnitude lower than the other wide bandgap semiconductors. A disproportionally small amount of work has been done to address the thermal issues compared to analogous demonstrations of related devices. The understanding of heat transport mechanisms in nanostructures and interfaces, solution to address the thermal management challenges are in demand.

The grand challenge of thermal management of power and RF electronics lies in placing the hot-spot area of GaN/AlGaN and Ga_2O_3 devices close to heat sinks or heat spreaders with small thermal resistance and low stress. Thermal boundary resistance accounts for a large or even dominant part of the total thermal resistance in these devices. This thesis studied the TBC of five technologically important interfaces: GaN-SiC, GaN-diamond, diamond-Si, $(Al_{0.1}Ga_{0.9})_2O_3$-Ga_2O_3, Ga_2O_3-diamond. (1) Instead of including a defective AlN transition layer between GaN and SiC in direct growth method, a room-temperature surface-activated bonding technique is used to integrate GaN with SiC which brings high-quality GaN directly to the GaN-SiC interface. The measured GaN thermal conductivity is higher than the MBE-grown GaN on SiC substrates. Moreover, a very high GaN-SiC TBC is observed for the bonded GaN-SiC interface, especially for the annealed interface whose TBC (~230 $MWm^{-2}K^{-1}$) is close to the highest reported value of GaN-SiC interfaces in the literature. (2) Unlike the growth of CVD diamond on GaN which has a nucleation layer with low thermal conductivity, GaN is heterogeneously integrated with single crystalline diamond substrates with two modified room-temperature surface-activated bonding techniques for thermal management of GaN-on-diamond applications. The measured TBC of the bonded GaN-diamond interfaces is among the highest values reported in the literatures and is affected by the thickness of the interfacial bonding layer. Device modeling shows a relatively large GaN-diamond TBC value (>50 MW/m^2-K) achieved in this work could enable device designers to take full advantage of the high thermal conductivity of single crystalline diamond. (3) To improve the low TBC of diamond related interfaces because of the large phonon density of states mismatch of diamond and other semiconductors, the TBC at semiconductor-dielectric interfaces is

increased by nanoscale graphoepitaxy. By growing CVD diamond on nanopatterned silicon wafers, a general strategy is provided to significantly reduce the thermal resistance of both a diamond layer and diamond-substrate interface simultaneously. The diamond-silicon TBC could increase by 65% comparing with that of a flat diamond-silicon interface. (4) To understand the phonon transport mechanisms across β-$(Al_{0.1}Ga_{0.9})_2O_3$-Ga_2O_3 interfaces, temperature-dependent measurement on thermal conductivity of β-$(Al_{0.1}Ga_{0.9})_2O_3/Ga_2O_3$ superlattices is reported from 80 K to 480 K. Significantly reduced thermal conductivity is observed (5.7 times reduction) at room temperature comparing with bulk Ga_2O_3, which highlights the importance of thermal management of related devices. The estimated minimum TBC of β-$(Al_{0.1}Ga_{0.9})_2O_3/Ga_2O_3$ interfaces is found to be larger than the Ga_2O_3 maximum TBC, which shows that some phonons could transmit through several interfaces before scattering with other phonons or structural imperfections, as possible evidence of phonon coherence. (5) To develop cooling strategies of Ga_2O_3-related devices, Ga_2O_3 is integrated with single crystal diamond with exfoliation-transferring and ALD-growth. The Van der Waals Ga_2O_3-diamond TBC was measured to be 17 -1.7/+2.0 MW/m^2-K while the TBC calculated with a Landauer approach and DMM is 312 MW/m^2-K, which sheds light on the possible TBC which can be achieved. The measured TBC of the grown ultra-clean interface is 179 MW/m^2-K, about 10 times higher than TBC of a Van der Waals bonded Ga_2O_3-diamond interface, suggesting that covalent bonding facilitates interfacial heat transport better than Van der Waals interfacial bonding. Integration of Ga_2O_3 and single crystal diamond could be a solution to cool Ga_2O_3-related devices.

CHAPTER 1. INTRODUCTION

1.1 Background and Motivation

Compared to conventional semiconductors such as silicon, wide bandgap (WBG) semiconductors are semiconductor materials which have a large bandgap (2-4 eV) such as GaN and SiC.[1] Ultrawide bandgap (UWBG) semiconductors are semiconductor materials with bandgaps significantly wider than GaN (3.4 eV), for instance, AlN, AlGaN, Ga_2O_3, and diamond.[1-3] Wider bandgap semiconductors could result in smaller switching loss, lower specific on-resistance, and larger breakdown voltage.[4,5] As a result, related devices could achieve higher energy efficiency, smaller device size, and better reliability. Table 1.1 summarizes the basic material properties of several WBG and UWBG semiconductors[1,5] and Si is also included as a reference.

Table 1.1. Material properties of several semiconductors.[1,5]

		WBG	WBG	UWBG	UWBG	UWBG
Materials	Si	GaN	4H-SiC	AlGaN/AlN	β-Ga_2O_3	diamond
Bandgap (eV)	1.1	3.4	3.3	Up to6.0	4.9	5.5
κ (W/m-K)	149	200	370	Up to 320	11-27	>2000
Breakdown field (MV/cm)	0.3	3.3	2.5	Up to 15	8	10

By considering the dissipated heat energy in power electronics accounts for 5-10% of the world's electricity,[6] energy efficiency improvement and lifetime improvement resulted from reliability improvement could impact from the power electronics research and industry to the whole society significantly. Power electronics have wide applications, including modernized energy infrastructure, supercomputers and personal computers,

power converters and wireless charging, self-driving cars, renewable energy, cell phones, 5G base station and satellite communications, radar systems in defense, and so on.[4] These will facilitate the development of Internet of Things (IoT), big data collection, and smart cities. Wide bandgap power devices are more size-compact, more energy efficient and faster. To isolate a certain voltage, the amount of GaN is about ten times less than that of Si. The fast switching speed enables high-frequency applications with low delay time. The fast switching and low on-resistance improve the energy efficient of related devices.

One of the basic components of these power and RF electronics applications are GaN high electron mobility transistors (HEMTs). The development of HEMTs has much promise for creating advanced communication technologies.[1,4,7] However, as shown in Figure 1.1(a), localized power densities near the gate in GaN HEMTs can exceed 90 kW/cm^2, resulting in high channel temperatures that degrade device performance and reliability.[8,9] The localized Joule-heating results from the large voltage drop near the channel. The lifetime of GaN devices is strongly related to its channel temperature. Some simulation results of GaN-on-SiC devices showed that the lifetime of GaN devices could increase about ten times if the channel temperature decreases by 25 K.[10] This highlights the importance of thermal management of GaN devices. Figure 1.1(b) compares the power density of hot plate, rocket nozzle, sun surface and GaN/AlGaN HEMTs. The localized power density of GaN/AlGaN HEMTs could be more than ten times larger than that of sun surface.[9] The integration of high thermal conductivity substrates such as SiC and diamond into GaN HEMTs allows for effective heat spreading and the ability to keep these devices cool.[11-19]

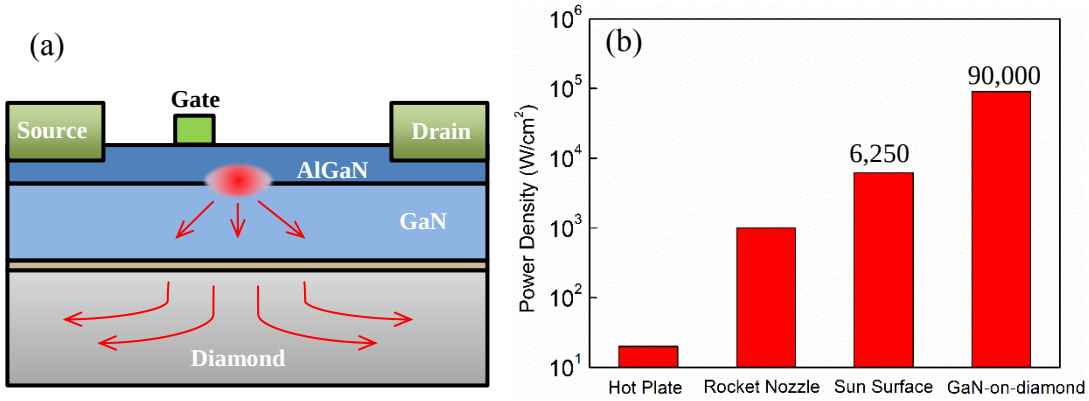

Figure 1.1. (a) Schematic diagram of HEMT structure and hotspot. (b) power density of hot plate, rocket nozzle, sun surface, and GaN/AlGaN HEMTs.[9]

GaN devices can be grown hetero-epitaxially on sapphire, SiC, Si or homo-epitaxially on GaN. Sapphire has very low thermal conductivity (33 W/m-K) so GaN-on-sapphire is not suitable for power electronics. GaN-on-Si devices have been developed because the low cost of the Silicon wafers. GaN wafers have higher thermal conductivity (~200 W/m-K) than Si (149 W/m-K) but are much more expensive. Due to the commercially available SiC wafers and high thermal conductivity of SiC, GaN is grown hetero-epitaxially on SiC substrates with a transition AlN layer. To cool GaN devices, hetero-epitaxy is used to bring in high thermal conductivity substrate, but it also brings in thermal boundary resistance (TBR, inverse of TBC) between GaN and substrates. This makes interfacial thermal resistance an inevitable obstacle for heat dissipation from the hot-spots to high thermal conductivity substrates. TBC is defined by a finite temperature drop (ΔT) across an interface for a given heat flux (Q): TBC=$Q/\Delta T$. For heterogeneous GaN interfaces, there always exists a temperature drop across GaN and substrates if the generated heat dissipates through substrates.

In terms of GaN-on-SiC devices, the AlN layer and the grown GaN near the interface have large numbers of defects and dislocations.[20] Even though the additional AlN layer, and the defects and dislocations reduce the TBC and the thermal conductivity of the GaN layer near the interface, the majority of the current GaN-on-SiC devices uses this structure.[21-23] While integrating diamond with GaN HEMTs is through the growth of the chemical vapor deposition (CVD) diamond onto the backside of the GaN buffer layer, an interfacial dielectric layer (e.g., SiN_x) is still required. The nanocrystalline nature of the CVD diamond near the GaN-diamond interface induces additional phonon scattering sources, resulting in significantly reduced and anisotropic thermal conductivity.[17,24-28] The high growth temperature (700-800 ^oC) leaves the devices with high stress level (~1GPa) after cooling down because of the large thermal expansion coefficient mismatch.[29-32] The stress limits the GaN quality by inducing cracking and wafer bow and affects the electrical performance of the devices, for instance, the formation of 2DEG.[33-35] Therefore, new heterogeneous integration techniques need to be developed to integrate GaN with high thermal conductivity substrates with high TBC and low stress.

When integrating diamond with other semiconductors, because of the unique physical structure of diamond, the thermal boundary resistance is very large due to the large mismatch in phonon density of states (DOS) across the interfaces. For instance, when integrating diamond on silicon, the TBR between diamond and silicon accounts for a large portion of the overall thermal resistance.[36,37] Reducing TBR, especially at diamond-substrate interface, is significantly important for a wide range of heterogeneous interfaces in semiconductors. For instance, if integrating GaN-on-diamond devices with silicon

substrates, the TBC of diamond-Si interfaces are very important for thermal dissipation of GaN devices. Here, diamond is used as a heat spreader.

Additionally, recent development of β-Ga_2O_3 growth technique (grown from the melt) makes it possible for large-scale commercially-available wafers.[5,38] It has emerged as a promising candidate for electronic applications similar to GaN due to its ultrawide bandgap and high breakdown voltage.[39,40] However, its thermal conductivity is at least one order of magnitude lower than other wide bandgap semiconductors, as shown in Table 1.1. The thermal conductivity of related nanostructures has not been studied before even though a significantly reduced thermal conductivity is expected.[40] The corresponding technical challenges of real-world applications lies in addressing this sensitive issue, including measuring and understanding heat transport mechanisms and looking for thermal management solutions. However, a disproportionally small amount of thermal studies have been reported compared to the effort to demonstrate Ga_2O_3 devices.[39]

1.2 Research Objectives

Based on the information outlined above, significant effort is still required in interface integration, measuring, understanding, and improving interfacial thermal transport across ultrawide and wide bandgap semiconductor interfaces for the thermal management of related power and RF devices to achieve size-compact, fast, and high-efficient devices with stable performance. The grand challenge of thermal management of power and RF electronics lies in reducing the thermal resistance between hot-spot area and heat sinks or heat spreaders with low stress. This thesis will discuss five technologically important interfaces: GaN-SiC, GaN-diamond, diamond-Si, $(Al_{0.1}Ga_{0.9})_2O_3$-Ga_2O_3, Ga_2O_3-

diamond. New heterogeneous integration techniques are used to integrate GaN devices with high thermal conductivity substrates such as SiC and single crystal diamond and new techniques are developed to improve TBC of diamond-related interfaces. Additionally, fundamental thermal transport mechanisms in Ga_2O_3-based nanostructures and interfaces are studied and solutions to solve the great challenges of thermal management for Ga_2O_3 power electronics are explored.

1.3 Dissertation Outline

Chapter 2 introduces the thermal characterization technique: time-domain thermoreflectance (TDTR), which is used to characterize the thermal properties of the materials and all interfaces studied in this dissertation. A historical review of TBC measurements are also included.

Chapter 3 discusses a method to achieve high TBC through surface-activated bonding of GaN-SiC interfaces. (**Reproduced with permission from reference below:** Fengwen Mu*, Zhe Cheng*, Jingjing Shi, Seongbin Shin, Bin Xu, Junichiro Shiomi, Samuel Graham, Tadatomo Suga. High Thermal Boundary Conductance across Bonded Heterogeneous GaN–SiC Interfaces, *ACS Appl. Mater. Interfaces*, 11, 36 (2019): 33428-33434. Copyright (2019) American Chemical Society.)

Chapter 4 provides a study of the excellent cooling performance for surface-activated bonded GaN-diamond interfaces. (**Reproduced with permission from reference below:** Zhe Cheng*, Fengwen Mu*, Luke Yates, Tadatomo Suga, Samuel Graham, High Interfacial Thermal Conductance across Room-Temperature Bonded GaN-

Diamond Interfaces for GaN-on-Diamond Devices, *ACS Appl. Mater. Interfaces*, 2019, in review, arXiv: 1909.01556 Copyright (2019) American Chemical Society.)

Chapter 5 provides a new method (nanoscale graphoepitaxy) to improve diamond-Si TBC significantly. (**Reproduced with permission from reference below:** Zhe Cheng, Tingyu Bai, Jingjing Shi, Tianli Feng, Yekan Wang, Matthew Mecklenburg, Chao Li, Karl D Hobart, Tatyana Feygelson, Marko J Tadjer, Bradford B Pate, Brian Foley, Luke Yates, Sokrates T Pantelides, Baratunde A Cola, Mark S Goorsky, Samuel Graham, Tunable Thermal Energy Transport across Diamond Membranes and Diamond-Si Interfaces by Nanoscale Graphoepitaxy, *ACS Appl. Mater. Interfaces*, 11, 20 (2019): 18517-18527 Copyright (2019) American Chemical Society.)

Chapter 6 provides an exploration of the phonon transport mechanisms in Ga_2O_3-related nanostructures and interfaces. (**Reproduced with permission from reference below:** Zhe Cheng, Nicholas Tanen, Celesta Chang, Jingjing Shi, Jonathan McCandless, David Muller, Debdeep Jena, Huili Grace Xing, Samuel Graham, Significantly Reduced Thermal Conductivity in β-$(Al_{0.1}Ga_{0.9})_2O_3/Ga_2O_3$ Superlattices, *Appl. Phys. Lett.* 115, 9, (2019): 092105 Copyright (2019) American Institute of Physics.)

Chapter 7 integrates Ga_2O_3 with single crystal diamond for thermal dissipation challenges of Ga_2O_3 power and RF devices. (**Reproduced with permission from references below:** Zhe Cheng, Luke Yates, Jingjing Shi, Marko J Tadjer, Karl D Hobart, Samuel Graham, Thermal conductance across β-Ga2O3-diamond van der Waals heterogeneous interfaces, APL Materials, 7, 3, (2019): 031118 Copyright (2019) authors. Zhe Cheng, Virginia D Wheeler, Tingyu Bai, Jingjing Shi, Marko J Tadjer, Tatyana

Feygelson, Karl D Hobart, Mark S Goorsky, Samuel Graham, Integration of Polycrystalline Ga_2O_3 on Diamond for Thermal Management *Appl. Phys. Lett.* In review (2019) Copyright (2019) American Institute of Physics.)

Chapter 8 concludes the work and provides an outlook.

CHAPTER 2. METROLOGY

2.1 TDTR System at Georgia Tech

TDTR is a pump-probe technique to measure the thermal properties of interfaces, nanostructured and bulk materials.[28,41] A picosecond laser is split into two beams (a pump beam and a probe beam). The pump beam chopped by an electro-optical modulator heats the sample surface periodically while a probe beam delayed by a mechanical moving stage detects the temperature variation of the sample surface via thermoreflectance.[42] The change in reflectance is related to the change in temperature of the sample surface: $\Delta R = \Delta T * \partial R/\partial T$. Here, $\partial R/\partial T$ is the thermoreflectance coefficient (unit:$^{o}C^{-1}$). The probe beam acts as a thermometer to measure the temperature variation induced by the pump beam. The sample surface is usually coated with a layer of Al (~ 80 nm) as transducer. The signal picked up by a photodetector and a lock-in amplifier is fit with an analytical heat transfer solution of the multi-layer sample structure to infer the unknown parameters. Here, the analytical heat transfer solution used to fit TDTR data is based on Fourier's law, similar to other thermal characterization techniques. By changing the modulation frequencies, the part of a sample probed by TDTR can be varied and provide good sensitivity to different unknown parameters. By measuring one spot on the sample with different frequencies, multiple thermophysical properties can be measured.[43,44] The TDTR system in Georgia Tech is a two-color system which uses a BiBo crystal to double the laser frequency from 800 nm to 400 nm.

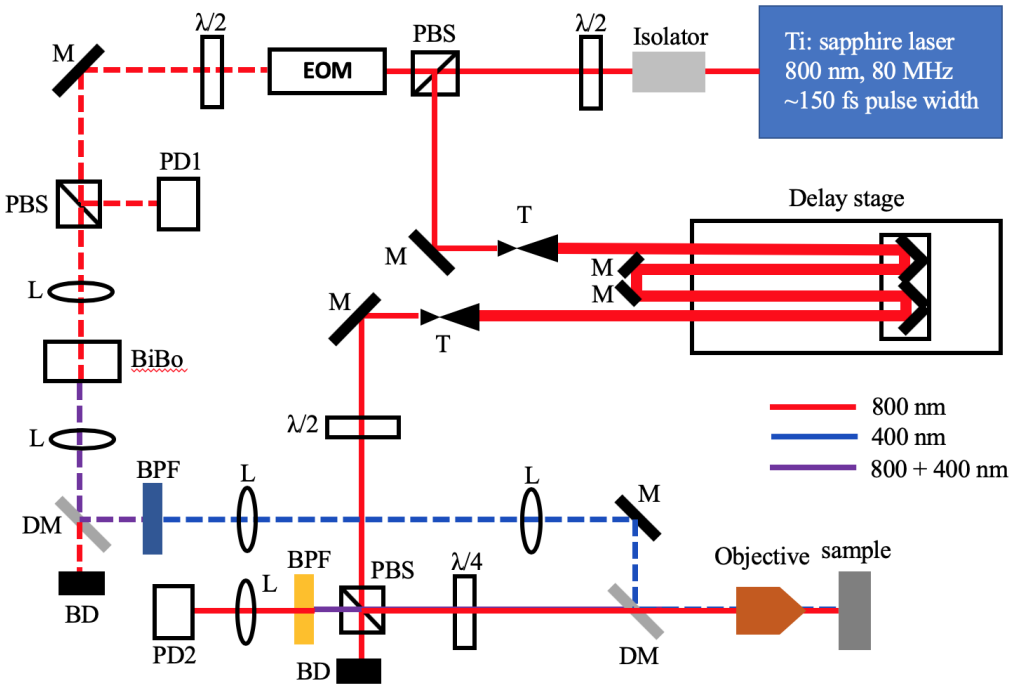

Figure 2.1. Schematic diagram of TDTR system at Georgia Tech.

Figure 2.1 shows the schematic diagram of a two-color TDTR system at Georgia Tech. PBS is polarizing beam splitter; EOM is electro-optical modulator; M is mirror; DM is dichroic mirror; BD is beam dump; λ/2 is half wave plate; λ/4 is quarter wave plate; BPF is band pass filter; PD1 is photodetector 1 (used to check waveform after EOM); PD2 is photodetector 2 (used to collect data); T is telescope or pair mirror; L is plano-convex lenses. 5X, 10X, 20X objective lenses are usually used. A list of the parts used in the system is as below: Ti: sapphire laser (Spectra Physics Mai Tai HP), optical isolator (ConOptics Model 714), EOM (ConOptics Model 160), function generator (Stanford Research Systems SSR850), photodetector (high-speed PIN diode, Thorlabs DET10A), high-speed low-noise electronic amplifier (Stanford Research Systems SR445a), lock-in amplifier (Stanford Research Systems SR844).

2.2 TDTR Measurements

In TDTR measurements, the Al thickness is usually determined by the picosecond acoustic technique. When the laser hits the sample surface, a strain-wave is generated and travels through the films along the cross-plane direction. A part of the wave is reflected back to the sample surface if hitting an interface and generates an echo in the TDTR signal. Figure 2.2 shows the echoes of an Al + GaN + SiC sample. The Al and GaN thicknesses are measured according to these echoes. The echoes indicate the time of strain waves travel from sample surface to a certain interface and bounce back. The film thickness can be obtained if the longitudinal acoustic phonon group velocity is known. This technique has been widely used in almost all the TDTR labs for decades. Excellent agreements have been achieved with thicknesses measured by other techniques such as atomic force microscopy (AFM) and TEM in the literature and this work.

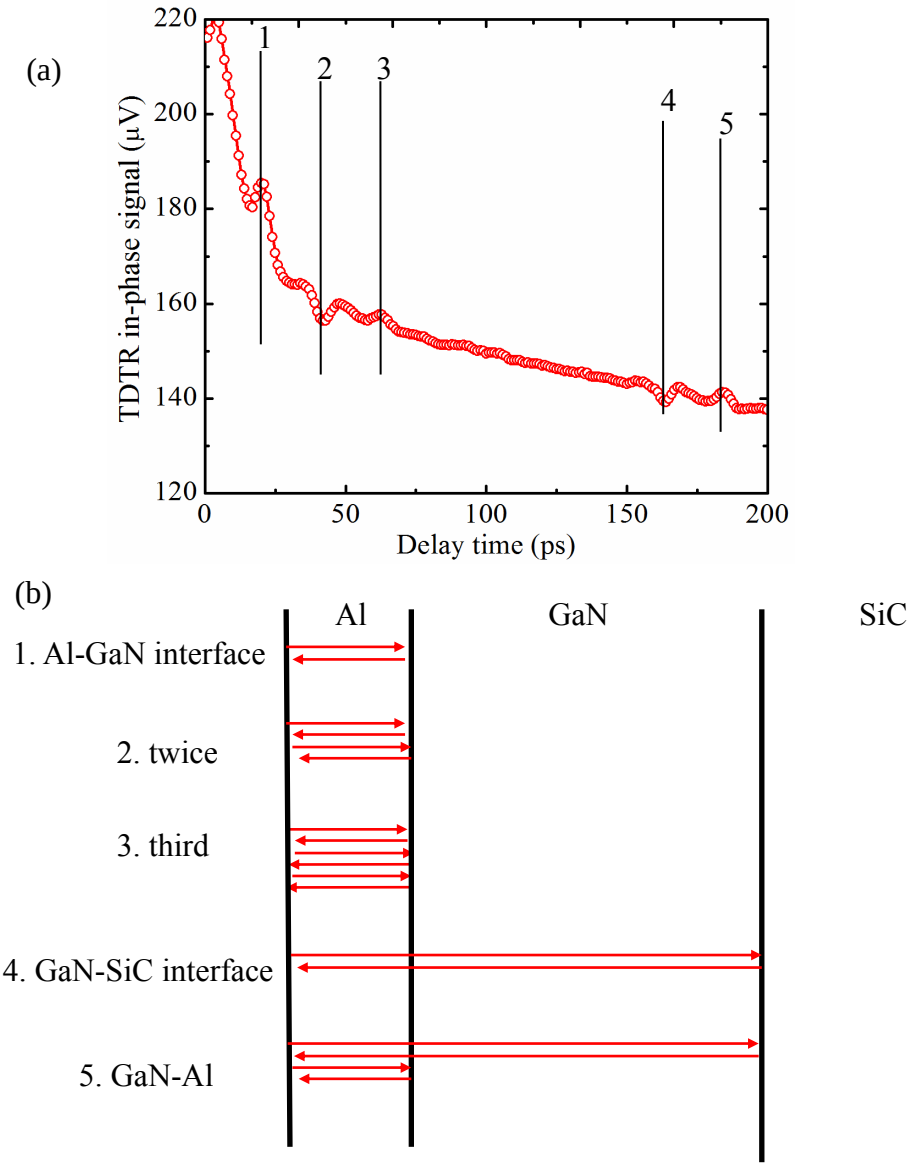

Figure 2.2. (a) Echoes from the picosecond acoustic technique and (b) what these echoes represent.

To perform accurate measurements, good TDTR sensitivity needs to be obtained. The definition of TDTR sensitivity is

$$S_i = \frac{\partial \ln(-V_{in}/V_{out})}{\partial \ln(p_i)}, \tag{2.1}$$

where, S_i is the sensitivity to parameter i, $-V_{in}/V_{out}$ is the TDTR signal, p_i is the value of parameter i. For normal single-frequency TDTR measurements on a two-layer sample (Al layer and sample layer), two free parameters are fitted (Al-sample TBC and sample thermal conductivity). But for three layer samples (Al layer, thin film, and substrate), there are three free or four parameters (Al-film TBC, film thermal conductivity, and film-substrate TBC/substrate thermal conductivity). One single frequency measurement is sometimes not enough to fit for three free parameters and multi-frequency measurements are needed.

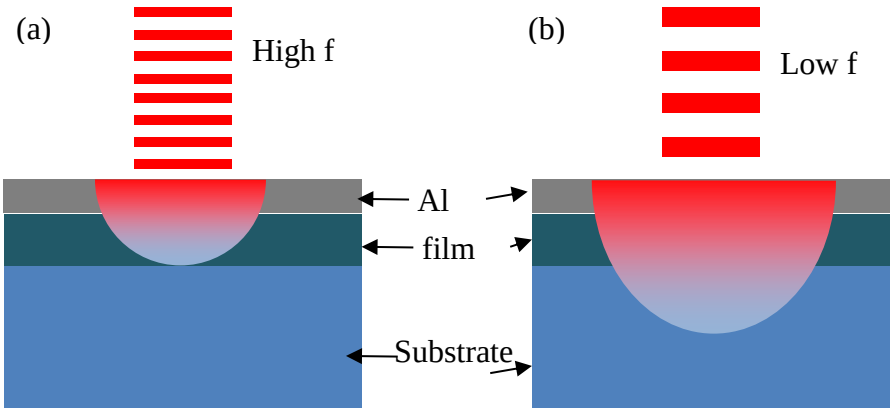

Figure 2.3. (a) high modulation frequency results in small thermal penetration depth; (b) low modulation frequency results in large thermal penetration depth.

The TDTR modulation frequency determines the thermal penetration depth into the samples, as shown in Figure 2.3. Low frequency TDTR measurements penetrate deeply into the samples, resulting in large sensitivity of the buried interface TBC (film-substrate TBC) or substrate thermal conductivity. High frequency TDTR measurements penetrate less deeply, resulting in large sensitivity of parameters close to the sample surface (large sensitivity of film thermal conductivity and small sensitivity of the film-substrate TBC and substrate thermal conductivity). Both frequencies have large sensitivity to Al-film TBC.

By using multi-frequency measurements on the same spot to fit for both film thermal conductivity and substrate thermal conductivity, accurate measurements on both parameters can be obtained. Figure 2.4 is an example of TDTR sensitivity on film thermal conductivity and substrate thermal conductivity with different modulation frequency (3.6 MHz and 8.8 MHz). Multi-frequency measurements enable accurate measurements on both film thermal conductivity and substrate thermal conductivity.

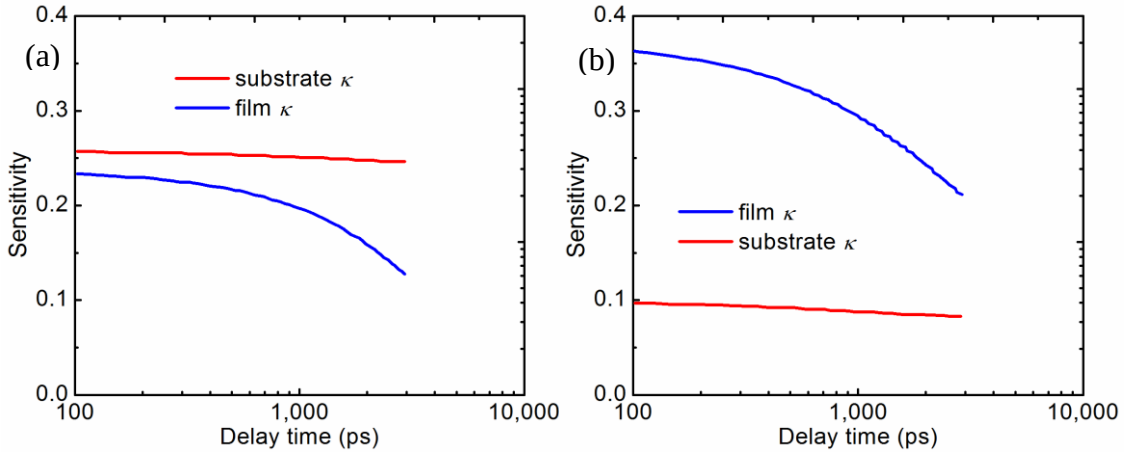

Figure 2.4. (a) sensitivity with modulation frequency of 3.6 MHz. (b) sensitivity with modulation frequency of 8.8 MHz. The sample structure is the superlattice on Ga_2O_3 substrate in Chapter 6.

The TDTR experimental data is fitted with an analytical solution to obtain unknown parameters. The step-by-step derivation of this analytical solution can be found in references.[41,42,45] In the analytical solution, each layer involves three parameters (thermal conductivity, volumetric heat capacity, thickness). The TBC of the interfaces are unknown. Most of the parameters can be found in literature such as heat capacity. The thickness of the substrate is not important because the substrate is thermally thick for TDTR

measurements. The volumetric heat capacity of Al is from literature and the thickness is measured by picosecond acoustic method during TDTR measurements.[28] A typical example of parameters used in the TDTR data fitting is shown in Table 2.1. The sample is the superlattice grown on a Ga_2O_3 substrate.

Table 2.1. Parameters used in the TDTR data fitting at room temperature.

	Th Cond	Volum Sp Heat	Thickness	TBC
	(W/m-K)	(J/ m³-K)	(μm)	(MW/m²-K)
Ga_2O_3	Fit	2.852e6	1000	Fit
superlattice	Fit	2.852e6	0.114	Fit
Al	150	2.43e6	0.085	0

Some error bars in this thesis are calculated by a Monte Carlo method.[46] This method accounts for all possible error sources in data fitting. The error of pump and probe beam spot sizes (10X objective) are ± 0.5 μm. The errors of heat capacity are ± 2%. The error bar of Al thermal conductivity is ± 10% and that of Al thickness is ± 3 nm. 1000 times are fitted for single frequency TDTR measurements and 500 times are fitted for multi-frequency TDTR measurements. An example is shown in Figure 2.5. 1000 times is fitted to calculate the error bar of parameter A. The 90% percentile confidence interval of A is 322-36/+41.

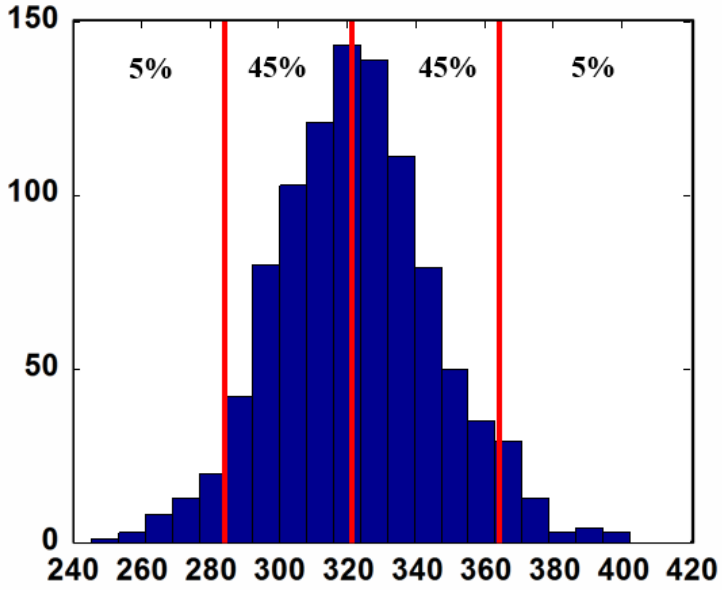

Figure 2.5. Monte Carlo error bar calculation with 1000 times of data fitting of parameter A. The 90% percentile confidence interval of A is 322-36/+41.

2.3 Historical Review of Experimentally Measured TBC

Figure 2.6 shows a historical review of experimentally measured TBC at room temperature. Kapitza observed a finite temperature drop across copper and liquid helium at extremely low temperatures in 1941.[47,48] Thermal boundary resistance across a heterogeneous interface is then named after Kapitza as Kapitza resistance. However, experimental measurements of TBC were not reported at higher temperature until 1980s and 1990s with the development of a transient hot-strip technique and a picosecond transient thermoreflectance (PTTR).[49-52] As shown in Figure 2.6, the database of measured TBC started to grow quickly when TDTR was developed. The red diamonds are TBC values of nonmetal-nonmetal interfaces while the blue square are TBC values of relatively clean metal-nonmetal interfaces including epitaxy-grown or cleaning steps were taken

before metal deposition such as an in situ high-temperature bake. The other TBC data of metal-nonmetal interfaces are shown as black circles. Additionally, the TBC of two metal-metal interfaces are shown in the inset. Most of these TBC data were measured by TDTR and a few were measured by frequency-domain thermoreflectance (FDTR), a modified version of TDTR, in Figure 2.6.

A summary of experimental techniques to measure TBC is discussed in a previous review paper by Monachon, *et al*.[53] The 1D reference bar technique and photoacoustic technique are usually used for characterizing very small TBC, for instance, thermal interface materials.[54-56] The 1D reference bar technique is a steady-state method which sandwiches the to-be-measured sample by two bars. By applying a temperature difference across the two bars and measuring the temperature gradients on the two bars, the temperature drop across the sample can be measured. Because the thermal conductivity of the two bars are known, the heat flux through the two bars are obtained and the thermal resistance can be obtained accordingly. The measured thermal resistance is an effective value of bar-sample contact thermal resistances and the thermal resistance of the sample itself. This method is suitable for samples whose thermal resistance is much larger than the bar-sample contact thermal resistance. Additionally, electro-thermal methods such as 3-Omega technique are sometimes sensitive to the TBC between the heating line and the substrates but primarily applied to measure thermal conductivity.[53,57-59] Generally speaking, 3-Omega technique is suitable for thermal conductivity measurements for relatively low thermal conductivity such as bulk polymer. The sensitivity of the metal-sample TBR is usually low. Therefore, the majority of the published TBC data were

measured by TDTR and the following discussions will focus on the main experimental technique: TDTR.

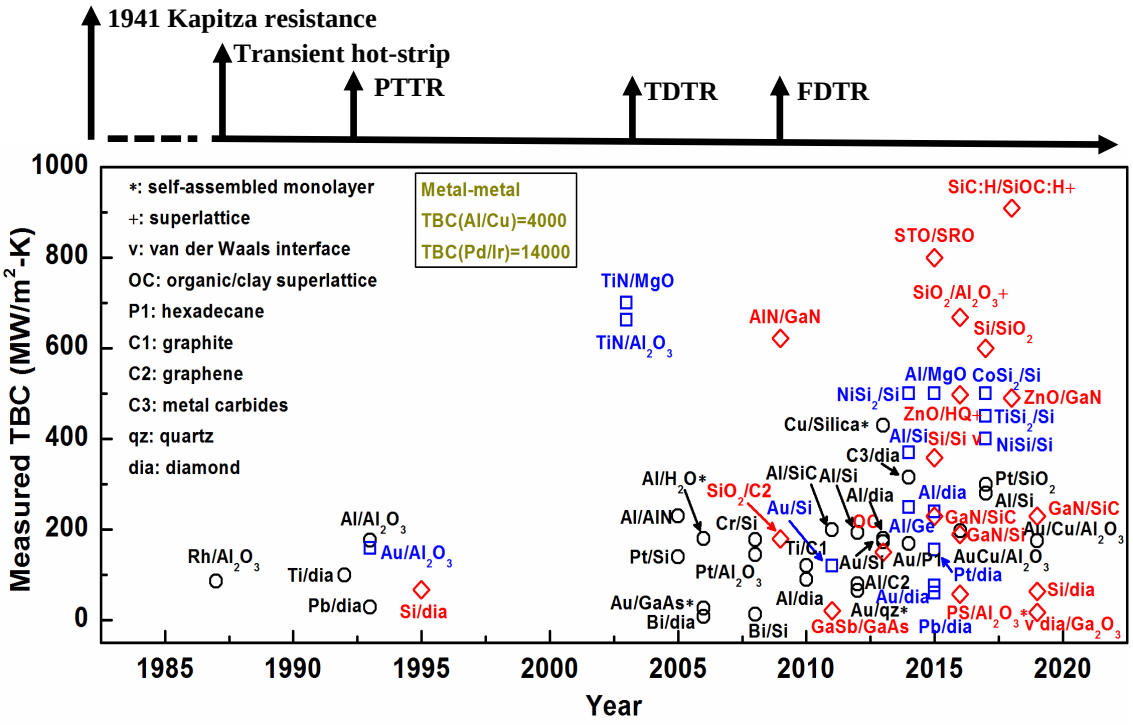

Figure 2.6. Literature review of experimentally measured TBC at room temperature. The red diamond are TBC values of nonmetal-nonmetal interfaces while the blue square are TBC values of relatively clean metal-nonmetal interfaces including epitaxy-grown or cleaning steps were taken before metal deposition such as an in situ high-temperature bake. The other TBC data of metal-nonmetal interfaces are shown as black circles. Additionally, the TBC of two metal-metal interfaces are shown in the inset. TBC data (red diamond) are from Si/diamond[37], SiO_2/graphene[60], AlN/GaN[61], GaSb/GaAs[62], organic/clay superlattice[63], STO/SRO[64], GaN/SiC[65], Si/Si van der Waals interface[66], SiO_2/Al_2O_3 superlattice[67], ZnO/HQ/ZnO superlattice[68], PS/sapphire with self-assembled monolayer (SAM)[69], GaN/Si[46], SiO_2/Si[70], ZnO/GaN[71], SiC:H/SiOC:H superlattice[72], bonded

GaN/SiC[73], Si/diamond[43], Ga_2O_3/diamond van der Waals interface[74]. TBC data (blue square) are from Au/Al_2O_3[51], TiN/Al_2O_3[75], TiN/MgO[75], Au/Si[76], Al/Ge[77], Al/Si[77], $NiSi_2$/Si[78], Al/MgO[64], Al/diamond[79], Pb/diamond[79], Pt/diamond[79], Au/diamond[79], NiSi/Si[80], $CoSi_2$/Si[80], $TiSi_2$/Si[80]. TBC data (black circle) are from Rh/Al_2O_3[49], Ti/diamond[81], Al/Al_2O_3[51], Pb/diamond[51], Al/AlN[82], Pt/Si[82], H_2O/Al with SAM[83], Au/GaAs with SAM[84], Bi/diamond[85], Cr/Si[86], Pt/Al_2O_3[87], Bi/Si[88], Ti/graphite[89], Al/diamond[90], Al/SiC[91], Al/Si[92], Al/graphene[93], Au/quartz with SAM[94], Cu/silica with SAM[95], Al/O/diamond[96], Au/Ti/Si[97], metal carbides/diamond[98], Au/hexadecane[99], AuCu/sapphire[100], Al/Si[101], SiO_2/Pt[70], Au/Cu/Al_2O_3[102]. The metal-metal TBC are from Al/Cu[103], and Pd/Ir[104].

2.4 Limitations of TDTR for TBC Measurements

TDTR and FDTR techniques are well-reviewed in references.[42,105] Here, the discussion is limited in the limitation of TDTR for TBC measurements. For TDTR measurements, a metal transducer is deposited on the sample surface. Therefore, TBC data of metal-nonmetal interfaces are much more than that of nonmetal-nonmetal interfaces, as shown in Figure 2.6. Al and Au are usually deposited by sputtering or e-beam deposition as transducer in TDTR or FDTR measurements so a large number of TBC values of the related interfaces were reported. Other metals are limited by the low absorption coefficient at the pump laser wavelength or low thermoreflectance coefficient at the probe laser wavelength. Metals sometimes react with samples and are affected by contamination, disordering, alloying, mixing, etching, and oxidation. These factors make most of the measured TBC values inconsistent and make it difficult to compare with modeling results. Moreover, this additional metal layer complicates the heat transfer problem in the thermal

measurements by introducing an additional unknown parameter (metal-sample TBC). So transducer-less TDTR methods are being developed to remove this metal layer. However, only the GaN top surface has been demonstrated as an example for now due to the complicated laser-materials interaction physics.[106]

For all the TBC data of nonmetal-nonmetal interfaces in Figure 2.6, the sample structures are at least three layers: metal transducer, nonmetal-1, and nonmetal-2. It is very challenging to measure these buried interfaces due to the limited thermal penetration depth (tens of nanometers to hundreds of nanometers, very few beyond μm, depending on material thermal properties). The measurements are affected by all the thermal properties of the upper layers. The metal/nonmetal-1 TBC and nonmetal-2 thermal conductivity need to be high, and the thermal resistance of the nonmetal-1 needs to be low, which facilitates heat penetrate across the nonmetal-1/nonmetal-2 interfaces and obtain good sensitivity of the TBC of this interface. This limits the sample structure that nonmetal-1 has to be thin and nonmetal-2 has high thermal conductivity so TBC values of nonmetal-nonmetal interfaces are disproportionally less reported than other interfaces. Even with good sample structure and material-pairs, the error bars of buried interfaces are much larger than non-buried interfaces, especially for high TBC interfaces.[71] Thermal penetration depth shows how far the periodical heating penetrates into the sample and usually calculated by $\sqrt{2D/\omega_0}$. Here, D is thermal diffusivity and ω_0 is the modulation frequency of the pump heating beam. However, a recent calculation shows that the real thermal penetration depth is much smaller than the values estimated by this formula, especially for low modulation frequencies.[107] The heating is difficult to penetrate across the buried interfaces and thus limits the ability to accurately measure some interfaces in a multilayered structure.[107]

For a thin nonmetal-1 layer, the phonon transport in this thin film is impacted by the upper and lower boundaries of the layer. The effective thermal conductivity of thin nonmetal-1 layer and TBC of metal/nonmetal-1 and nonmetal-1/nonmetal-2 are coupled and affected mutually.[108,109] All these mentioned above affect the TBC measurements of buried nonmetal-nonmetal interfaces which are based on classic diffusive heat transport assumptions. This problem also exists in the TBC extraction from superlattice effective thermal conductivity.[40,61,72] Coherent phonons across interfaces overestimate the TBC values. For future works, more measurements need to be performed on clean interfaces to enrich the TBC database, especially epitaxially grown interfaces for both metal-nonmetal and nonmetal-nonmetal interfaces. Experimental tools are also on demand to be developed to perform fast and accurate thermal characterization of buried interfaces.

CHAPTER 3. HIGH THERMAL BOUNDARY CONDUCTANCE ACROSS BONDED HETEROGENEOUS GAN-SIC INTERFACES

3.1 Introduction

GaN is an excellent wide bandgap semiconductor for power and RF electronics.[1] GaN-based HEMTs have the potential to be widely used in high-power and high-frequency electronics while their maximum output powers are limited by high channel temperature induced by near-junction Joule-heating, which degrades device performance and reliability.[2,3] Proper thermal management are the key to these devices for stable performance and long lifetime. Due to the high thermal conductivity and relatively small lattice mismatch with GaN, SiC is usually used as the substrates for high-power applications. However, the TBC between GaN and SiC limits the effectiveness for heat dissipation from GaN to SiC.[4] For this technically important interface, a number of experimental and simulation studies have been reported to understand thermal transport across the GaN-SiC interfaces.[4-12] The calculated TBC of GaN-SiC interface is close to 500 $MWm^{-2}K^{-1}$ by molecular dynamics (MD) simulations, twice as the experimentally measured GaN-SiC TBC.[4-9] Only a first-principle calculation matches with experimental values,[12] but acoustic mismatch model (AMM) and diffusive mismatch model (DMM) are used to calculate transmission in their work, which did not include the contribution of inelastic scatterings and cannot address the problem of local non-equilibrium phonon transport near the interface.[13] Therefore, a unified understanding of thermal transport across GaN-SiC interface is still lacking because of the complicated nature of interfacial heat transport. The complications arise due to interfacial layers such as AlN that are used

in between the GaN and SiC and the resulting quality of the GaN (e.g., dislocation density) that exists when GaN is grown onto the AlN. Both of these will add to the thermal resistance of the device structure near the interface. In general, what impact TBC are not only common factors such as temperature and phonon dispersion relations of the involved materials, but also interfacial bonding and local chemistry near the interfaces.[14,15]

The GaN-SiC interfaces reported in the literature are generally grown by MBE or metalorganic chemical vapor deposition (MOCVD) with an AlN nucleation layer, which is necessary to grow high-quality GaN due to the lattice mismatch between GaN and SiC. This AlN layer could serve as a phonon bridge to enhance TBC between GaN and SiC with a proper thickness because of the large phonon density of states mismatch of GaN and SiC but it has not been verified for the GaN-SiC interface.[16] Besides growing GaN on SiC, room-temperature surface activated bonding (SAB) is an important technique which has the potential to be widely used in the heterogeneous integration of semiconductor materials and in microelectronics packaging.[17,18] Compared with MBE, SAB is insensitive to lattice mismatch and can be performed at room temperature and at wafer-scale which results in small thermal stress. The bonded interfaces can have different interfacial bonds and local chemistry from directly-grown interfaces, and provide novel interfaces which cannot be grown through other techniques. This will enable and stimulate future studies of interfacial thermal transport mechanisms with such high degree of control over heterogeneous interfaces. Additionally, from an applied point of view, the thermal transport properties across these bonded interfaces are of great significance for real-world applications of electronics integration and packaging in which heat dissipation is always an important issue.[3]

In this work, template GaN is bonded with a 4H-SiC substrate followed by thinning it to several hundred nanometers for interfacial thermal transport characterization. TDTR is used to measure the thermal properties of GaN layer and GaN-SiC TBC for samples with and without post-annealing. The thermal conductivity of the GaN layer is compared with that of MBE-grown GaN. To understand the structure-thermal property relation, high-resolution scanning transmission electron microscopy (HR-STEM) and electron energy loss spectroscopy (EELS) are used to study the interface structure and local chemistry distribution.

3.2 Experimental Section

3.2.1 Sample Preparation

A Ga-face 2-μm GaN layer grown on a sapphire substrate was bonded to a Si-face, 3-inch, 4^{o} off, 4H-SiC wafer by a SAB machine at room temperature. The root-mean-square (RMS) surface roughness of the GaN and SiC surface is ~0.4 nm and ~0.3 nm, respectively. The employed SAB machine consists of a load-lock chamber and a processing-bonding chamber. The background vacuum of the processing-bonding chamber is kept as 5×10^{-6} Pa. Two kinds of Ar ion beam sources (Ar ion beam and Si-containing Ar ion beam) were setting in the processing-bonding chamber for surface activation. The Ar ion beam is for GaN surface and the Si-containing Ar ion beam is intentionally designed for SiC to suppress its Si preferential sputtering during surface activation.[110] Both of them have a power of 1.0 kV and 100 mA. After the surface activation for both GaN and SiC, two wafers were bonded at room temperature by contact with a pressure of 5 MPa for 300 s. The sapphire substrate of GaN template was removed from the bonded wafer by laser-

lift-off method using a laser with a wavelength of 248 nm, followed by a dicing process for multiple analyses.

To obtain good TDTR sensitivity for the buried GaN-SiC interface, the GaN layer was thinned to 300~600 nm thick by polishing. To study the effect of thermal annealing on TBC, one chip was annealed at 1273 K for 10 min in a flowing N_2 gas. After that, a ~70 nm Al layer was deposited on the samples by sputtering as TDTR transducer. Figure 3.1 shows the schematic diagram of the whole process. An additional bare SiC substrate with ~70 nm Al layer was also prepared for the thermal conductivity measurement of the SiC substrate.

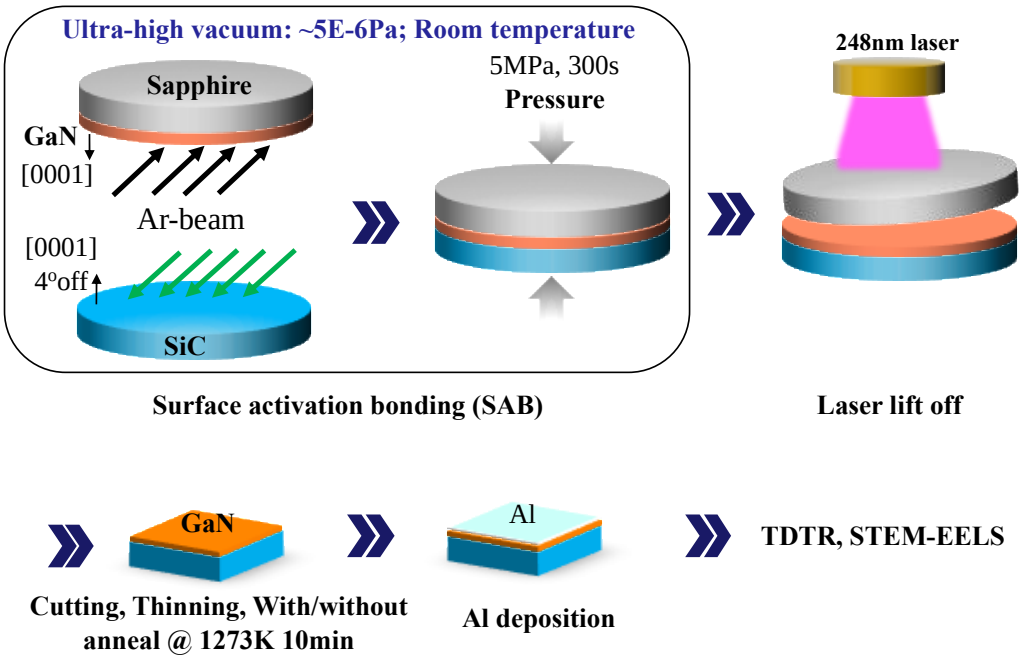

Figure 3.1. Schematic diagram of the whole experimental process.

3.2.2 Characterization Methods

Another bonded wafer obtained at the same condition was used for the evaluation of bonding energy by the "crack-opening" method.[111] The bonding energy (γ), which is the fracture energy of bonding interface, was evaluated by the "crack-opening" method and calculated by the following equation.[111]

$$\gamma = \frac{3t_b^2 E_1 t_{w1}^3 E_2 t_{w2}^3}{16L^4\left(E_1 t_{w1}^3 + E_2 t_{w2}^3\right)} \tag{3.1}$$

where E_1 and E_2 are the Young's moduli of SiC (530 GPa) and sapphire (345 GPa), t_{w1}=0.355 mm and t_{w2}=0.432 mm are the thickness of two wafers, t_b=0.1 mm is the thickness of the blade, and L is the crack length. In this evaluation, the bonded wafer is simplified to be a bonding between sapphire and SiC, since the thickness of GaN layer is neglected compared to that of sapphire substrate. This measurement was carried out at room temperature in air at a relative humidity (RH) of ~39.6%.

The measured thermal conductivity of the SiC substrate is used as input in the data fitting. The GaN thermal conductivity and GaN-SiC TBC are extracted from both of the as-bonded and annealed samples by TDTR with a 10X objective and a modulation frequency of 3.6 MHz. The picosecond acoustic technique is used to measure the local Al and GaN thicknesses. The measured thicknesses are confirmed with TEM and the results show excellent agreements. Cross-section TEM samples were prepared with a FEI Helios dual beam focused ion beam (FIB) system. The interface structures were characterized by an high-resolution STEM (Probe-corrected FEI Titan) and the interface composition was measured by EELS (Gatan Enfinium) with a step size of 0.2 nm. Since the Si-face of SiC

has 4^{o} off-axis towards <11-20>, to avoid interface overlap, the observation in this study is along <1-100> axis for both of SiC and GaN.

3.3 Results and Discussion

Figure 3.2(a) shows an image of the bonded wafer. Most area of the two wafers was well bonded except a few bonding voids resulting from particles and some edge parts. After a laser-lift-off process, the sapphire substrate can be removed and the GaN layer was transferred onto a SiC substrate, as shown in Figure 3.2(b). The bonding energy of ~1.3±0.3 Jm^{-2} is achieved. The bonding interface can withstand both of cutting and thinning process.

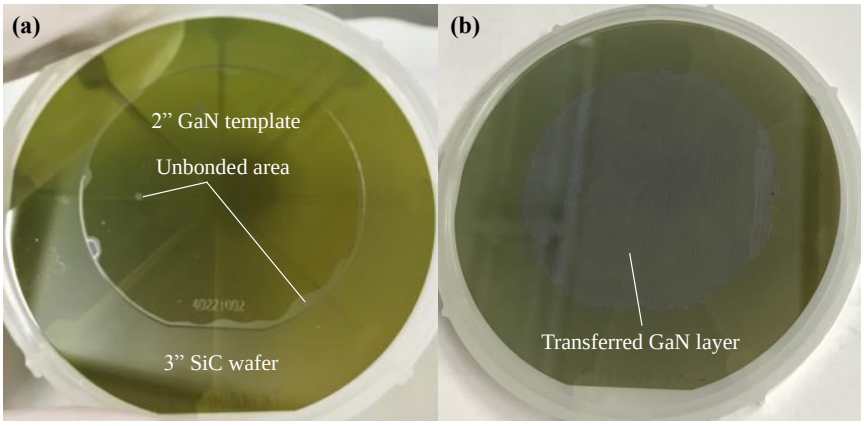

Figure 3.2. (a) Wafer bonded at room temperature by SAB method and (b) Bonded wafer after a laser lift-off process.

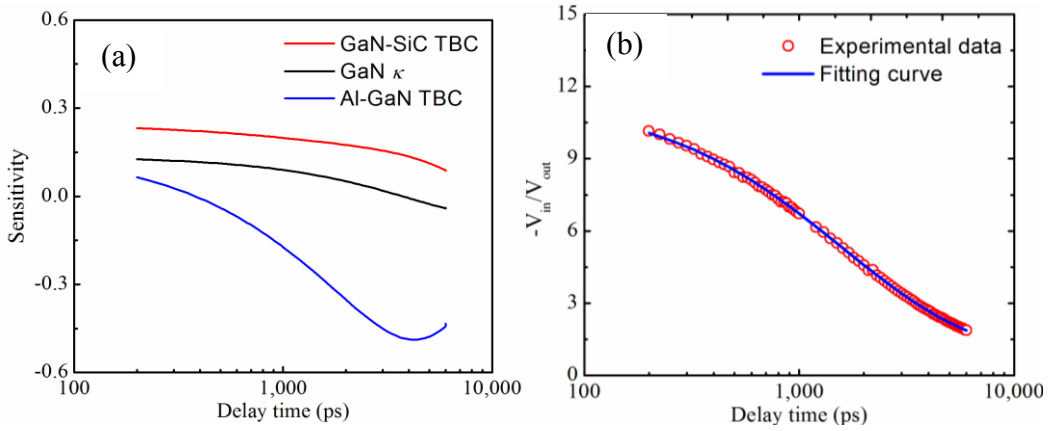

Figure 3.3. (a) TDTR sensitivity of each fitting parameter: Al-GaN TBC, GaN thermal conductivity and GaN-SiC TBC. (b) TDTR data fitting. The red circles are experimental data while the blue line is the analytical fitting curve.

The sensitivity of TDTR to each unknown parameter is shown in Figure 3.3(a). The definition of TDTR sensitivity is

$$S_i = \frac{\partial \ln(-V_{in}/V_{out})}{\partial \ln(p_i)} \tag{3.2}$$

Where S_i is the sensitivity to parameter i, $-V_{in}/V_{out}$ is the TDTR signal, p_i is the value of parameter i. The sensitivity of GaN-SiC TBC is very high, which is good for accurate measurements.[21] The thermal conductivity, density, and heat capacity of Al is 150 $Wm^{-1}K^{-1}$, 2700 kgm^{-3}, and 900 $Jkg^{-1}K^{-1}$.[22] The thermal conductivity of Al is calculated from electrical conductivity measurements and applying Wiedemann-Franz law. The density and heat capacity of GaN is 6150 kgm^{-3} and 430 $Jkg^{-1}K^{-1}$.[23] The thermal conductivity, density, and heat capacity of SiC is 331 $Wm^{-1}K^{-1}$, 3210 kgm^{-3}, and 660 $Jkg^{-1}K^{-1}$.[23] The thermal conductivity of the SiC substrate is measured from the bare SiC substrate by TDTR in this work, close to literature value.[4] The fitting of the experimental data and the analytical curve is excellent, as shown in Figure 3.3(b). Very good agreement between the

experimental data and the theoretical curve is achieved. The errors of GaN thermal conductivity and GaN-SiC TBC are calculated according to a Monte Carlo method which accounts for all possible parameters. The errors of the laser spot sizes are ±0.5 μm. The error of SiC thermal conductivity is ±5% while that of the heat capacity of Al, GaN, and SiC is ±2%. The thickness of Al is determined by both picosecond acoustic and TEM. The consistent results show a small error bar of ± 1 nm. The error of GaN layer is ± 3 nm based on the accuracy of picosecond acoustic technique. The error of Al thermal conductivity is ± 10%. Due to the small sensitivity of Al thermal conductivity, the effect on the TDTR measurements is very small.

Multiple spots are measured on the two bonded samples. Since the GaN thickness is not uniform after thinning, thickness dependence of GaN thermal conductivity and GaN-SiC TBC are obtained as shown in Figure 3.4. As shown in Figure 3.4(a), the measured GaN thermal conductivity is slightly larger than that of the MBE-grown GaN. The MBE-grown GaN is directly grown on SiC so the lattice mismatch leads to a relatively large amount of dislocations and defects in the thin GaN film near the interface. Phonons scattering with these structural imperfections lead to reduced mean free paths and correspondingly reduced thermal conductivity. In this work, commercially available template GaN is used in our bonding which has less structural imperfections in the top layer. Here, SAB provides a solution to avoid the integration of low-quality GaN into sample structures which cannot be avoided when direct growth with MOCVD is used. The SAB bonding method eliminates the growth of the AlN nucleartion layer and buffer GaN near the growth interface where high concentrations of defects and relatively low thermal conductivity are expected. Also, the GaN thermal conductivity increases with GaN film

thickness due to the phonon-boundary scattering. 80% of the thermal conductivity of bulk GaN is contributed by phonons with mean free paths from 100 nm to 3 μm.[24] Phonons with mean free path longer than the film thickness scatter with the film boundary. The film thickness limits the phonon mean free path and limits the thermal conductivity. For the ~600 nm and ~300 nm thick GaN films, their thermal conductivity are reduced to half and one third of the bulk value, respectively.

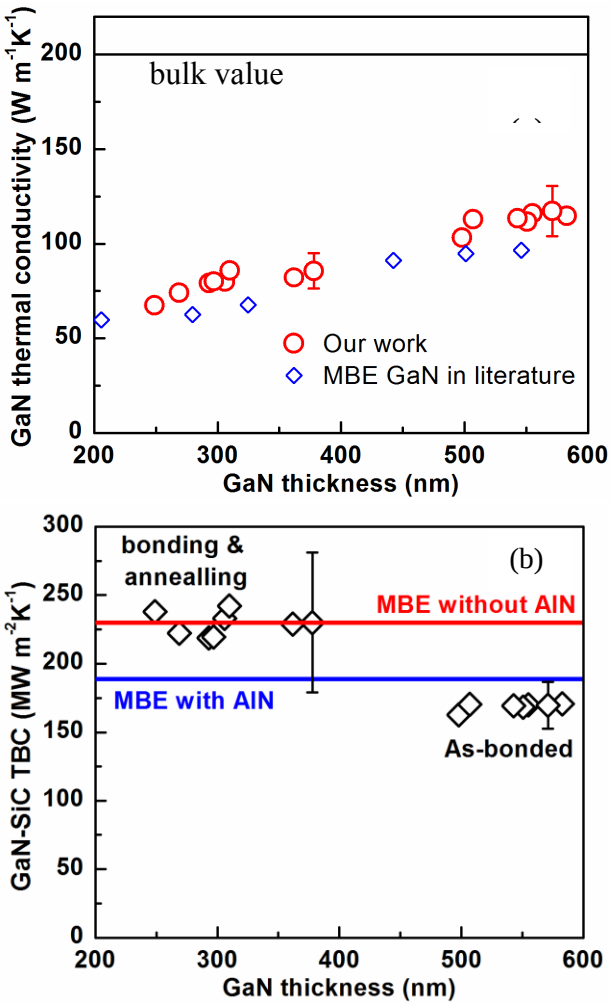

Figure 3.4. (a) Thickness-dependent thermal conductivity of the GaN thin films. The thermal conductivity of MBE-grown GaN is from literature.[25] The thermal conductivity of bulk GaN is from literature.[23] (b) thickness dependence of GaN-SiC TBC for annealed and

as-bonded samples. The TBC of MBE-grown GaN on SiC with and without a AlN layer are from literature.[4,9]

Figure 3.4(b) shows the measured TBC of both the as-bonded and annealed GaN-SiC interfaces. The measured TBC values do not change with GaN thickness as expected. The TBC of the as-bonded GaN-SiC interface is slightly lower than that of the GaN grown on SiC with an AlN layer. But after annealing at 1273 K for 10 mins, the TBC increases to about 230 $MWm^{-2}K^{-1}$, one of the highest reported GaN-SiC TBC values measured by experiments[4] as summarized in **Table** 3.**1**.

Table 3.1. Summary of experimentally measured GaN-SiC TBC in the literature and this work

Literature	AlN layer	Integration method	GaN-SiC TBC [$MWm^{-2}K^{-1}$]	Methods
Ref. 4	No	MBE	230 ±23.5	FDTR
Ref. 9	Yes	MBE	189	TDTR
Ref. 26	Yes	MOCVD	200 +29.4/-22.7	TDTR
Ref. 11	Yes	MOCVD	20-67	Raman
Ref. 10	Yes	MOCVD	30 ±4.5	Raman
This work	No	SAB	169 ±17	TDTR
This work	No	SAB with annealing	229 ±51	TDTR

It is notable that no large variation for the TBC values in the cm-scale samples is observed. 15 spots on the as-bonded and annealed samples were measured randomly. The variation of the measured TBC is within 10%. Since the small original thermal stress of the sample bonded at room temperature as well as the small thermal expansion mismatch between GaN and SiC, the TBC of the sample still shows uniform high values after experiencing high temperature annealing up to 1273 K. This facilitates real-world

applications, for example, homoepitaxy-growth of GaN on GaN-SiC bonded structure or device fabrications because epitaxy-growth and electrode formation are high temperature processes. Thus, these data show that very high TBC values along with higher thermal conductivity GaN in the vicinity of the interface can be obtained.

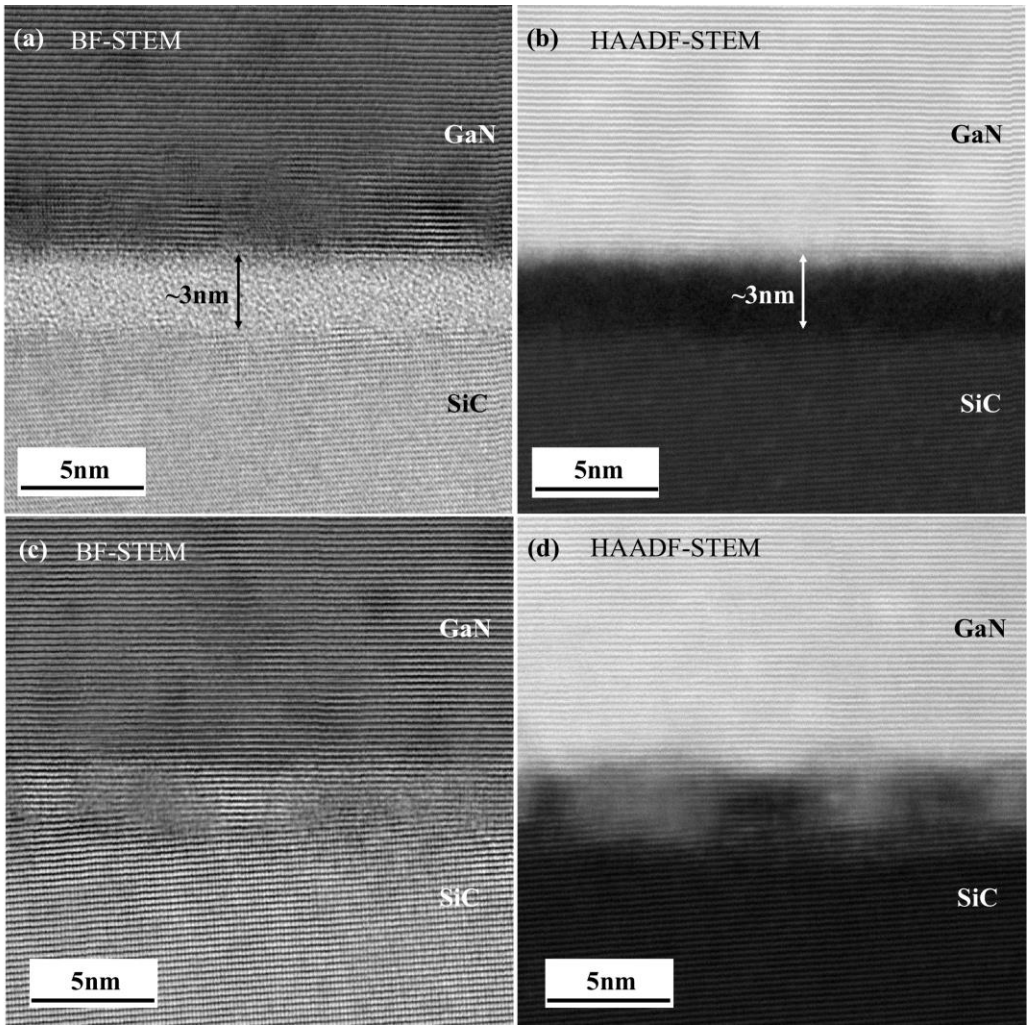

Figure 3.5. Cross-section HR-STEM images of GaN-SiC interface bonded at room temperature and after annealing at 1273 K: (a)(c) bright-field (BF) images and (b)(d) high-angle annular dark-field (HAADF) images.

To further understand the thermal property-structure relation, HR-STEM and EELS are used to study the GaN-SiC interfaces. The structure of the as-bonded GaN-SiC interfaces are shown in Figure 3.5(a). There exists a ~3 nm thick amorphous layer at the as-bonded interface, resulting from the ion beam bombardment during surface activation in the bonding process. The amorphous layer is mainly amorphous SiC, where amorphous GaN is hardly recognized. According to the blurred interface between amorphous GaN and amorphous SiC in the HAADF image of the as-bonded interface, as shown in Figure 3.5(b), the interfacial diffusion seems to happen even at room temperature. As confirmed by the high resolution EELS analysis in Figure 3.6(a), the amorphous SiC contains a Si-enriched layer, which is formed by the intentionally-designed Si-containing Ar ion beam. The Si-enrichment of the amorphous SiC is assumed to be helpful for the interfacial diffusion at room temperature, which is consistent with previous bonded interfaces of GaN-Si and GaN-SiC.[27,28] Both of the interfacial amorphous layer and interfacial mixing caused by diffusion may contribute the high TBC of the as-bonded interface.[29] Besides, a small amount of Ar (a couple of percent in atom composition) is only observed in the amorphous SiC layer, which derives from the Ar ion beam in the bonding process.[27] Some simulations show that the implanted Ar in the GaN side is possible to be ejected out.[30] Similar phenomena are also observed in bonded GaN-Si interface.[28] It is still an open question that how these trapped Ar atoms affect thermal transport across interface, especially with an amorphous interface layer where phonon gas model does not hold. Recent MD modeling results show that there exists an interface mode at heterogeneous Si-Ge interfaces.[31-33] The interface mode interacts with phonons in both sides of the interface, redistributes phonon modes and boosts the contribution of inelastic transport to TBC.[34]

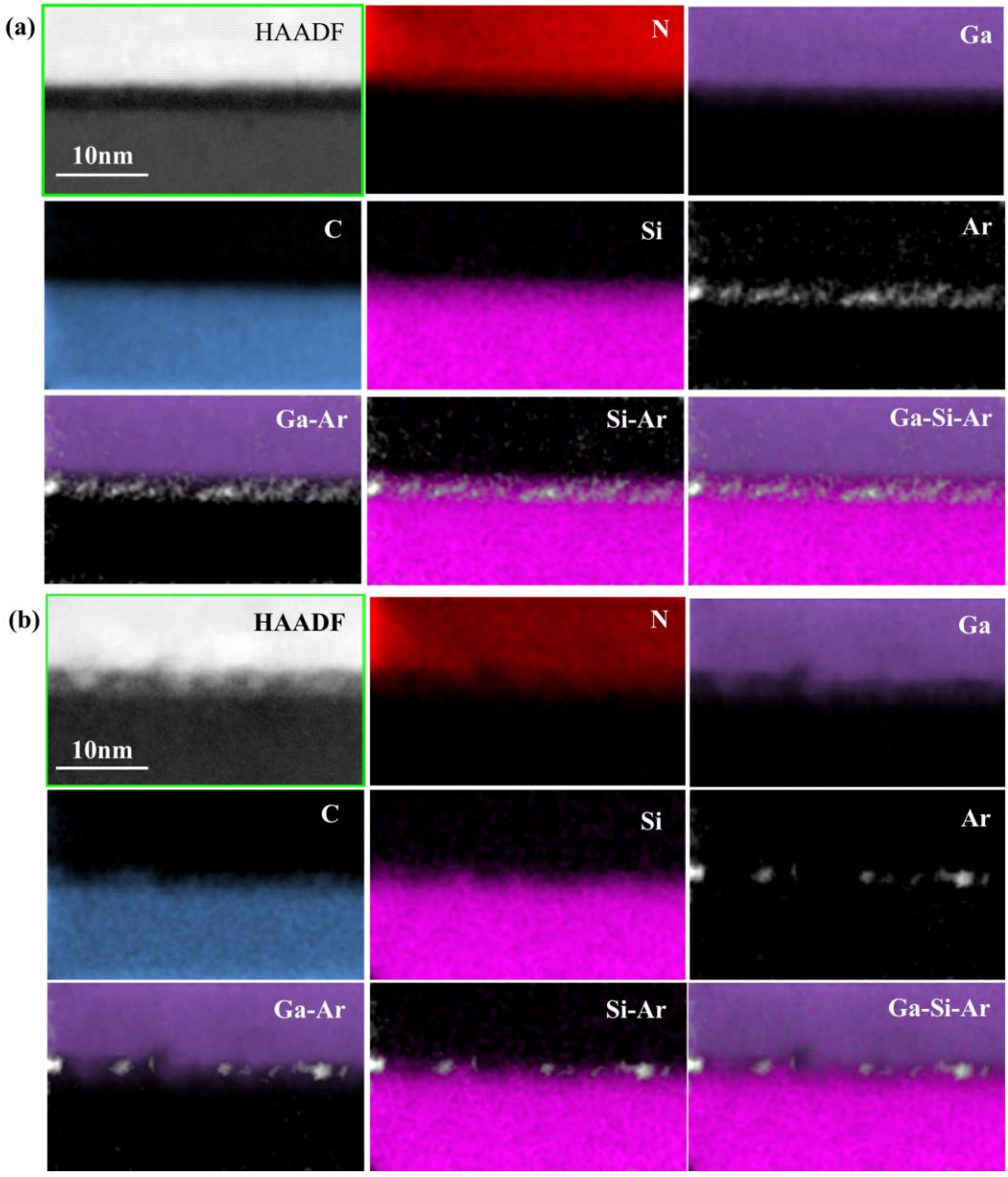

Figure 3.6. EELS mapping of GaN-SiC bonded interfaces: (a) at room temperature and (b) after annealing at 1273 K. The N, Ga, C, Si, and Ar maps are highlighted in red, purple, blue, pink, and white, respectively.

As a comparison, the TEM structure and EELS images of the annealed interface are shown in Figure 3.5(c-d) and Figure 3.6(b), respectively. The amorphous layer crystallizes during annealing and almost disappears in the TEM images. But some local

inhomogeneous structure and dislocations show up near the interface. This is possibly due to the non-uniform interfacial diffusion during annealing, as shown in Figure 3.5(d) and Figure 3.6(b). The trapped Ar atoms also redistribute and form islands at the interface but still in SiC side, as shown in the EELS images. An amorphous layer usually has very low thermal conductivity. After annealing, the measured TBC increases by 36%, to almost the same value as the TBC of directly-grown GaN on SiC. Here, this increase in TBC is attributed to the disappearance of the amorphous layer and the redistribution of the Ar atoms even though some modeling results show that amorphous interface increases TBC.[20,33] The GaN-SiC TBC by a Landauer approach with DMM is calculated as about 260 $MWm^{-2}K^{-1}$, close to the literature value.[12] If assuming the phonon transmission is unity (all the phonons in the GaN side transmit across the interface to the SiC), the radiation limit is determined as 367 MW/m^2K. This gives us an estimate of the upper limit of GaN-SiC TBC if inelastic scattering at the interface is not significant.

3.4 Conclusions

In this work, a GaN layer is bonded with a SiC substrate by a room temperature bonding method which brings high-quality GaN directly to the GaN-SiC interface, which facilitates thermal dissipation for devices. Moreover, a high GaN-SiC TBC is observed for the bonded GaN-SiC interface, especially for the annealed interface whose TBC (~230 $MWm^{-2}K^{-1}$) is close to the highest reported values in the literature. STEM and EELS results show that, for the as-bonded sample, there exists an interfacial amorphous layer and a small amount of trapped Ar atoms at the interface while the amorphous layer disappears and the Ar atoms redistribute after post-annealing. The TBC increase after annealing is attributed to the disappearance of the amorphous layer and the redistribution of the trapped Ar atoms.

Our work not only paves the way for thermal transport across bonded interfaces where bonding and local chemistry are tunable, which will enable the study of interfacial thermal transport mechanisms, but also impact real-world applications of semiconductor integration and packaging in which thermal dissipation always plays an important role.

CHAPTER 4. INTERFACIAL THERMAL CONDUCTANCE ACROSS ROOM-TEMPERATURE BONDED GAN-DIAMOND INTERFACES FOR GAN-ON-DIAMOND DEVICES

4.1 Introduction

With wide bandgap, high-breakdown electric field, and high carrier mobility, GaN has been used for high-power and high-frequency electronics applications such as wireless communication, satellite communication, and radar systems.[4] The maximum output power of GaN-based HEMTs is limited by the high channel temperature induced by localized Joule-heating, which degrades device performance and reliability.[12,112] Diamond has the highest thermal conductivity among natural materials and is of interest for integration with GaN to help dissipate the generated heat from the channel of GaN-based HEMTs.[12,113-115] Current techniques involve two ways to integrate GaN with diamond. One is direct growth of CVD diamond on GaN with a transition layer of dielectric material.[116] The nanocrystalline diamond near the nucleation interface has reduced thermal conductivity (tens of W/m-K) which could contribute to an additional thermal resistance of 10 m^2K/GW.[117] Combining with the GaN-diamond thermal boundary resistance, these near-hotspot thermal resistances have been shown to have a large impact on impeding the flow of heat from the device channels, especially for high frequency applications in which the thermal penetration depth is small.[14,15,28,43] The high growth temperature of the diamond also induces large residual stress in the GaN because of the mismatch of the coefficients of thermal expansion.[29,30] Stresses generated during the direct growth of diamond on GaN have been shown to vary, dependent upon GaN thickness, diamond growth temperature,

and the sacrificial carrier wafer[31,32]. Residual stresses greater than 1 GPa at the free surface of the GaN have been reported.[118] The elevated stress conditions in the GaN ultimately limit the total thickness and material quality of the GaN by inducing layer cracking and wafer bow, and impact the electrical performance of the device.[33-35,119] The aforementioned effects of elevated stress cause a significant reliability concern when considering the function and lifetime of a GaN device. Another method is high temperature bonding of GaN with diamond.[120,121] The GaN device is firstly grown on silicon substrates. Then the GaN device is transferred and bonded with a CVD diamond with an adhesion layer. The transfer and bonding processes are performed at elevated temperatures exceeding 700 ^{o}C.[121] The adhesion layer increases the thermal resistance of GaN-diamond interface, which offsets the effect of the high thermal conductivity of diamond substrates. The stress due to the different coefficients of thermal expansion results in wafer bow and warp, even fractures.[121] Even though some attempts have been made to bond GaN with diamond at lower temperatures[113,122], additional techniques to integrate GaN with diamond substrates are in demand to be developed to take full advantage of the high thermal conductivity of diamond without inducing additional stress resulting from high temperature processes.

In this work, two modified SAB techniques (one with Si nanolayer sputtering deposition and the other with Si-containing Ar ion beam) are used to bond GaN with diamond substrates with different interlayers at room temperature. TDTR is used to measure the thermal properties. Materials characterization such as HR-STEM and EELS are used to study the interface structure and chemistry to help elucidate the measured thermal properties. An analytical modeling for devices is performed to estimate the device cooling performance of these bonded interfaces.

4.2 Methods

4.2.1 Sample Preparation

Two single crystalline diamond (CVD diamond and HPHT diamond with size of 10 mm×10 mm and 3 mm×3 mm) are bonded to templated GaN films at room temperature. The GaN films are Ga-face ~2-μm GaN layer grown on sapphire substrates (~430 μm thick). The root-mean-square (RMS) surface roughness of the GaN and diamond surface is ~0.4 nm and ~0.3 nm, respectively. A modified SAB method with a sputtering-deposited Si nano-layer is used to bond the CVD diamond (Samp1) and a modified SAB method with Si-containing Ar ion beam is used to bond the HPHT diamond (Samp2). The detailed bonding process are similar to literature[110,123]. After bonding, the sapphire substrate was removed by a laser lift-off process. The GaN layer was polished to be thinner to obtain good TDTR sensitivity of the buried GaN-diamond interface. The GaN layer of Samp1 is thinned to ~700 nm, while the GaN layer of Samp2 is thinned to ~1.8 μm. After that, a ~70 nm Al layer was deposited on the samples by sputtering as TDTR transducer.

4.2.2 TDTR Measurements

The measured thermal conductivity of the diamond substrates are used as input in the data fitting of TDTR measurements on GaN-diamond interfaces. A 10X objective (pump radius: 9.7 μm; probe radius: 5.8 μm) is used with a modulation frequency of 2.2 MHz (Samp2) or 3.6 MHz (Samp1). The GaN layer of Samp2 is thicker than that of Samp1 so large thermal penetration depth is needed to penetrate through the GaN layer to obtain large TDTR sensitivity of the GaN-diamond TBC. Therefore, lower modulation frequency (2.2 MHz) is used for Samp2 to get larger thermal penetration depth. The heat capacity of

GaN is from literature.[124] Because of the thin thickness of the GaN layer of Samp1, the GaN thermal conductivity is not sensitive so the GaN thermal conductivity is fixed in the data fitting using literature values of similar GaN layer bonded on SiC.[21] The thermal conductivity and heat capacity of the Al transducer is from literature with similar Al films.[21] The picosecond acoustic technique is used to measure the local Al and GaN thicknesses.[21,125]

4.2.3 Materials Characterization

Cross-section TEM samples were prepared with a FEI Helios dual beam focused ion beam (FIB) system. The interface structures were characterized by a HR-STEM (Probe-corrected FEI Titan) and the interface composition was measured by EELS (Gatan Enfinium) with a step size of 0.2 nm. The observation in this study is along <11-20> axis of GaN.

4.3 Results and Discussion

In this work, GaN was bonded to diamond using a Si interlayer to aid in the chemical adhesion at the interface. The first sample, Samp1, is comprised of a thin layer of GaN (~700 nm) bonded on a commercial single crystal diamond substrate (grown by CVD and purchased from EDP Corporation) with ~10-nm-thick Si interlayer. The Si interlayer can lower TBC, so a different bonding method is applied to Samp2 which has a ~1.88-μm-thick GaN bonded onto a commercial single crystal diamond substrate grown by a high-pressure high-temperature (HPHT) method and purchased from Sumitomo Electric Industries, Ltd. In this sample, the Si-containing Ar ion beam is employed to introduce a

~4-nm-thick interlayer to enhance the interfacial chemical interaction between GaN and diamond. More details about the bonding process can be found in references[21,123].

To create the sample for measuring the TBC between the GaN and diamond by TDTR as shown in Figure 4.1(a), a layer of Al was deposited on the sample surface as a TDTR transducer. With this sample structure, the thermal conductivity of the single crystal diamond substrates were measured first on the area without GaN. Then TDTR measurements were performed on the area with the GaN layer to measure the GaN-diamond TBC. The measured thermal conductivity of the diamond substrates was used as a known parameter in the TDTR data fitting to extract the TBC when measuring over the GaN layer. Overall, there are three unknown parameters: Al-GaN TBC, GaN thermal conductivity, and GaN-diamond TBC. As shown in Figure 4.1(b), the TDTR sensitivity of these three unknown parameters are large which is good for accurate thermal measurements. TDTR is a pump-probe technique which can measure thermal properties of both nanostructured and bulk materials.[21,28,41,43,71,74] An example of the agreement between experimental data (Exp) and the analytical heat transfer solution (Theo) in TDTR data fitting is shown in Figure 4.1 (c).

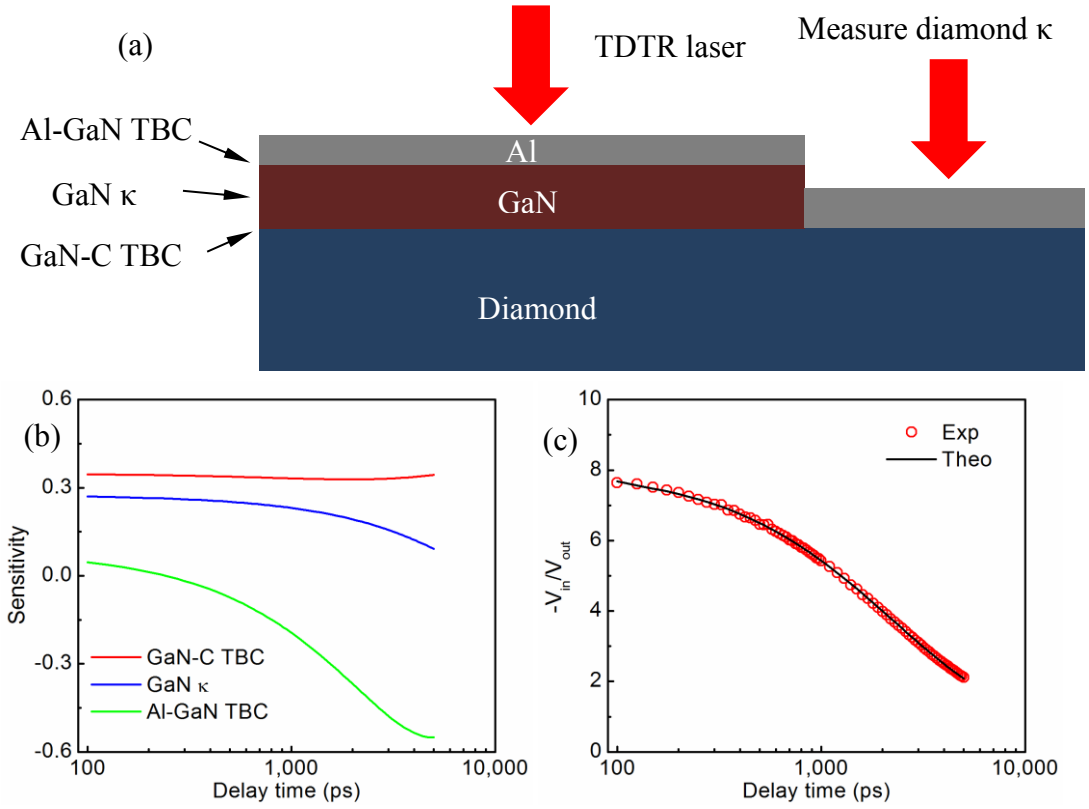

Figure 4.1. (a) TDTR measurements on the diamond and bonded GaN-diamond samples. (b) TDTR sensitivity of the three unknown parameters of Samp2. (c) TDTR data fitting of Samp2 with modulation frequency of 2.2 MHz at room temperature.

Figure 4.2(a-b) show the temperature dependence of the measured thermal conductivity of the diamond and the GaN layer and are compared with literature values. Our measured diamond and GaN thermal conductivity match with literature values.[124,126-129] The light yellow color of HPHT sample shows relatively high concentration of impurities while the CVD diamond sample used in this work is transparent. The CVD diamond sample has a higher thermal conductivity than the HPHT sample as expected and matches well with literature values of high-purity diamonds. [126,127] The measured thermal conductivity of the GaN layer (~1.88 μm) in Samp2 is close to experimentally measured bulk values and lower than density-function-theory calculated (DFT) values because of

impurities in these samples. The slightly larger thermal conductivity difference between experimental values and DFT values at high temperatures is due to higher order of phonon scatterings such as four phonon scattering.[124] Phonon-phonon scattering dominates in thermal transport at high temperatures. Because of the large phonon bandgap of GaN (the optical phonons have much larger energy than the acoustic phonons), the three-phonon scattering process among acoustic and optical phonons are limited (energy conservation during phonon scattering process). Four-phonon scattering process which is not included in the DFT calculation in the reference[128] becomes relatively important, leading to an overestimated thermal conductivity. The thermal conductivity of the GaN thin film (~700 nm) in Samp1 does not have good TDTR sensitivity so literature values are used in the TDTR data fitting.[21,130]

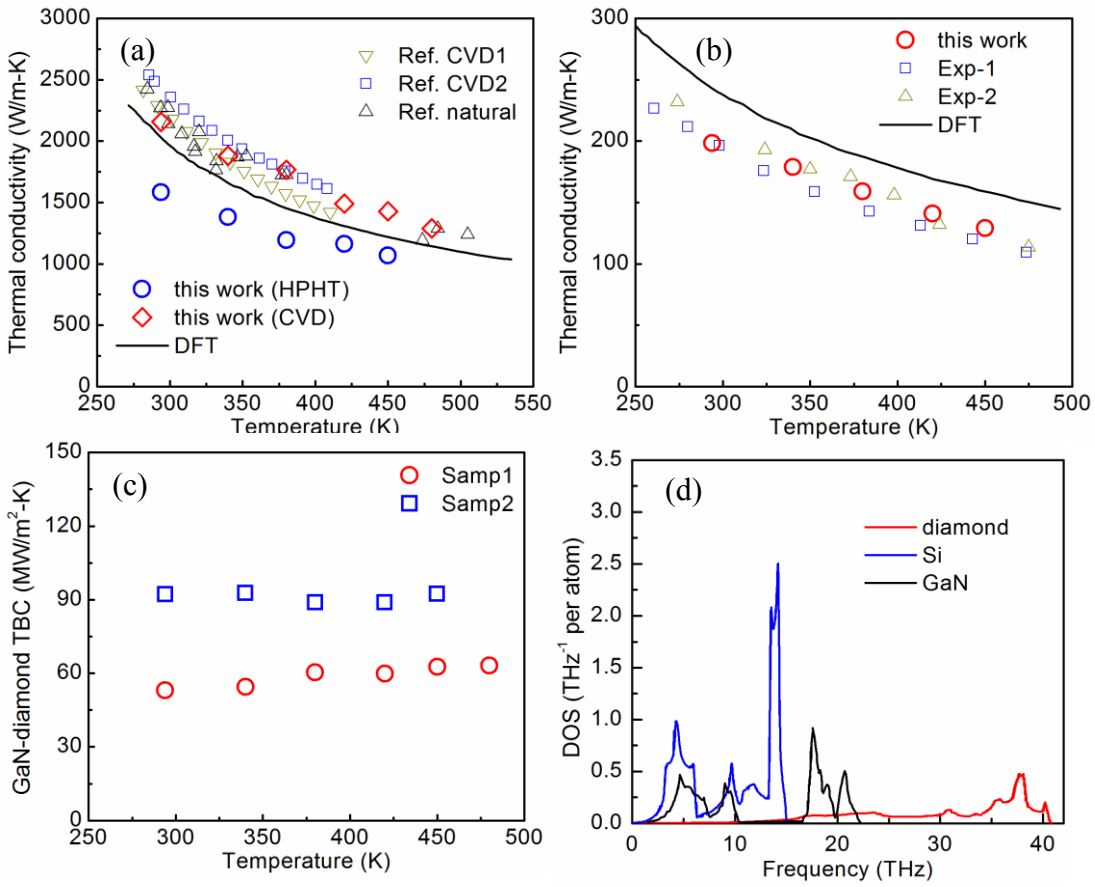

Figure 4.2. (a) temperature dependence of the measured thermal conductivity of two diamond substrates: Samp1 (CVD) and Samp2 (HPHT). The DFT values and the measured thermal conductivity of Ref. CVD1, CVD2, and natural are from literature.[126,127] (b) temperature dependence of the measured thermal conductivity of GaN layer. "DFT", "Exp-1", and "Exp-2" are DFT-calculated thermal conductivity and two experimentally measured thermal conductivity of bulk GaN from literature.[124,128,129] (c) temperature dependence of the measured TBC of bonded GaN-diamond interfaces. (d) phonon density of state of GaN, Si, and diamond.[43,131]

The temperature dependence of the measured TBC of room-temperature bonded GaN-diamond interfaces are shown in Figure 4.2(c). Samp2 has a much higher TBC (92 MW/m^2-K) than Samp1 (53 MW/m^2-K) at room temperature because of the thinner

interlayer. For the data fitting of the TDTR measurements in this work, the Si interlayer is very thin, so its thermal resistance is added to the total thermal resistance of the interface. The measured TBC is the effective TBC of the GaN-Si-diamond architecture at the interface (GaN-Si interface + Si layer + Si-diamond interface). The measured TBC of both samples show weak temperature dependence in the measured temperature range (295 K to 480 K). The Debye temperatures of GaN, Si, and diamond are higher than 480 K.[43,132] For perfect GaN-Si-diamond interfaces, effective TBC should increase with temperature in the range of 295 K to 480 K because an increasing number of phonons are involved in the thermal transport across the GaN-diamond interfaces as temperature increases. However, for the bonded GaN-Si-diamond interfaces in this work, the disorder at the interface and Ar atoms trapped at the interface increases phonon scattering, which possibly explains the weak temperature dependence of the measured TBC. More details about the interfacial structure-thermal property relationship will be discussed later. Figure 4.2(d) shows the phonon DOS of GaN, Si, and diamond.[43,131] Generally speaking, large phonon DOS overlap leads to large TBC. A thin interlayer with a max phonon frequency between two adjacent materials has been reported to cause an increase in TBC.[99,133] As shown in Figure 4.2(d), the max phonon frequency of Si is lower than those of both GaN and diamond. The Si interlayer would reduce the TBC of GaN-diamond interfaces. Therefore, the TBC of bonded GaN-diamond interfaces still have the potential to be improved by using other interfacial layers such as SiC, AlN, or SiNx, even though our measured TBC for Samp2 is already among the high TBC for GaN-diamond interfaces.[115,134]

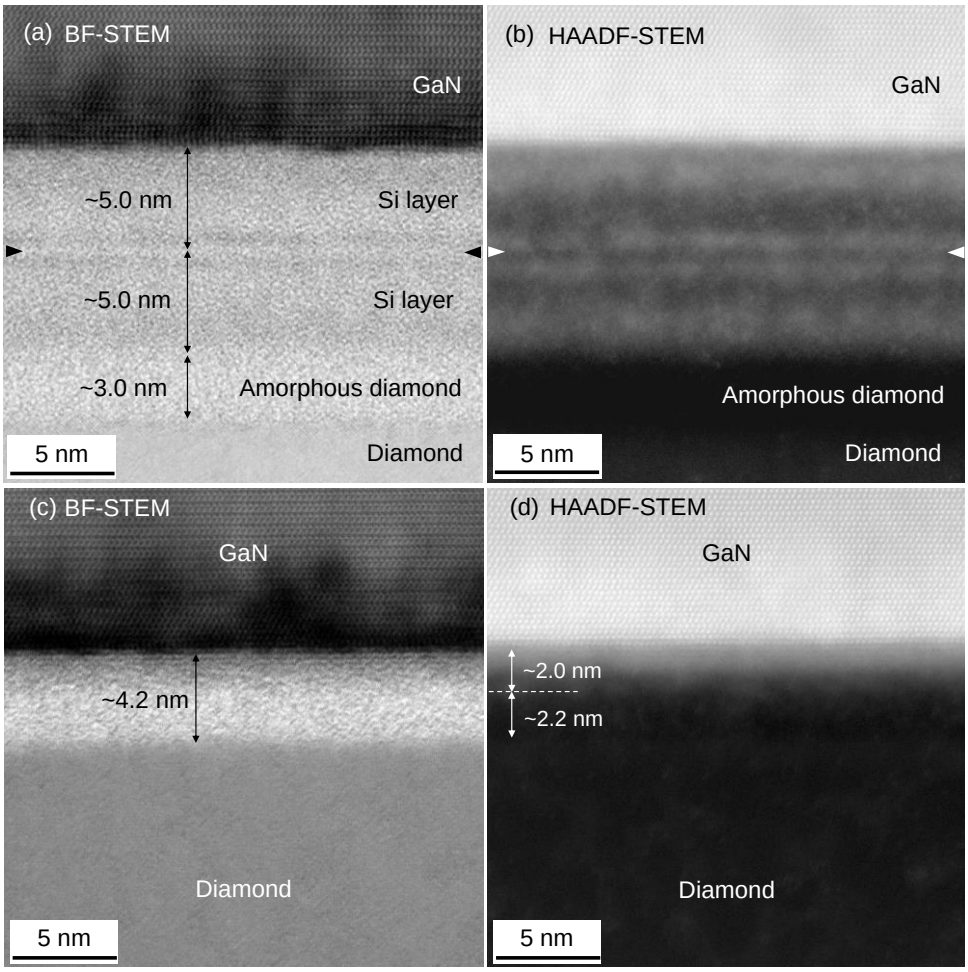

Figure 4.3. (a-b) Cross-section bright-field (BF) and high-angle annular dark-field (HAADF) HR-STEM images of GaN-diamond interfaces of Samp1. (c-d) Cross-section bright-field (BF) and high-angle annular dark-field (HAADF) HR-STEM images of GaN-diamond interfaces of Samp2.

To help elucidate the measured TBC and its relationship to the sample architecture, HR-STEM and EELS are used to study the structure of the GaN-diamond interfaces. As shown in Figure 4.3(a-b), the GaN-diamond interfaces of Samp1 are composed as two layers of amorphous deposited silicon and one amorphous diamond layer. Similar to a previous study in the literature[123], no amorphous GaN is observed. The bonding interface

is the Si-Si interface, marked by two triangles in Figure 4.3(a-b). The thicknesses of the Si interlayer and the amorphous diamond induced by the surface activation with an Ar ion beam are ~10 nm and ~3.0 nm, respectively. Figure 4.3(c-d) shows the BF and HAADF HR-STEM images of the GaN-diamond interface of Samp2. Only a ~4-nm-thick overall amorphous layer is observed. The bonded interface is not sharp and the thickness of amorphous diamond is approximately 2 nm. The 2-nm-thick amorphous layer between GaN and diamond is supposed to be amorphous silicon deposited by the Si-containing Ar ion beam during surface activation.

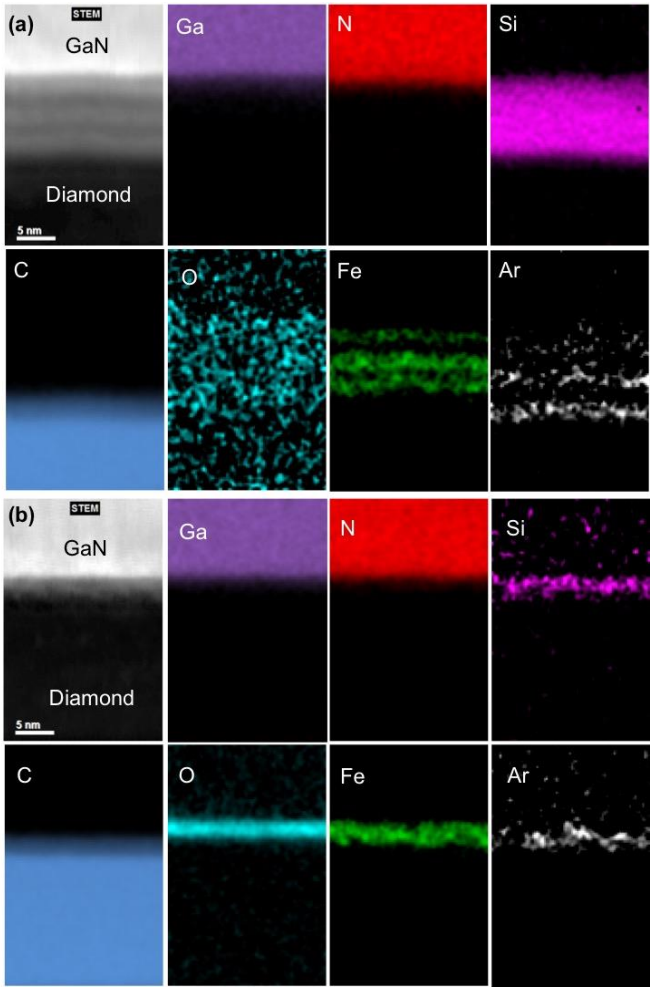

Figure 4.4. STEM images of the GaN-diamond interface of Samp1 (a) and Samp2 (b), followed by their high-resolution EELS mappings: Ga map in purple, N map in red, Si map in pink, C map in blue, O map in Cyan, Fe map in green, and Ar map in white.

Additionally, high-resolution EELS analysis is used to study the chemical composition at the interfaces. As shown in Figure 4.4(a), the EELS element mapping of the interface confirms the interlayer thicknesses in the TEM images. Si atoms are implanted into diamond and GaN, and Ar atoms are also implanted into diamond. Some ion elements also show up at the interfaces, originating from the ion beam source which is made of stainless steel. The three-layer distribution of Fe corresponds to the activated GaN surface,

the activated diamond surface, and the bonding interface. The bonding interface has the highest atomic composition of Fe (~6%). Please note these Fe contamination could be removed after further improvement of the bonding environment. The O maps in Figure 4.4(a) is oxygen-contaminated after sample preparation, which is supposed to be no oxygen at the interface. Different from the interface bonded by modified SAB with sputtering-deposited Si nanolayer, Si-containing Ar ion beam does not cause much implantation of Si at the interface. As shown in Figure 4.4(b), the EELS element mapping of the interface of Samp2 indicates that the interface layer is composed of Si, Ar, O, and Fe. No implantation of Si is observed near the interface. The disorder at the interface confirms our discussion above about the weak temperature dependence of GaN-diamond TBC. Due to the complicated nature of interfacial thermal transport, it is still unclear that how these imperfections such as Ar, O, and Fe defects, and amorphous Si, affect the TBC of the bonded interfaces. Further processing refinements are necessary to change or control the distribution of defects, impurities, and the amorphous layers to further improve TBC and elucidate their effects.

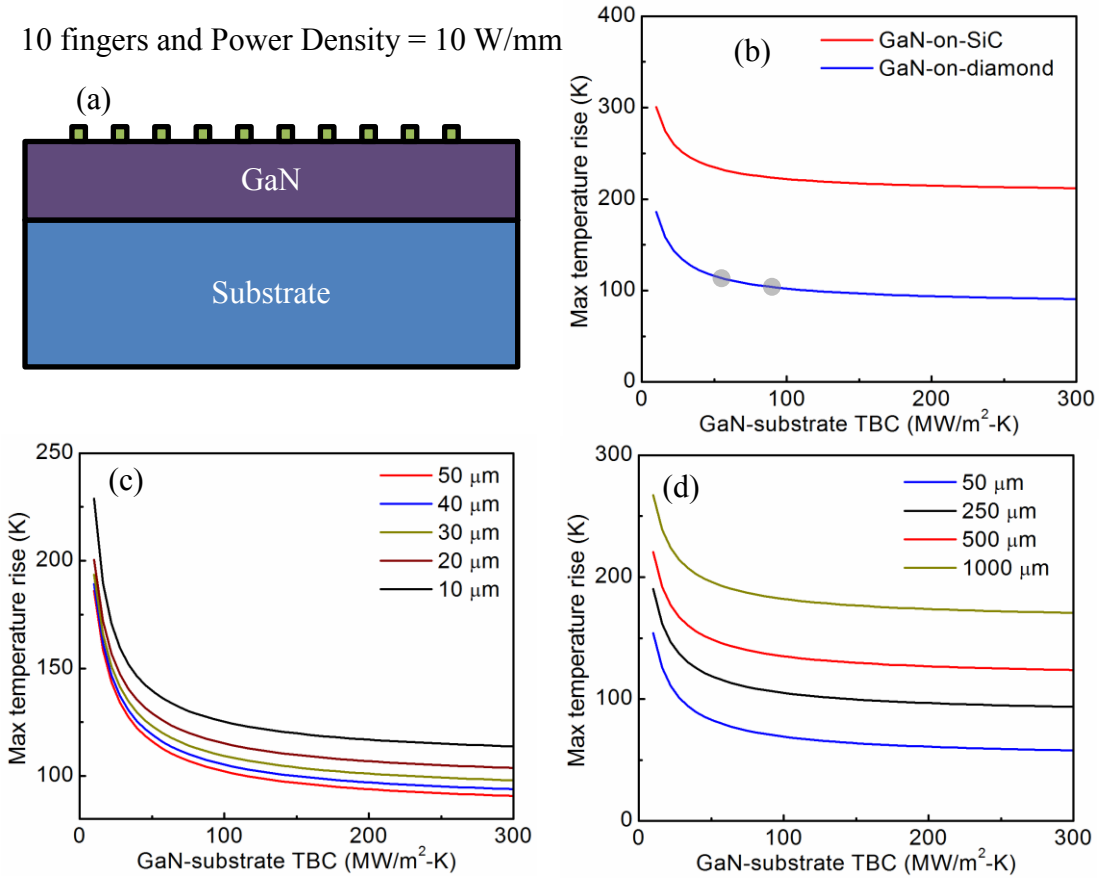

Figure 4.5. (a) A 800-nm GaN device with 10 fingers seated on a substrate is modeled with a power density of 10 W/mm.[135] (b) the max temperature of the device is calculated with different GaN-substrate TBC and substrates. (c) the effect of gate-gate spacing (10-50 μm) on the max temperature with different GaN-diamond TBC. (d) the effect of gate width (50-1000 μm) on the max temperature with different GaN-diamond TBC.

To estimate the potential effect of room-temperature bonded GaN-Diamond interfaces on the thermal response of GaN HEMTs, a 800-nm GaN device with 10 fingers seated on different substrates is modeled under fully open channel condition with a power density of 10 W/mm.[135] The thermal model of this device is based on an analytical solution of steady-state heat transfer in multilayer structure with discrete heat sources. The

boundary condition of the top of the device are constant heat flux at the heating area and insulation at the non-heating area. The bottom of the device includes a die-attach layer and convection in the sink plane. The thickness of SiC or diamond is 200 μm and that of the SnAg die attach is 50 μm with a thermal conductivity of 33 W/m-K. The convection heat transfer coefficient of the bottom boundary condition is 6.5 x 10^5 W/m^2-K at the sink and ambient temperature is 20 ^oC. In the calculation, a quarter-model was used to reduce the computational expense because of the symmetric structure of the device. The thermal conductivity of 800 nm layer GaN is 150 W/m-K.[21,130] Figure 4.5(b) shows the max temperature of the device with a heating source width of 4 μm, a heating source length of 500 μm, and gate-gate spacing of 50 μm. The thermal conductivity of SiC and diamond used in the modeling are 380 W/m-K and 2000 W/m-K, respectively.[2,124] The max temperature of GaN devices on a diamond substrate is much lower than that on a SiC substrate, indicating the advantage of using diamond substrates. Max temperature decreases sharply with increasing GaN-substrate TBC when GaN-substrate TBC is small but saturates for large GaN-substrate TBC. Figure 4.5(c) shows the effect of gate-gate spacing on the max temperature with different GaN-diamond TBC. The power density, heating source width, gate width of the device are 10 W/mm, 4 μm, and 500 μm, respectively. The gate-gate spacing ranges from 10 μm to 50 μm. The max temperature of devices increases with decreasing gate-gate spacing. When the GaN-diamond TBC is small (<50 MW/m^2-K), the max temperature increases more sharply with decreasing GaN-diamond TBC for small gate-gate spacing. Increasing GaN-diamond TBC is very important for devices with reduced gate-gate spacing. Figure 4.5(d) shows the effect of gate width on the max temperature with different GaN-diamond TBC. The power density, heating source

width, gate-gate spacing of the device are 10 W/mm, 4 μm, and 20 μm, respectively. The gate width ranges from 50 μm to 1000 μm. The max temperature increases with gate width while keeping power density constant. The GaN-substrate TBC shows similar trend with Figure 4.5(b). For all cases modelled in Figure 4.5(b-d), GaN-diamond TBC is the key to minimize the max temperature especially for small GaN-diamond TBC values. Additionally, the measured TBC of the GaN-diamond interfaces in this work are about 50 and 90 MW/m^2-K. The max temperatures of GaN-on-diamond devices with these TBC values are shown as solid gray dots in Figure 4.5(b). The max temperature does not decrease significantly with TBC if the TBC is larger than 50 MW/m^2-K. The max temperature of GaN devices bonded on diamond substrates is much lower than that on SiC substrates, showing the great potential of cooling GaN devices bonded with single crystal diamond substrates. To compare the cooling performance of GaN devices with state-of-the-art GaN-diamond/SiC/Si TBC, the max temperature of 800 nm GaN devices is modeled with heating source width of 4 μm, gate-gate spacing of 20 μm, and gate width of 500 μm. Even if the highest GaN-SiC TBC (230 MW/m^2-K) and GaN-Si TBC (143 MW/m^2-K) in the literature are used,[21,136] the power density of GaN-on-diamond can reach 20.3 W/mm, ~2.5 times as that of GaN-on-SiC (8.2 W/mm), and ~5.4 times as that of GaN-on-Si (3.78 W/mm) with a max temperature of 250 ^{o}C of the devices. It is notable that all the discussion above are steady-state heat transfer conditions. For high frequency and high power applications of GaN HEMTs, the working frequency ranges from 1 GHz to 100 GHz, which results in a thermal penetration depth less than 100 nm. The localized transient heating area will not reach the interface between GaN and high thermal conductivity substrates. Therefore, the generated heat will dissipate through the GaN-substrate interface

but the transient heat transfer will not reach the interface. TBC is expected to affect the device performance by steady-state heat transfer.

Table 4.1. Summary of GaN-diamond TBC in the literature and this work.

	Method	**Conditions**	**Interlayer**	**Method**	**TBC** (MW/m^2-K)
Ref.[11]	CVD growth of diamond on GaN		~25 nm dielectric	Raman	~37
Ref.[11]	CVD growth of diamond on GaN		~50 nm dielectric	Raman	~28
Ref.[137]	CVD growth of diamond on GaN	>600 ºC	~50 nm dielectric	Raman	56
Ref.[138]	CVD growth of diamond on GaN		~30 nm SiNx	TDTR	~35
Ref.[139]	CVD growth of diamond on GaN		28 nm SiNx	TTR	83
Ref.[120]	High temperature bonding	>700 ºC	Adhesion layer	TDTR	21-28
Ref.[140]	High temperature bonding	>700 ºC	22 nm SiNx	TDTR	~58
Ref.[115]	CVD growth of diamond on GaN		~ 5 nm SiNx	TDTR	~100
Ref.[134]	CVD growth of diamond on GaN		~ 5 nm SiNx	TTR	~150
This work	SAB bonding	Room Temp.	~ 10 nm Si	TDTR	53
This work	SAB bonding	Room Temp.	~ 2 nm Si	TDTR	92

Table 4.1 summarizes the GaN-diamond TBC measured in the literature and this work. “TTR” is transient thermoreflectance. Our measured GaN-diamond TBC for Samp2 is among the high TBC values reported ever. An advantage of the bonding technique in this work is the room-temperature processing temperature so no additional stress remains due to different coefficient of thermal expansion after bonding.[121] It is notable that the diamond used in this work is single crystal diamond with ultra-high thermal conductivity. However, for CVD growth of diamond on GaN with a dielectric layer, the nanoscrystalline diamond near the GaN-diamond interfaces has significantly reduced thermal conductivity

(tens of W/m-K).[13,15,28,43] Moreover, the thermal conductivity of nanoscrystalline CVD diamond is anisotropic and nonhomogeneous which offsets the high thermal conductivity of diamond for cooling GaN devices. The single crystal diamond substrates used in this work do not have these disadvantages and will pave the way for thermal management of GaN-on-diamond devices.

4.4 Conclusions

This work reported the heterogeneously integration of GaN with single crystalline diamond substrates with two modified room-temperature surface-activated bonding techniques for thermal management of GaN-on-diamond applications. The measured TBC of the bonded GaN-diamond interfaces is among the high values reported in the literatures and is affected by the thickness of the interlayer. Due to the disorder and defects at the interfaces, a weak temperature dependence of GaN-diamond TBC was observed. HR-STEM and EELS results show the presence of interfacial amorphous layers and their compositions at the bonded interfaces. The thermal conductivity of two single crystal diamond substrates and the GaN film were also measured and matches reasonably with literature values. Device modeling shows a relatively large GaN-diamond TBC value (>50 MW/m^2-K) achieved by surface activated bonding for GaN-on-diamond devices could enable to take full advantage of the high thermal conductivity of single crystalline diamond. This work paves the way for room-temperature heterogeneous integration of GaN with diamond and will impact applications such as electronics cooling especially for GaN-on-diamond devices.

CHAPTER 5. TUNABLE THERMAL ENERGY TRANSPORT ACROSS DIAMOND MEMBRANES AND DIAMOND-SI INTERFACES BY NANOSCALE GRAPHOEPITAXY

5.1 Introduction

The ongoing miniaturization of microelectronic devices, as well as their heterogeneous integration to create advanced functionalities, have led to high local power densities and circumstances where thermal effects limit the overall device performance.[141-143] Keeping these devices cool has become a design challenge aiming to avoid the degradation of device performance and reliability.[142,143] Due to the architecture of these electronic systems, heat dissipation can be significantly influenced or even dominated by the thermal boundary resistance found at heterointerfaces.[75,85] Previous efforts to reduce thermal boundary resistance between solids include bridging phonon spectra mismatch and enhancing interfacial bonding.[69,90,94,95,99,134,144] In addition, several theoretical studies show that incorporating nanostructures at the interface enlarges the interface contact area and increases TBC, but experimental results are inconsistent.[36,145-148] Tuning thermal transport across interfaces or even in the adjacent materials remains largely an open issue.

Graphoepitaxy is a technique that uses artificial surface relief structures to induce crystallographic orientation in thin films grown on a surface.[149-152] This technique was invented to grow Si, Ge, and KCl on amorphous SiO_2 substrates about four decades ago.[149-152] After that, it was extensively used to grow block copolymers and carbon nanotubes to control orientation or alignment.[153-155] By introducing nanoscale graphoepitaxy into

thermal transport across interfaces, the solid-solid interface contact area increases due to the artificial surface structures, which may contribute to increasing TBC. The crystallographic orientation of grains in the adjacent membranes may affect their thermal conductivity as well. These two synergistic effects provide a possible solution to tune thermal transport across interfaces and in the adjacent membranes.

In this work, diamond membranes are grown on silicon substrates by nanoscale graphoepitaxy. TDTR is used to measure the thermal conductivity of the diamond layer and the diamond-silicon TBC. The diamond thermal conductivity and diamond-silicon TBC are tuned with different surface pattern sizes. STEM and X-ray diffraction (XRD) are used to study the grain size distribution and orientation. NEMD simulation and a Landauer approach are used to understand the diamond-silicon TBC. Our work is notably the first effort to tune diamond growth on silicon substrates, and subsequently thermal transport across diamond-silicon interfaces and diamond membranes by graphoepitaxy. It is expected that graphoepitaxy can be applied to polycrystalline diamond grown on other substrates as well.

5.2 Samples and Methodologies

5.2.1 Samples

In this work, six silicon wafers are prepared (Samples A1, B1, ref1, and A2, B2, ref2). Samples A1, A2, B1, and B2 are patterned silicon wafers with nanoscale trenches while Samples ref1 and ref2 are flat silicon wafers without nanoscale trenches. The dimensions of the interface patterns are summarized in Table 5.1. Nanocrystalline diamond (NCD) films were fabricated with the same growth conditions on both nanopatterned and

flat silicon substrates acquired from LightSmyth Technologies. NCD was grown on a flat (100) oriented polished silicon substrate by a microwave plasma-assisted chemical vapor deposition (MPCVD) method in IPLAS 5.0 KW CVD reactor with hydrogen and methane as reactant gases. The growth conditions were consistent throughout the entire deposition process as follows: 750 °C substrate temperature, 7.0 Torr chamber pressure, 1400 W microwave power, and 0.5% methane to hydrogen ratio. The flat Si substrate enables in-situ NCD film thickness measurement using laser reflectometry, and also serve as a reference for the future comparison with the patterned silicon. Prior to diamond growth, all the silicon substrates were seeded by ultrasonic treatment in ethanol-based nanodiamond suspension prepared from detonation nanodiamond powder (International Technology Center, North Carolina, USA (ITC)). According to the manufacturer specifications the material grade used here has a high degree of grain size homogeneity with an average particle size of 4 nm, and a chemical purity in excess of 98%. The SEM analysis of the backside of a typical NCD film deposited with implementation of the abovementioned seeding method shows a uniform seed density greater than 10^{12} nuclei/cm^2. With this type of diamond nucleation, the NCD films were formed through grain coalescence and subsequent growth competition of initially random-oriented nanodiamond seeds. Only the crystals with the fastest growth speed along the thickness direction extend to the surface. This process ultimately leads to a formation of a well-pronounced columnar grain structure in the film as well as an increase in lateral grain size with film thickness. The use of carbon-lean growth conditions as above is intended to suppress secondary renucleation and increases film quality by reducing grain boundaries.

Table 5.1. Dimensions of Si patterns for Samples A, B, and ref.

Sample	Height	Top width	Bottom width
	nm	nm	nm
A	47	60	77
B	105	205	215
ref	0	0	0

Samples A1, B1 and ref1 were used for material characterization with 1-um-thick diamond films. Samples A2, B2 and ref2 were used for TDTR measurements with 2-um-thick diamond films to improve TDTR sensitivity. To study the effect of nanoscale graphoepitaxy on both diamond thermal conductivity and diamond-silicon TBC on the samples, the 2-um-thick samples are chosen for thermal measurements, where TDTR is sensitive to both diamond thermal conductivity and diamond-silicon TBC.. All the diamond layers were grown under the same conditions.

5.2.2 Thermal Characterization

The thermal properties in this work are measured by multi-frequency TDTR.[44,46,140,156] As shown in Figure 5.1, a pump beam which is chopped by a modulator heats a sample periodically and a delayed probe beam measures the temperature decay of the sample surface through a change in thermoreflectance. The probe beam delay time is controlled by a mechanical stage, which is used to create a temperature decay curve from 0.1 to 5 ns. By fitting the experimental signal picked up by a lock-in amplifier with an analytical solution of heat flow in the layered structure, one or more thermal properties of the sample can be extracted.[28,41,44,46,140,156] In TDTR measurements, the distance that the

heat penetrates into the surface depends on the modulation frequency and the thermal diffusivity of the sample. By tuning the modulation frequency, the thermal properties of the sample with different penetration depths are inferred, leading to different sensitivity to different unknown parameters.

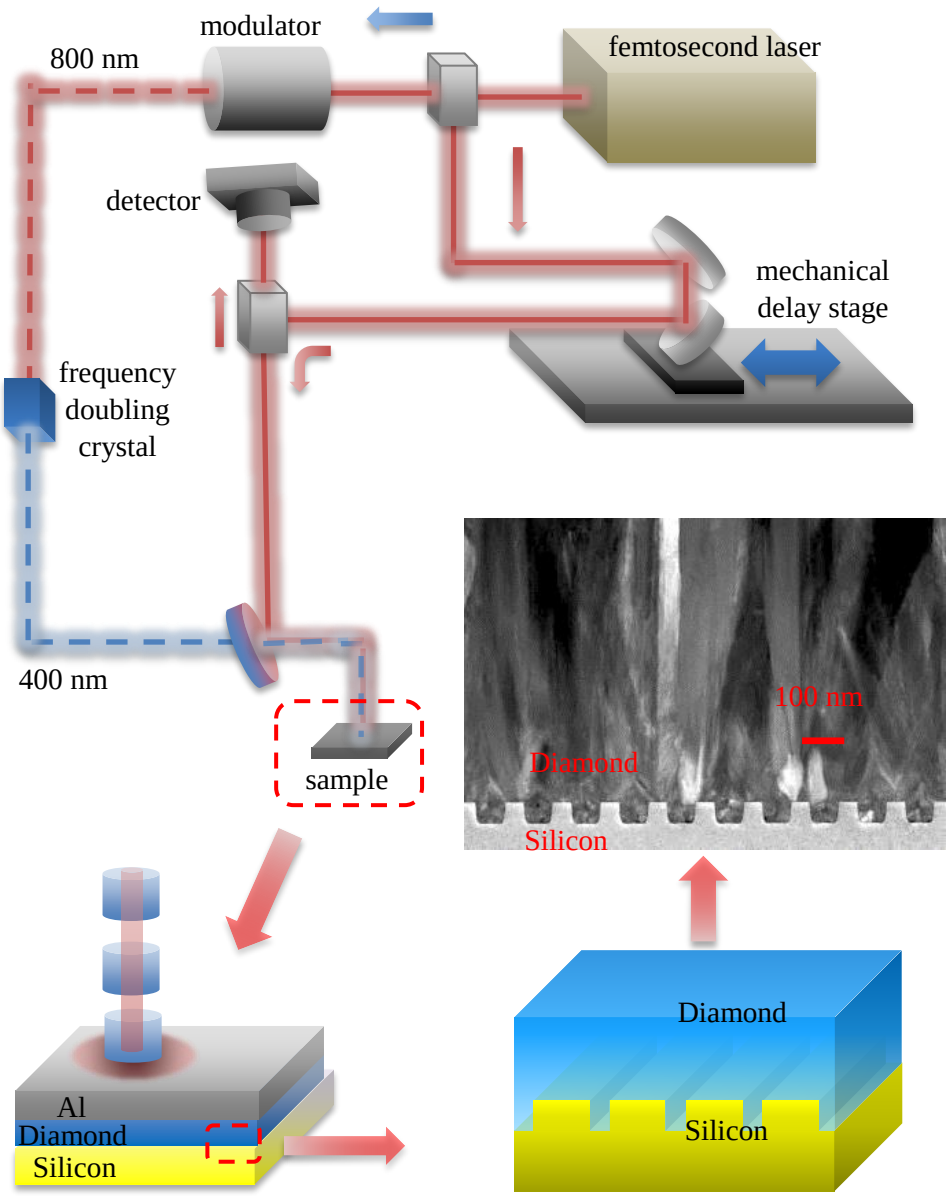

Figure 5.1. Schematic diagram of TDTR and sample structure grown by graphoepitaxy with nanoscale patterns. The TEM image shows the patterned diamond-silicon interface (CVD diamond grown on patterned silicon substrates by graphoepitaxy).

To perform TDTR measurements, a layer of Al is deposited on the sample surface as a transducer. The Al thicknesses are determined by the picosecond acoustic method[125,157]. In this case, the thickness of the Al transducer layers are determined to be

103 nm, 80 nm, and 74 nm for samples A2, B2, and ref2, respectively. The thermal conductivity of the Al layer is determined by measuring its electrical conductivity and applying the Wiedemann-Franz law. The thermal conductivity of the silicon substrate is taken from the literature (142 W/m-K).[158] The thickness of the diamond layers in Samples A2, B2, and ref2 are measured to be 2.3 μm by a SEM. The density and specific heat of CVD diamond and Al used for the analysis of the data are from the literature. The pump and probe beam size (radius) are 8.1 μm and 6.4 μm for Samples A2, B2. Those of Sample ref2 are 7.7 μm and 7.5 μm, measured with a DataRay scanning slit beam profiler. A standard silicon calibration sample is checked every time before measuring the diamond samples. Three-frequency TDTR measurements are used to measure the Al-diamond TBC, diamond cross-plane thermal conductivity, and diamond-silicon TBC.

5.2.3 Materials Characterization

Plan-view and cross-section TEM samples were prepared using Focused Ion Beam (Nova 600 SEM/FIB). The near-interface plan-view samples were made at the Si patterned region so that both silicon and diamond can be seen. STEM images were then generated using a Titan STEM (FEI) system under 200 kV. The STEM mode with a high-angle annular dark-field (HAADF) detector provides images with contrast due to differences in the adjacent grain orientation. The cross-section STEM images were used to study the grain growth near the nucleation region. The plan-view images were used to measure average grain size and its distribution within an area. Dark-field images were also taken to show grains with either (111) or (110) plane parallel to the sample surface. These images were used to calculate the grain growth ratio for (111) and (110) oriented grains (more details can be found later). In order to analysis the chemical information at the interface, electron

energy loss spectroscopy (EELS) was then taken at the diamond-Si interface using JEOL JEM-2100F. X-ray diffraction (XRD) was used to analyze cross-plane preferred grain orientation. The XRD 2θ:ω scan was performed on a Jordan Valley D1 diffractometer with Cu $K\alpha_1$ radiation and a parallel beam source. In these measurements, ω was offset by a few degrees from the surface orientation of the Si substrate to avoid the strong (004) Si reflection. This offset was the same for all samples so it would not affect the measurement of the preferred orientation.

5.2.4 NEMD Simulations

The MD simulations were performed using the LAMMPS[159] code and Tersoff potentials.[160] The simulation domain contains a 23-nm-long diamond (28,080 atoms) and a 33-nm-long Si (11,712 atoms) with the same cross-section area of 3.28*2.16 nm^2. The temperature difference is applied along the x direction, and periodic boundary conditions are applied along y and z directions. In the NEMD simulations, the domains were first stabilized at 300 K by NPT simulations (constant pressure and temperature) with 2,000,000 steps and then converted to NVE (constant volume and energy) ensemble, with the temperatures of 350 K and 250 K applied at the ends of diamond and Si, respectively. 3,000,000 steps of NVE simulations were used to stabilize the temperature gradient and heat current through the whole system. The time for each step is 0.5 fs. After that, another 2,000,000 NVE steps simulations were performed to extract the stabilized temperature gradient and heat flux. The amorphous layer was constructed before the NEMD simulations by melting the 2-nm-long region of diamond at the interface at 3000 K with fixed volume (20% larger than crystalline diamond to allow atoms to move), followed by an annealing process to 300 K at a rate of 0.54 K/ps (10,000,000 steps) as well as a NPT relaxation.

5.2.5 Landauer Approach

The Landauer approach is a widely used method to predict TBC (G)[50,51,85,161-163] and it has been applied here to calculate the TBC at the diamond-silicon interface. The general form of the Landauer formula calculating G at a 3D/3D interface is:

$$G = \frac{q}{A\Delta T} = \frac{1}{A\Delta T}\Big(\sum_p \frac{A}{2} \iint D_1(\omega) f_{BE}(T_1) \hbar\omega v_1(\omega) \tau_{12}(\theta,\omega) \cos\theta \sin\theta \, d\theta d\omega - \sum_p \frac{A}{2} \iint D_2(\omega) f_{BE}(T_2) \hbar\omega v_2(\omega) \tau_{21}(\theta,\omega) \cos\theta \sin\theta \, d\theta d\omega \Big), \quad (5.1)$$

where q is the net heat flow rate, A is the cross-sectional area of the interface, D is the phonon density of states (DOS), f_{BE} is the Bose-Einstein distribution function, $\hbar$ is the reduced Planck constant, ω is the phonon angular frequency, v is the phonon group velocity, τ_{12} is the transmission coefficient from material 1 to 2 (here it is from silicon to diamond), θ is the angle of incidence, and the sum is over all phonon modes. With the restriction of detailed balance, the formula can be simplified as:

$$G = \frac{q}{A\Delta T} = \frac{\sum_p \frac{1}{2} \iint D_1(\omega)\big(f_{BE}(T_1) - f_{BE}(T_2)\big)\hbar\omega v_1(\omega)\tau_{12}(\theta,\omega)\cos\theta \sin\theta d\theta d\omega}{\Delta T}. \quad (5.2)$$

Without considering the local non-equilibrium near the interface, the formula can be further simplified as:

$$G = \sum_p \frac{1}{2} \iint D_1(\omega) \frac{df_{BE}}{dT} \hbar\omega v_1(\omega) \tau_{12}(\theta,\omega) \cos\theta \sin\theta \, d\theta d\omega. \quad (5.3)$$

Here, the DMM is used to calculate the transmission coefficient.[50,162,163]

$$\tau_{12}(\omega) = \frac{\sum_p M_2(\omega)}{\sum_p M_1(\omega) + \sum_p M_2(\omega)}, \quad (5.4)$$

where M is the number of modes, which is proportional to the square of the wave vector for a 3D isotropic material. The DMM assumes all the incident phonons are diffusely scattered at the interface and lose their memory.

5.3 Results and Discussion

5.3.1 Enhanced Thermal Transport across Interfaces

To dissipate the localized Joule heating in power electronics, CVD diamond is an excellent candidate for thermal management because of its high thermal conductivity.[8,9,12,14,15,164] However, when integrating diamond with other materials, the TBC is very small due to the large mismatch in phonon DOS between diamond and other materials. Generally speaking, phonons with a certain frequency have a high likelihood to transmit through an interface only when phonons with this frequency exist on the other side of the interface or when specific modes that are local to the interface help the transmission of those phonons.[71,72,165-168] Therefore, the degree of DOS overlap between two adjacent materials has a significant effect on the TBC across an interface. Due to the small mass of carbon atoms and strong bonds among these carbon atoms in diamond, diamond has a very high cutoff frequency (the Debye temperature of diamond is 2230 K).[169] When integrating diamond with other materials, poor DOS overlap and a correspondingly small TBC are expected. Figure 5.2(a) shows a comparison of the DOS of diamond and several typical materials (Pt, MgO, SiC, and Si). The DOS overlaps between diamond and these materials are small, leading to small TBC.[79,170]

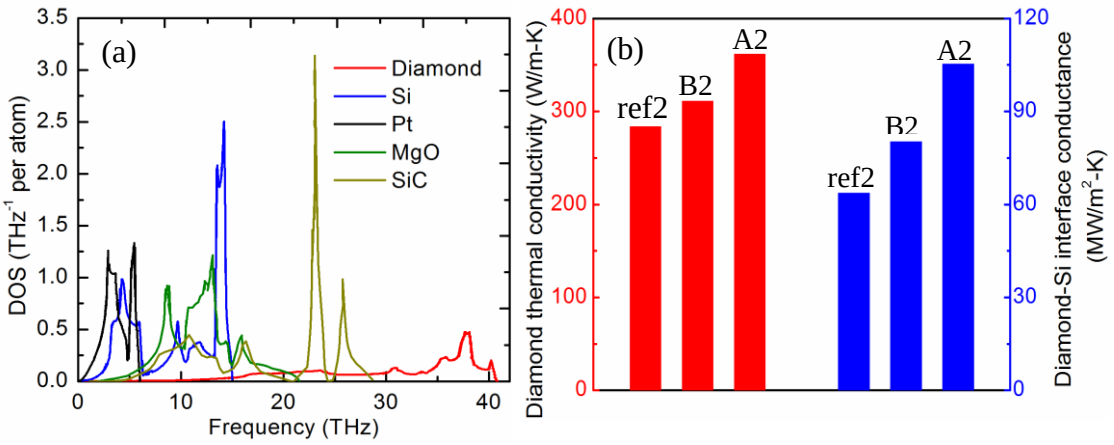

Figure 5.2. (a) Phonon DOS of diamond and a few other materials, highlighting the sizable differences in the vibrational spectra of different crystalline materials.[79,170,171] (b) Comparison of the cross-plane thermal conductivity of diamond layers and diamond-silicon TBC for the flat sample (ref2) and the patterned samples (A2 and B2).

By using multi-frequency TDTR measurements,[41,44,46,140,156] the diamond cross-plane thermal conductivity and the diamond-silicon TBC at room temperature were measured and the results are shown in Figure 5.2(b). Here, the TBC of flat diamond-silicon interfaces will be discussed first. The TBC of the flat interface in this work is measured to be 63.7 MW/m^2-K, which is very close to the value measured by Joule-heating method in the work done by Goodson *et al*. (about 66.7 MW/m^2-K)[37,172], larger than the value measured by 3-Omega method by Mohr *et al*. (50 MW/m^2-K)[173]. These measured TBC of flat diamond-silicon interfaces from literature and this work are close to 60 MW/m^2-K and generally agree with each other.

In terms of theoretical calculations and simulations for diamond-silicon TBC, Khosravian *et al*. calculated the diamond-silicon TBC using NEMD. The TBC is determined as 335.6 MW/m^2-K, which is 5 times larger than our measured value.[174] NEMD

was used to calculate the diamond-silicon TBC as well. The TBC is found to be 381 MW/m^2-K. The difference between these NEMD results derives from the difference of the used atomic potentials and size effects of finite simulation domains. The calculated TBC from the Landauer formula with transmission from DMM is 316.9 MW/m^{2}K. These theoretical values calculated by NEMD and the Landauer approach with DMM are close to 350 MW/m^2-K and generally agree with each other while they are much larger than the experimental values. Our future work will discuss more about the fundamental understanding of diamond-silicon TBC, especially for the large difference between experimental and theoretical results.

Now we turn to our measured TBC of the nanopatterned interfaces. The measured diamond-silicon TBC for the sample grown by graphoepitaxy (sample A2) is 105 MW/m^2-K, which is the highest diamond-silicon TBC measured to date. This high measured TBC is attributed to enlarged contact area between diamond and silicon. When comparing with the flat diamond-silicon interface, the diamond-silicon TBC of A2 increases by 65% for the nanopatterned interface. The patterned interface enlarges the diamond-silicon contact area, which behaves like fins in convective heat transfer. Because the fin length is very short, the relation between the ratio of the TBC and the ratio of contact area should be as below:

$$\frac{G_p}{G_{ref}} \approx \frac{S_p}{S_{ref}} \tag{5.5}$$

Here, G_p and G_{ref}, S_p and S_{ref} are the TBC and contact areas of the patterned and reference samples. $S_p = L_t + L_b + 2h$ and $S_{ref} = L_t + L_b$. Here, L_t, L_b, h are the top width, bottom width, and height of the pattern. The contact area of the patterned interface

(Samples A1 and A2) increases by 69% ($S_p/S_{ref} - 1$) compared with that of the flat diamond-silicon interface (Samples ref1 and ref2). This consistency between TBC enhancement (65%) and contact area enlargement (69%) confirms that the increased TBC is due to the larger contact area. Here we experimentally confirm the effect of increased contact area on TBC predicted by the theoretical calculations and simulation works in the literature.[145-147] For Sample B2, the TBC is also enhanced by 26%, but it is smaller than the contact area enhancement (50%). This difference may be due to the grain impingement which will be discussed later, which facilitates good contact between the diamond and the side walls of the silicon patterns. For CVD diamond near the nucleation interface, the grain size is very small. The size of the diamond seeds is only about 4 nm. Diffusive thermal transport at the diamond side is expected even if the amorphous layer is not considered. So contact area enlargement should increases TBC. For the silicon side, the nanoscale patterns decrease the silicon thermal conductivity near the interface due to size effect but the dominant thermal resistance is still the diamond-silicon TBR. It is acknowledged that ballistic thermal transport near the interface plays some role but the dominant reason for the increased TBC is due to contact area enhancement. This is consistent with previous experimental and theoretical works.[36,145-147]

To explore the mechanism behind the enhanced thermal conductance across the interface, STEM and XRD are used to characterize the structure of the diamond-silicon interfaces. The STEM images in Figure 5.3(a-b) were taken using the HAADF detector to show the contrast from different grains. They show that the grains nucleating from the silicon surface tend to impinge upon one another, coalescing together in the area located above the trenches. Figure 5.3(a) shows a plan-view STEM image that includes the

diamond-silicon interface and Figure 5.3(b) shows a cross-section STEM image of the diamond-silicon interface. It can be clearly seen that the patterned silicon ridges in Figure 5.3(a). The diamond grains grow on the Si trench and eventually impinge at the middle of the trench region, as indicated by the yellow dashed lines in Figure 5.3(a-b). This grain impingement affects the preferred crystal orientation and corresponding thermal properties. First, the grain impingement forces the grown diamond to have very good contact with the silicon nanoscale trenches. No voids are observed near the interface. This good contact facilitates thermal transport across the interface and enhances the TBC. This may be the reason that the TBC enhancement of Sample A2 matches well with contact area enhancement. Second, the grain impingement induces preferred grain orientation (texturing) in the continually grown diamond layer.

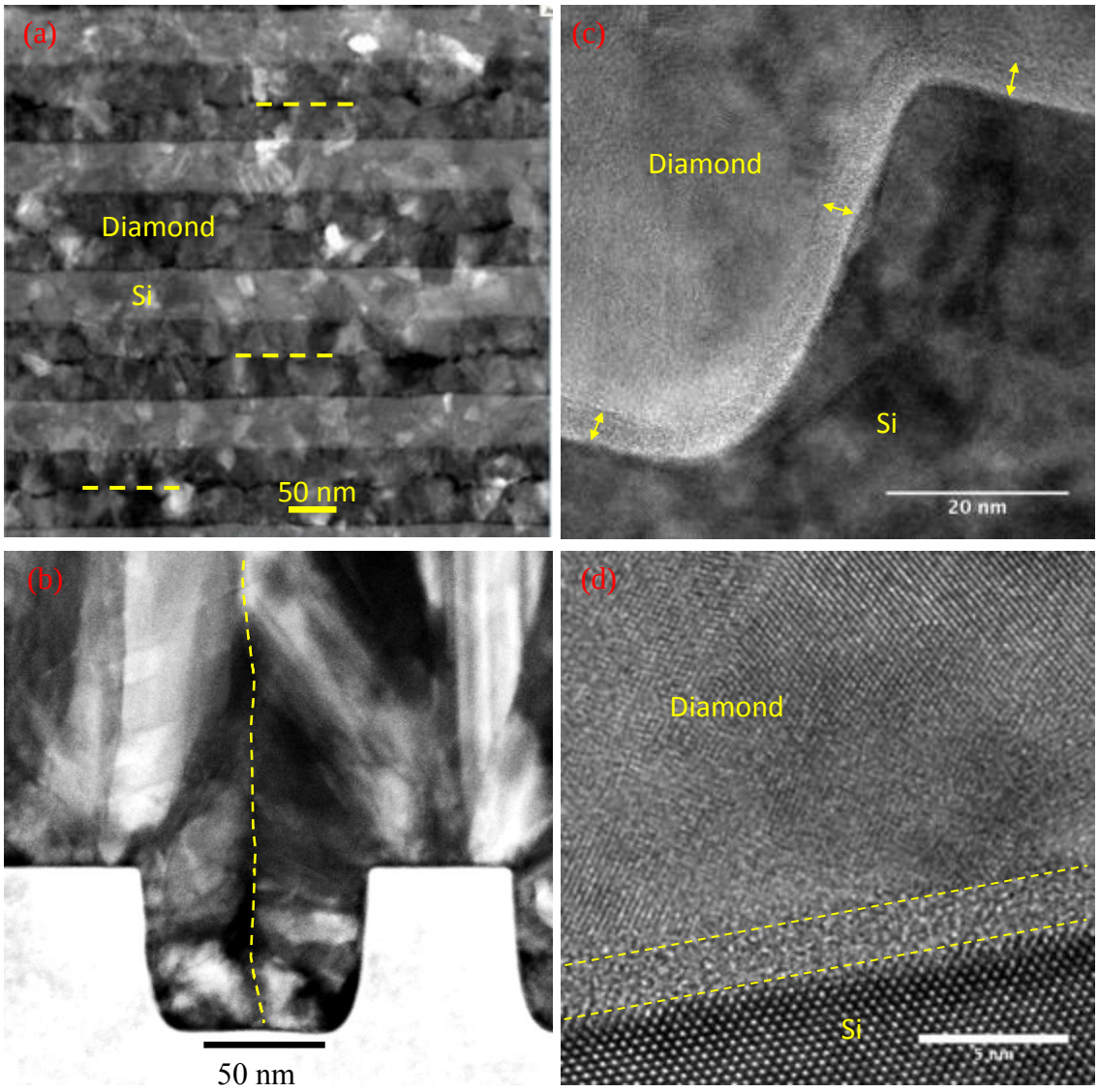

Figure 5.3. Grains impinge over the patterned trenches (Sample A1) and amorphous layer at the diamond-silicon interface. (a) Plan-view STEM image near the diamond-silicon interface. (b) Cross-section STEM image of diamond-silicon interface. (c-d) Cross-section HRTEM images to show the amorphous carbon region at the diamond-silicon interfaces of the patterned and flat samples.

Figure 5.3(c-d) includes HR-TEM images taken at the diamond-silicon interfaces showing lattice fringes for the silicon substrate and diamond grains. As shown in Figure

5.3(c-d), no SiC is observed at or near the interfaces for either the patterned or the flat Si-diamond interfaces. However, an amorphous layer is present (about 2 nm thick) for both interfaces. EELS is performed on the flat interface and the results are shown in Figure 5.4. The measurements were performed in four regions including the pure diamond region, the diamond-silicon interface region and the silicon substrate region. The EELS results show the existence of ≤ 4 nm (measurement resolution) sp^2 C at the interface. The EELS measurement combined with the HRTEM image supports the conclusion that a 2-nm amorphous layer observed in the HRTEM is sp^2 C, which is formed during the diamond deposition process for both patterned and flat samples.

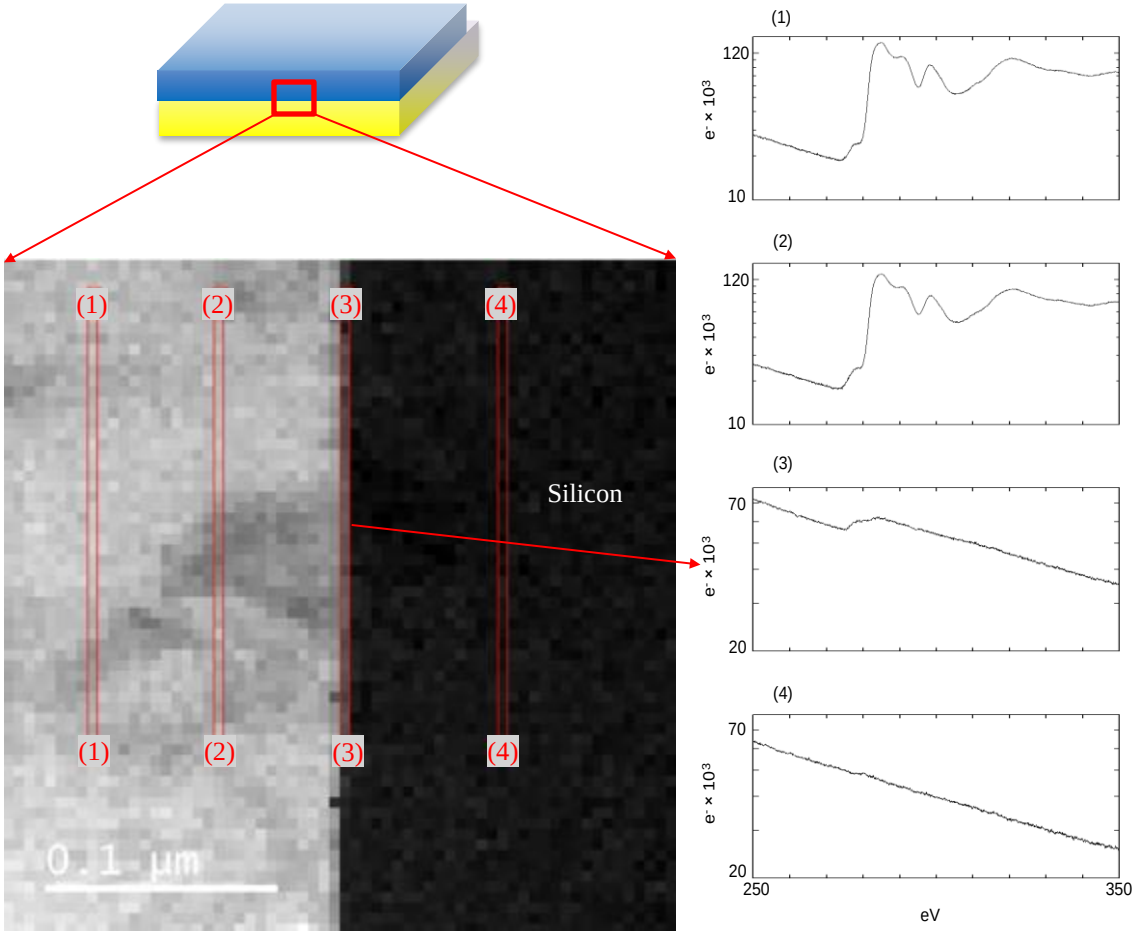

Figure 5.4. EELS data of diamond-silicon interface. The measurements were performed in four regions including the pure diamond region (1-2), the diamond-Si interface region (3), and the Si substrate region (4). The results show the existence of < 4 nm (length of 1 pixel) sp^2 C at the interface.

To study the effect of amorphous carbon at the diamond-silicon interface on thermal transport, NEMD simulations are performed. As shown in Figure 5.5, a temperature difference is applied across the diamond-silicon interface. It is found that the interface between amorphous diamond and silicon presents larger thermal conductance than that between crystalline diamond and silicon, i.e., the temperature jump at the interface (x=2.2 nm) becomes smaller after the amorphous diamond layer is introduced. This is

consistent with Si-Ge interfaces in the literature.[175] However, for our work, the amorphous carbon layer itself has thermal resistance that has an effect to lower the effective TBC value. Therefore, the overall interfacial thermal conductance does not change much. The overall TBC is determined as 381 MW/m^2-K without amorphous carbon and 378 MW/m^2-K with amorphous carbon for the systems, close to the previous TBC value calculated by NEMD.[174] The effect of the amorphous layer on the diamond-silicon TBC is negligible (smaller than 1%), so the intrinsic diamond-silicon thermal boundary resistance is the dominant thermal resistance at the interfaces. Moreover, this amorphous carbon layer exists for both the flat and patterned samples. Therefore, the existence of the amorphous layer does not affect our conclusion that the enhanced thermal transport across the diamond-silicon interface grown by graphoepitaxy is due to the enlarged contact area.

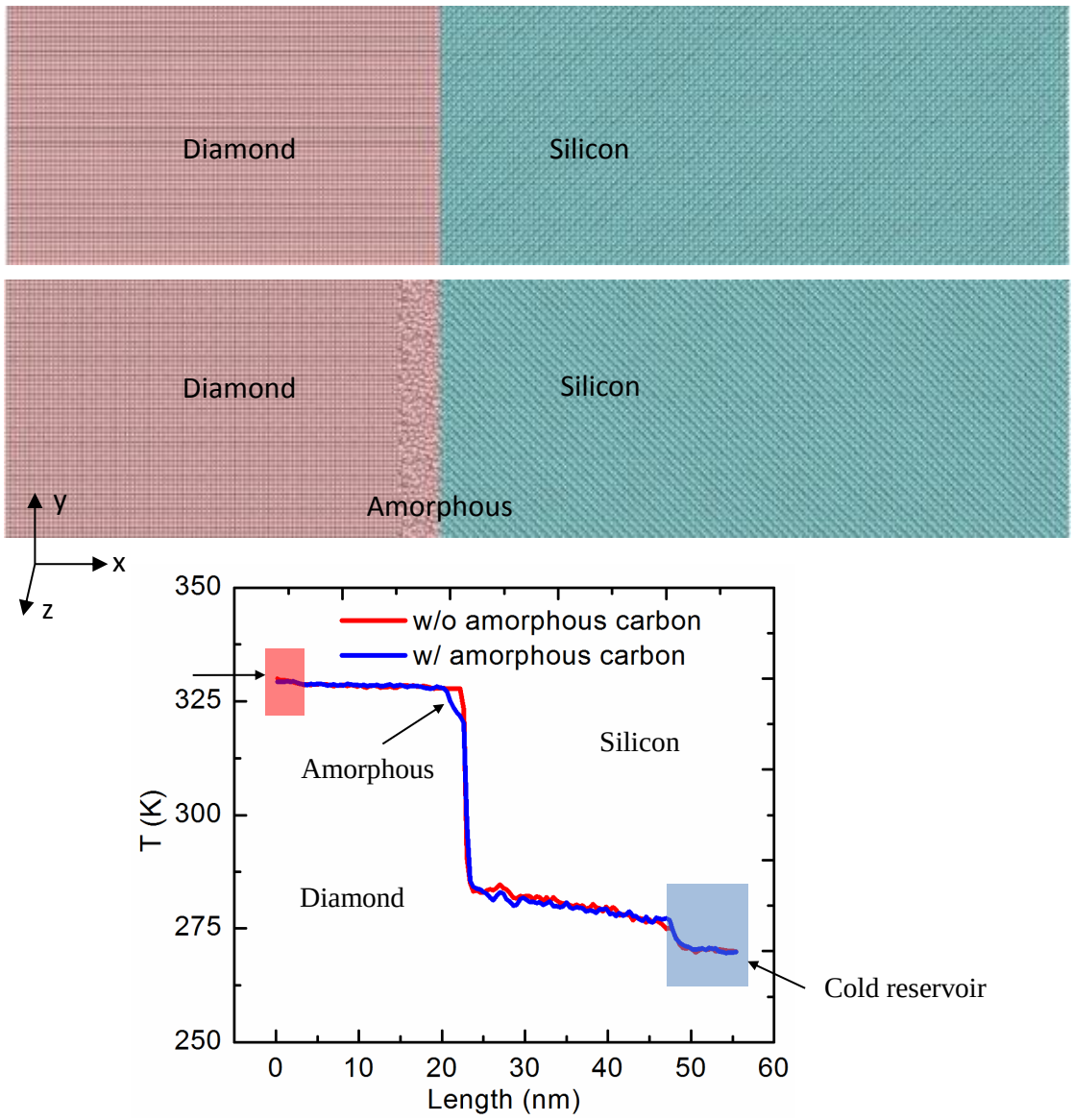

Figure 5.5. NEMD simulation of thermal transport across the diamond-silicon interfaces with and without amorphous carbon layer. The effect of the amorphous layer on diamond-silicon TBC is negligible (<1%).

To understand more about the phonon mode transport across the interface, a Landauer approach is used to study the diamond-silicon TBC as well. The Landauer approach is a method in frequency space, which facilitates understanding modal phonon

transport across the interface compared with NEMD. NEMD simulations include inelastic scatterings naturally from the anharmonic interatomic potentials and could model complicated interface structures, such as an amorphous layer at the interface, while the Landauer approach only considers elastic scatterings and predicts the TBC between bulk materials with perfect interfaces. The two methods provide different insights in the thermal transport across diamond-silicon interfaces so both methods were included here.

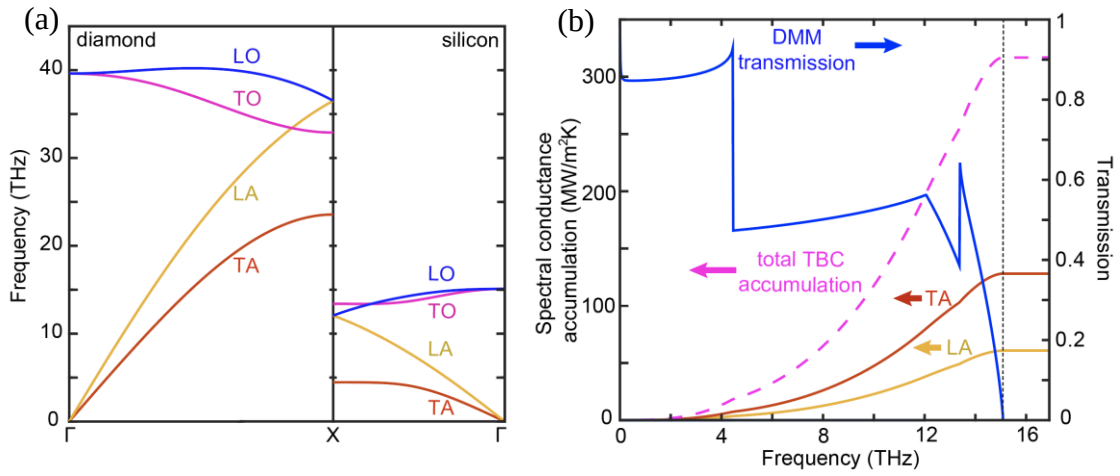

Figure 5.6. (a) The phonon dispersion relations of silicon and diamond from first-principles calculations. (b) The spectral conductance accumulation and the transmission coefficients from DMM at the interface between diamond and silicon. The left vertical axis is the spectral conductance accumulation while the right vertical axis is the transmission coefficient. The black dotted line is the cutoff frequency of silicon.

The phonon properties of silicon and diamond are calculated from first-principles calculations. The phonon dispersion relation curves, shown in Figure 5.6(a), are used as inputs to calculate transmission coefficients. Along the Γ–to-X direction in the reciprocal lattice, there are 6 phonon branches: 2 transverse acoustic (TA) branches, 1 longitudinal

acoustic (LA) branch, 2 transverse optical (TO) branches, and 1 longitudinal optical (LO) branch. The phonon group velocity (the slope of the dispersion curve) of diamond is much larger than that of silicon, especially for the acoustic branches. The calculated transmission coefficients from DMM are shown in Figure 5.6(b). In the low frequency range (below 4.5 THz), the number of modes in silicon is much larger than that of diamond. DMM assumes that phonons lose their memory of original directions after reaching the interface. The probability of phonons propagating to the side with larger number of modes is much higher than that to the other side. As a result, the transmission coefficient at low frequency from diamond to silicon is quite high (~0.9). 4.5 THz is the cutoff frequency of the silicon TA branch. Above this frequency, the number of modes on the silicon side decreases sharply so the transmission coefficient drops above this frequency. Here, each turning point in the transmission curve indicates the starting or cutoff frequency of a phonon branch.

The spectral conductance accumulation curve is shown in Figure 5.6(b). For phonons with frequencies lower than 4 THz, the contribution to TBC is very small because of the small phonon DOS and small phonon energy even though the transmission coefficient is very high. For phonons with higher frequencies, the high spectral contribution to TBC results from the large phonon DOS. The contribution from TA and LA branches to TBC are calculated as well. The contribution from TA branches is twice as that from LA because TA has two branches so the DOS is almost twice as that of LA. The TBC from Landauer is smaller than that from NEMD. This difference is mainly attributed to anharmonic contribution to TBC, which is especially true for diamond-silicon interfaces because the energy diamond phonons could have is much higher than those of silicon phonons. It is possible that multiple silicon phonons scatter at the interface and become

one diamond phonon, which contributes to transport energy across the interface (inelastic scatterings).

According to the MD simulation, the amorphous layer has negligible effect on the diamond-silicon TBC. This amorphous layer makes phonon scatterings near the interface more diffusive (closer to the assumption of DMM). However, some recent modeling results show that there exists a localized interface mode at the interface which affects thermal transport across the interface significantly.[168,176,177] The assumption of Landauer formula with a transmission coefficient deriving from DMM may not hold with the existence of interface mode. The diamond-silicon interface with and without an amorphous layer possibly have different interface modes, which will be discussed more in the future work. As an estimate of upper limit of diamond-silicon TBC, the radiation limit is calculated as 569 MW/m^2-K.

5.3.2 Enhanced Thermal Conduction in Diamond Membranes

As shown in Figure 5.2(b), very surprisingly, we find the diamond cross-plane thermal conductivity of the patterned samples grown by graphoepitaxy (Samples A2 and B2) increases by 28% and 10% comparing with that of the flat sample (Sample ref2). To figure out the structure-property relation, we used TEM to study the grain sizes of the diamond layer. In polycrystalline dielectric materials, phonons dominate thermal conduction. Phonons scatter with defects, grain boundaries and phonons, which determine phonon mean free path and correspondingly thermal conductivity. Large grains (less boundaries) scatter phonons less extensively, leading to a long phonon mean free path and correspondingly high thermal conductivity.[25,28,178] In order to measure the grain growth

ratio for grains with different orientations, dark field (DF) images were generated over several μm length of the TEM samples. An aperture was used to select the reciprocal lattice points in selected area diffraction patterns that correspond to grains with (111) or (110) planes parallel to the sample surface. The resulting images show the selected grains in bright contrast. As an example, a diamond grain with (110) orientation is shown in the insert of Figure 5.7(a). The grain width (indicate with red arrows) was measured every 100 nm (as shown with blue arrows) from the depth at which the grain is first observed. We define the "grain growth ratio" as the ratio of the grain size measured at different distances over the grain size measured at 100 nm in order to quantify if grains with certain orientations grow at the expense of others. Figure 5.7 (a) and (c) show how the grain growth ratios of several diamond crystals with (111) orientation and (110) orientation parallel to the surface change with different distance from the nucleation interface. As depicted in Figure 5.7, for diamond layers grown on both patterned and flat silicon substrates (Samples A1 and ref1), grains with (111) orientation typically shrink or are blocked by other grains, while grains with (110) orientation tend to expand horizontally while growing. As a result, grains with (110) orientation are longer (wider) in the film-thickness (cross-plane) direction than grains with (111) orientation. Similarly, it has been reported that the (110) grain orientation is a preferred grain orientation for CVD diamond growth under certain conditions.[179-181] As discussed above, these long (wide) grains scatter phonons less extensively in the cross-plane direction, resulting in longer phonon mean free path and correspondingly higher thermal conductivity.

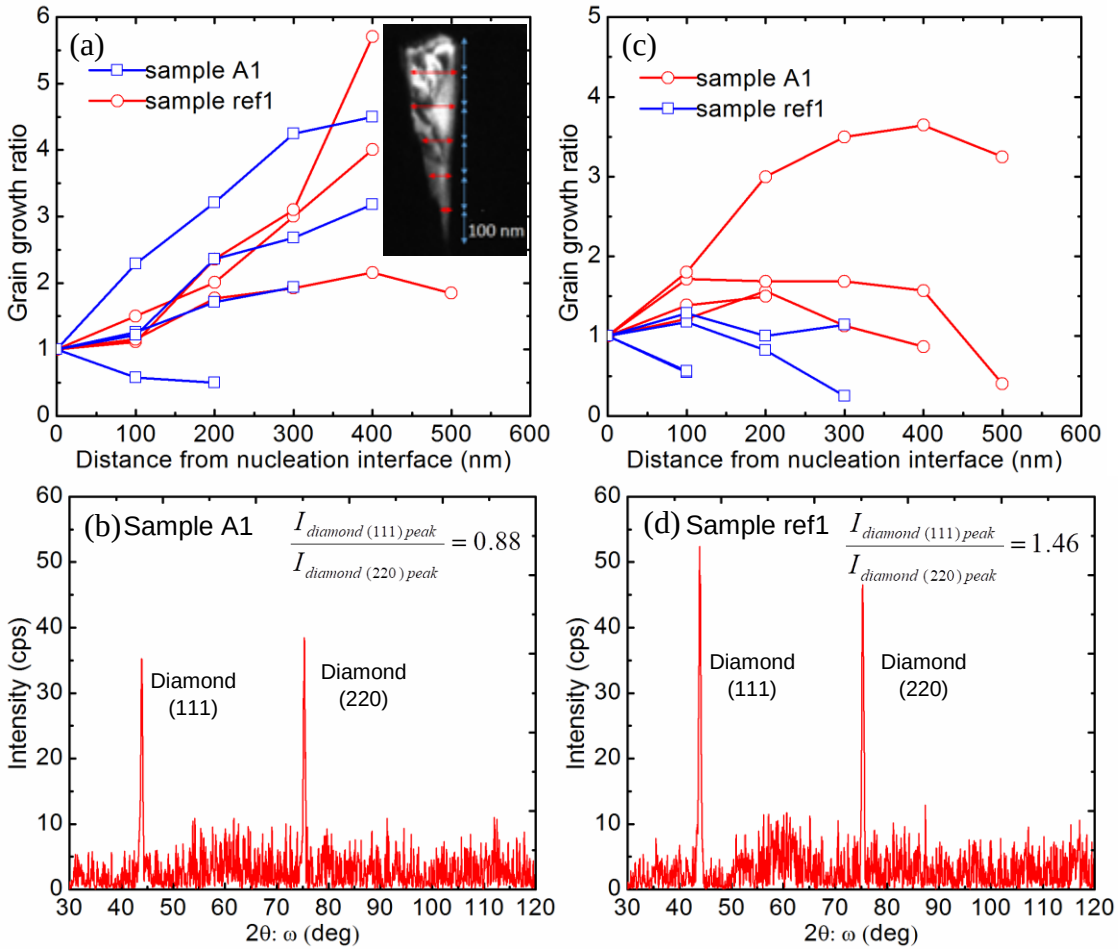

Figure 5.7. (a) The grain growth ratios of diamond crystals with (110) orientation. The inset (Dark field TEM image to select grains with (110) plane parallel to surface) shows how the grain grown ratio was measured. (b) XRD scan for sample A1. (c) The grain growth ratios of diamond crystals with (111) orientation. (d) XRD scan for sample ref1.

To assess the cross-plane preferred grain orientation, Samples A1, B1, and ref1 were measured using XRD 2θ:ω scans. The XRD peak intensities are from the grains that have that specific plane parallel to the surface and the integrated intensity ratio provides information about preferred orientation. The XRD patterns of Samples A1 and ref1 are shown in Figure 5.7 (b) and (d) as comparison. The integrated intensity ratio $I_{diamond\,(111)}$

$_{peak}/I_{diamond\ (220)\ peak}$ of Samples A1, B1, and ref1 are 0.88, 1.13, and 1.46, respectively. Samples A1 and B1 have smaller integrated intensity ratio than Sample ref1 (all of them are smaller than a ratio of 2.50, which would be the ratio for random grain orientations). This feature indicates that all three samples have (110) preferred orientation while the patterned sample (A1, B1) shows stronger (110) preferred orientation than the flat sample. As discussed above, crystals with (111) orientation typically shrink or are blocked while crystals with (110) orientation are not. When comparing with grains with (111) orientation, the long (wide) crystals with (110) orientation facilitate thermal conduction along the cross-plane direction because of reduced phonon-grain boundary scattering.[178] The higher fraction of grains with (110) orientation in the diamond layer grown by graphoepitaxy leads to long phonon mean free path. This result explains the high cross-plane thermal conductivity measured in patterned samples.

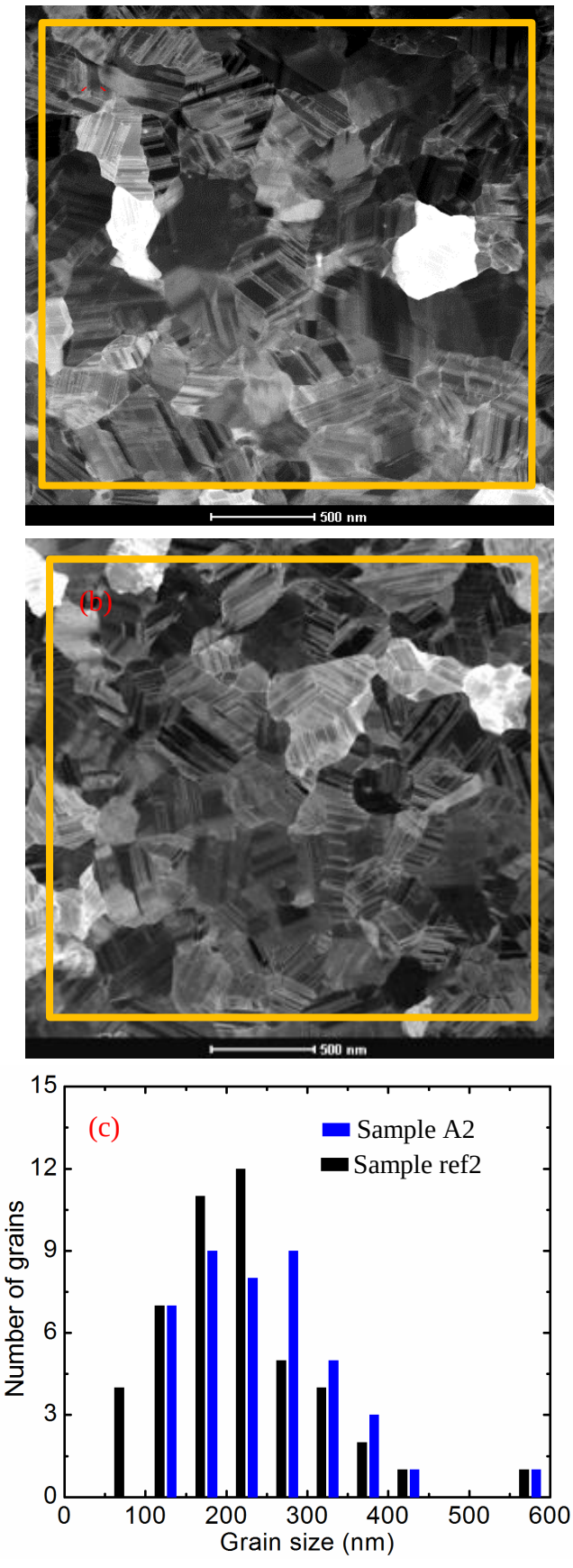
500 nm
(b)
500 nm
(c)
Sample A2
Sample ref2
Number of grains
Grain size (nm)
0
3
6
9
12
15
0
100
200
300
400
500
600

Figure 5.8. The plan-view STEM image near the diamond film surface for 2 um samples: (a) the patterned sample (Sample A2) and (b) the flat sample (Sample ref2). (c) Grain distribution of Samples A2 and ref2. The average grain size of Sample A2 is 247 nm while that of Sample ref2 is 216 nm.

To further confirm our conclusions about the grain size impact, we also measured the grain distributions of Samples A2 and ref2 with plan-view TEM samples as many more grains could be measured than with cross section TEM. Figure 5.8(a-b) show the STEM images of Samples A2 and ref2 near the surfaces of the diamond layers. The grain size is measured within the yellow box in the images and the distribution information is summarized in Figure 5.8(c). The average grain size of the patterned sample is 247 nm which is larger than that of the flat sample (216 nm). Moreover, the patterned sample does not have very small grains (0-100 nm) and has a distribution that is weighted toward larger grain sizes (the patterned sample has 19 grains larger than 250 nm in this area while the flat sample has only 13 within the 5.8 μm^2 area). Grain boundaries scatter phonons and limit phonon mean free paths, leading to a reduced thermal conductivity.[25,178,182] The larger average grain size and lower concentration of very small grains (less grain boundaries) scatter phonons less extensively, leading to long phonon mean free path and high thermal conductivity, which helps explain the observation that the cross-plane thermal conductivity of the diamond grown by graphoepitaxy is higher than that grown on the flat sample.

5.4 Conclusions

The thermal boundary resistance can be an important factor that limits the heat flow out of high-power-density electronics and microelectronics that require the heterogeneous

integration of materials. This is especially true for chemically deposited diamond integrated with other semiconductors due to the large phonon DOS mismatch between diamond and other materials. However, we show for the first time that it is possible to increase the TBC at semiconductor-dielectric interfaces by graphoepitaxy. By growing diamond on nanopatterned silicon wafers, the present work provides a general strategy to significantly reduce the thermal resistance of both the diamond layer and diamond-substrate interface simultaneously. The diamond-silicon TBC increases by 65% comparing with that of a flat diamond-silicon interface, which is consistent with the contact area enlargement (69%). Our results experimentally confirm the effect of contact area enlargement on TBC predicted by previous theoretical works and achieve the highest diamond-silicon TBC measured to date. The NEMD simulation results show that the amorphous carbon layer at the interface has negligible effect on thermal transport across the interface and the large intrinsic diamond-silicon thermal boundary resistance is the dominant thermal resistance. A Landauer approach is used to calculate diamond-silicon TBC and understand phonon transmissions across the interface. Furthermore, comparing with that of the diamond layer grown on the flat silicon substrate, we observe a 28% increase in thermal conductivity of the diamond layer grown on the patterned substrate which is due to preferred grain orientation (texturing) measured by STEM and XRD. In diamond layers grown on both patterned and flat silicon substrates, grains with (110) orientation typically trend to expand while growing while grains with (111) orientation shrink or are blocked by other grains. XRD results show the diamond layer grown on the patterned substrate has stronger (110) texturing than that on the flat substrate. This finding is confirmed by grain distribution analysis on diamond grain sizes near the grown side for

Samples A2 and ref2. The average grain size of the patterned sample A2 (247 nm) is slightly larger than that of the flat sample ref2 (216 nm). Moreover, the patterned sample does not have very small grains (0-100 nm) and has a distribution that is weighted toward larger grain sizes. Graphoepitaxy provides a general solution to significantly enhance thermal transport across diamond layers and diamond-substrate interfaces when integrating diamond to substrates for applications of electronics cooling.

CHAPTER 6. SIGNIFICANTLY REDUCED THERMAL CONDUCTIVITY IN *B*-$(AL_{0.1}GA_{0.9})_2O_3/GA_2O_3$ SUPERLATTICE

6.1 Introduction

As an emerging ultra-wide bandgap semiconductor material, β-Ga_2O_3 has shown promising properties for electronic device applications, such as an ultra-wide bandgap (4.8 eV) and high critical electric field (8 MV/cm), which predicts a Baliga figure of merit that is 3214 times that of Si.[38] However, the thermal conductivity of bulk β-Ga_2O_3 (10-30 W/m-K, depending on crystal orientation) is at least one order of magnitude lower than those of other wide bandgap semiconductors such as GaN (230 W/m-K), 4H-SiC (490 W/m-K), and diamond (>2000 W/m-K).[2,183] Thermal dissipation will be the bottleneck for real-world applications, especially for high power and high frequency devices. Currently, compared to demonstrations of Ga_2O_3 devices, a disproportionately smaller number of thermal studies have been performed.[39] Similar to GaN/AlGaN interfaces, to demonstrate modulation-doped field effect transistors (MODFETs), *β*-$(Al_xGa_{1-x})_2O_3/Ga_2O_3$ heterogeneous structures have been used to form a high mobility two-dimensional electron gas (2DEG) where joule heating is localized.[184-188] The thermal properties of the *β*-$(Al_xGa_{1-x})_2O_3/Ga_2O_3$ structure are the key for heat dissipation in these devices, however they have not been studied before.

In this work, the first measurement on temperature-dependent thermal conductivity of *β*-$(Al_{0.1}Ga_{0.9})_2O_3/Ga_2O_3$ superlattices epitaxial-grown on bulk (010) Ga_2O_3 substrates by MBE is measured from 80 K to 480 K. Multi-frequency TDTR is used to measure the

thermal properties of both the β-$(Al_{0.1}Ga_{0.9})_2O_3/Ga_2O_3$ superlattices and the bulk Ga_2O_3 substrates simultaneously. The phonon scattering mechanism in these structures is discussed in detail. Additionally, we estimate the TBC of β-$(Al_{0.1}Ga_{0.9})_2O_3/Ga_2O_3$ interfaces and compare it with maximum Ga_2O_3 TBC. The mechanism of phonons transmission through interfaces is discussed.

6.2 Samples and Structure

The β-$(Al_xGa_{1-x})_2O_3/Ga_2O_3$ superlattice used in this study was homoepitaxy-grown on a Sn-doped (010) Ga_2O_3 substrate, with an n-type doping concentration of $4x10^{18}$ cm^{-3}, using a Veeco Gen930 MBE system. The aluminum and gallium were provided by standard effusion cells. The oxygen plasma was produced using a Veeco RF plasma source. During the growth, the gallium and aluminum beam equivalent pressures (BEP) measured by an ion gauge were 1×10^{-8} Torr and 1×10^{-9} Torr, respectively. This led to an aluminum flux that is 9.1% of the total metal flux. The oxygen was flown into the chamber at 0.7 sccm and the RF plasma was struck using a load power of 289 W, which corresponded to a total chamber pressure of 2.18×10^{-5} Torr. The substrate temperature, measured by a thermocouple, was 500 ^oC for the entire growth. The substrate was mounted to a silicon carrier wafer using indium bonding. The substrate was grown by edge-defined film-fed growth (EFG) purchased from Novel Crystal Technology. The film has ten alternating periods of a Ga_2O_3 layer followed by a $(Al_{0.1}Ga_{0.9})_2O_3$ layer each grown for 30 minutes.

Cross-sectional TEM specimen was prepared using an FEI Strata 400 FIB with a final milling step of 5keV to reduce surface damage. Atomic resolution high angle annular dark field (HAADF) images were acquired on an aberration corrected 300keV Themis

Titan. The superlattice film thickness was determined by a scanning transmission electron microscopy (STEM) to be 114 nm, as shown in Figure 6.1. For each period, the Ga_2O_3 layer is 6.5 nm (±0.2 nm) thick while the $(Al_{0.1}Ga_{0.9})_2O_3$ layer is 4.5 nm (±0.1 nm) thick. The interfaces in the superlattice structure are not very sharp. A layer of Al (~80 nm) was deposited on the surface as the TDTR transducer as demonstrated in several previous studies.[28,41,42,74,189] Here, we measure one spot on the sample with two modulation frequencies, i.e., 3.6 MHz and 8.8 MHz, at room temperature. TDTR signal is sensitive to the thermal conductivity of the bulk Ga_2O_3 substrate with modulation frequency of 3.6 MHz while it is sensitive to the thermal conductivity of the superlattice with modulation frequency of 8.8 MHz. More details about multi-frequency TDTR measurements can be found in references.[28,44,156,190] In the TDTR data fitting, volumetric heat capacity (the product of specific heat Cp and density) is input as a fixed value. If we take the superlattice as about 5% Al_2O_3 and about 95% Ga_2O_3, the concentration of Al is quite small. Furthermore, the volumetric heat capacity of Al_2O_3 is almost the same as that of Ga_2O_3. The mixture of these two components should have similar volumetric heat capacity. So we used the volumetric heat capacity of Ga_2O_3 as that of the superlattice in the data fitting. What's more, the TDTR sensitivity of superlattice heat capacity is very small, about one ninth of that of the superlattice thermal conductivity. Even if there are some deviations by assuming the superlattice heat capacity as the heat capacity of Ga_2O_3, the effect on thermal conductivity measurements is negligible.

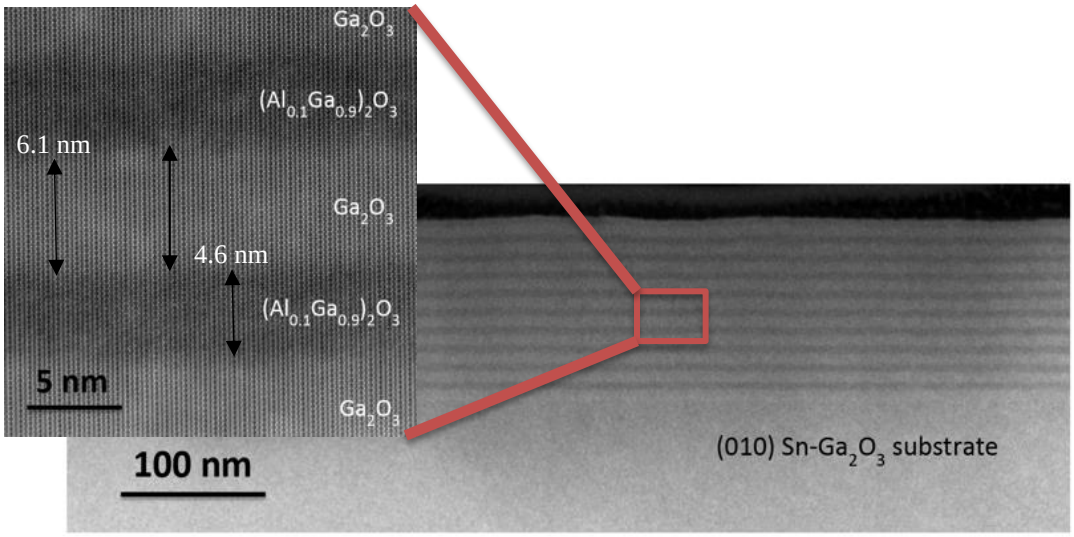

Figure 6.1. HAADF-STEM images of the β -$(Al_{0.1}Ga_{0.9})_2O_3/Ga_2O_3$ superlattice structure.

6.3 Results and Discussion

The temperature-dependent thermal conductivity of the bulk (010) Ga_2O_3 substrate and the β-$(Al_{0.1}Ga_{0.9})_2O_3/Ga_2O_3$ superlattice are shown in Figure 6.2(a). At room temperature, the thermal conductivity of the superlattice is 5.7 times smaller than that of the bulk (010) Ga_2O_3 substrate. This significantly reduced thermal conductivity further impedes thermal dissipation, potentially creating additional challenges for gallium oxide electronics devices. Aggressive thermal management techniques need to be applied for reliable device performance, such as integrating high thermal conductivity materials close to the regions where heat is being generated to aid in conducting and spreading the heat away from the source location. For the bulk (010) Ga_2O_3 substrate, its thermal conductivity decreases with increasing temperature from 80 K to 450 K because of increased phonon-phonon scattering. As temperature increases, the number of excited phonons increases, resulting in increasingly extensive phonon-phonon scattering. For the superlattice, its

thermal conductivity shows a peak at 380 K. Below 380 K, the thermal conductivity decreases with decreasing temperature while it decreases with increasing temperature above 380 K. For temperatures below 380 K, phonon-structural imperfection scattering, such as alloy and boundary, dominates in impeding thermal transport. The thermal conductivity of superlattices can be reduced to be lower than their amorphous counterparts due to the large number of thermal boundary resistances, especially when the boundaries are composed of two dissimilar materials which have very low TBC.[191] For temperatures above 380 K, phonon-phonon scattering dominates. More about the scattering mechanisms will be discussed later.

The measured thermal conductivity of the bulk (010) Ga_2O_3 substrate is compared with literature values as shown in Figure 6.2(b). Our measured values are consistent with most of other experimentally measured values and first-principle calculated values in the literature. This indicates that the Sn doping and unintentional doping do not affect the thermal conductivity significantly. The other samples measured in the literature have different levels of doping as well. It is still an open question as to how high doping concentrations impact the thermal conductivity in β-Ga_2O_3.

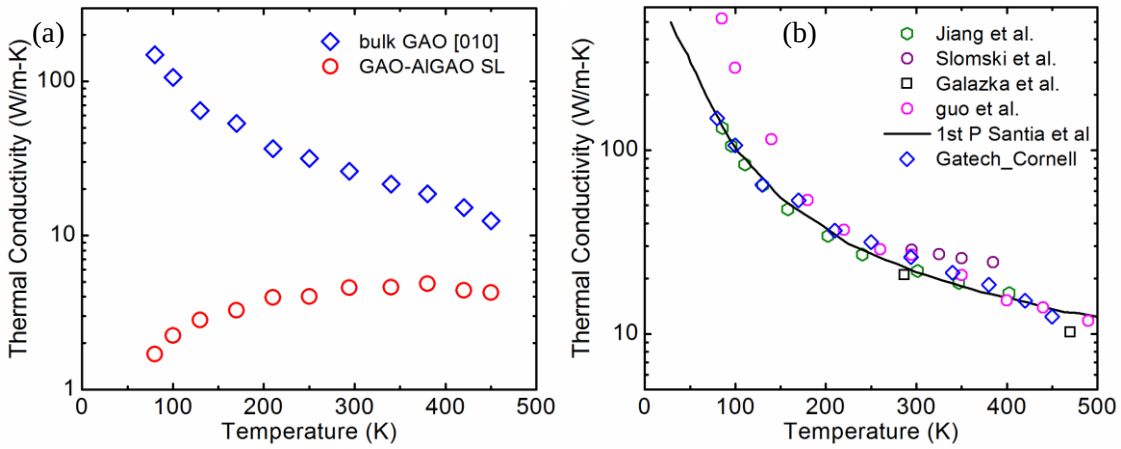

Figure 6.2. (a) Temperature-dependent thermal conductivity of the bulk Ga_2O_3 substrate and β-$(Al_{0.1}Ga_{0.9})_2O_3/Ga_2O_3$ superlattices. (b) Summary of temperature-dependent thermal conductivity of bulk (010) β-Ga_2O_3 in this work and literature.[183,192,193]

To better understand the phonon scattering mechanism in the superlattice and bulk Ga_2O_3, we calculate the inverse thermal diffusivity of both the superlattice and bulk Ga_2O_3, as shown in Figure 6.3(a). The formula of inverse thermal diffusivity is shown as below:

$$\frac{C_v}{k}(T) = \left\{\sum_{n=1}^{n} \int_0^{\omega_D} g(\omega) k_B \left(\frac{\hbar\omega}{k_B T}\right)^2 e^{\frac{\hbar\omega}{k_B T}} / (e^{\frac{\hbar\omega}{k_B T}} - 1)^2 \, d\omega\right\} /$$

$$\left\{\sum_{n=1}^{n} \int_0^{\omega_D} g(\omega) k_B \left(\frac{\hbar\omega}{k_B T}\right)^2 e^{\frac{\hbar\omega}{k_B T}} / (e^{\frac{\hbar\omega}{k_B T}} - 1)^2 \, v_\omega^2 \left(\frac{1}{\tau_{ph}} + \frac{1}{\tau_{struc}}\right)^{-1} d\omega\right\}. \qquad (6.1)$$

Here, C_v is the volumetric heat capacity, k is thermal conductivity, T is temperature, n is the number of phonon branches, ω_D is Debye frequency, $g(\omega)$ is phonon density of states, k_B is Boltzmann constant, ħ is reduced Planck constant, ω is the phonon frequency, v_ω is the phonon group velocity, τ_{ph} is the relaxation time for phonon-phonon scattering, and τ_{struc} is the relaxation time for phonon-structural imperfection scattering. To the first-

order approximation, the inverse thermal diffusivity can be used to estimate the relative contribution of scattering sources.[194,195] The temperature-dependent thermal conductivity of the superlattice and bulk Ga_2O_3 have different trends with temperature. The strong temperature dependence of heat capacity makes it difficult to compare the contribution of phonon-phonon scattering and phonon-structural imperfection scattering according to the thermal conductivity data. After removing the effect of heat capacity, the inverse thermal diffusivity represents the relative contributions of phonon scattering sources qualitatively. As shown in Figure 6.3(a), the inverse thermal diffusivity decreases with decreasing temperature because of reduced scattering intensity of phonon-phonon scattering. As temperature goes to zero, phonon-phonon scattering diminishes and only structural imperfection scattering remains. Then Equation (6.1) can be simplified as:

$$\frac{C_v}{k}(T \to 0\ \mathrm{K}) \approx \frac{3}{v_0^2 \tau_{struc}} = \frac{3}{v_0 l_0}. \qquad (6.2)$$

Here, v_0 is the average phonon group velocity and l_0 is the scattering length arising from structural imperfections. For the bulk Ga_2O_3, the structural imperfection is negligible so nearly zero residual value is observed at low temperatures. However, a large residual value is observed at low temperatures for the superlattice, indicating strong structural imperfection scattering, such as alloy scattering, boundary scattering, and point defect scattering. We estimate the average acoustic phonon group velocity as 2420 m/s.[193] Based on the residual inverse thermal diffusivity (40 s/cm^2), the structural scattering length l_0 can be calculated as 3.1 nm, which is close to the layer thickness of the superlattice by considering additional alloy scattering. The rough interfaces in the superlattice may reduce

the effective thermal conductivity because the roughness at the interfaces may induce additional phonon scattering.[196]

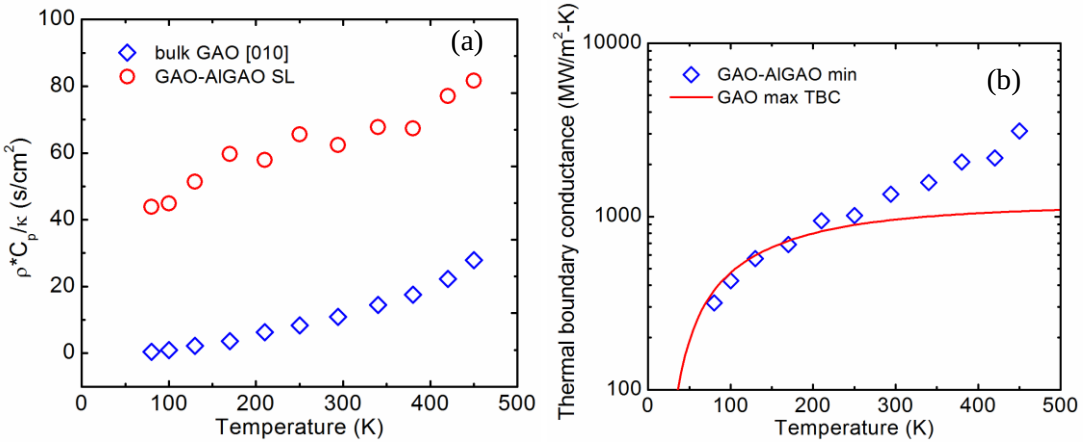

Figure 6.3. (a) Temperature-dependent inverse thermal diffusivity of bulk (010) Ga_2O_3 and β-$(Al_{0.1}Ga_{0.9})_2O_3/Ga_2O_3$ superlattices. (b) Temperature dependence of estimated minimum TBC (lower bound) of β-$(Al_{0.1}Ga_{0.9})_2O_3$ and Ga_2O_3 interfaces and maximum TBC of Ga_2O_3.

To understand the mechanism of phonons transmission through $(Al_{0.1}Ga_{0.9})_2O_3/Ga_2O_3$ interfaces, we estimate the TBC as below:

$$R_0 + \frac{n}{TBC} = \frac{114\ nm}{k_{measured}}. \qquad (6.3)$$

Here, R_0 is the superlattice thermal resistance of $(Al_{0.1}Ga_{0.9})_2O_3/Ga_2O_3$ without considering the TBR. n is the number of interfaces. TBC in this case refers to the TBC of the $(Al_{0.1}Ga_{0.9})_2O_3/Ga_2O_3$ interfaces. $k_{measured}$ is the measured effective thermal conductivity of the superlattice. R_0 is supposed to be higher than the thermal resistance of pure Ga_2O_3 with the same thickness because of the alloy scattering.[24,28,197]. Here, we only consider the size effect resulting from total superlattice thickness (114 nm), the thermal conductivity

reduces to 45% according to first-principle calculations.[193] As a result, the minimum TBC of the $(Al_{0.1}Ga_{0.9})_2O_3/Ga_2O_3$ interface could be estimated by assuming R_0 as the thermal resistance of a 114-nm-thick pure Ga_2O_3 layer. It is notable that the estimation of minimum TBC is based on the assumption of incoherent phonon transport across interfaces. This assumption will be checked later. To compare with this estimated TBC, we also calculate the max TBC of any heterogeneous interfaces which involving Ga_2O_3. This max TBC is calculated by assuming the phonon transmission coefficient across the interface as unity (all phonons from Ga_2O_3 could transmit through the interface). The definition of TBC can be described as below.[53,64]

$$G = \frac{1}{4}\sum_j \int v_w c_w t_w dw_j \qquad (6.4)$$

Here, v_w, c_w, and t_w are phonon group velocity, heat capacity per frequency, and transmission probability on one side of the interface for polarization j.[64] Max TBC is the value of G when t_w is unity. As shown in Figure 6.3(b), the estimated minimum TBC is larger than the max TBC of Ga_2O_3 interfaces, especially at high temperatures. At 450 K, the minimum TBC is almost three times larger than the max Ga_2O_3 TBC. This means that the incoherent phonon conduction assumption does not hold and some phonons transmit through several interfaces before scattering with other phonons or structural imperfections. The comparison of the estimated minimum TBC and the max TBC shows the evidence of phonon coherence. Some phonons do not scatter with interfaces as expected by the definition of TBC based on incoherent phonon transport. At low temperatures, the minimum TBC should be much larger than the max TBC because phonon mean free paths at low temperatures are much larger than that at room temperature. Phonons could transmit

through more interfaces without scatterings. But we overestimate the thermal conductivity of the superlattice at low temperatures significantly, resulting in a small minimum TBC. Here, the estimated TBC is the thermal energy transmitted across the interface for a certain temperature difference per unit area. Because the period of the superlattice is very small comparing with some long mean free path phonons, some phonons could transmit across several interfaces without scattering with other phonons and structural imperfections. The energy of these phonons are accounted repeatedly for several times, resulting in a very large effective TBC, even larger than the max TBC Ga_2O_3 heterointerfaces could achieve. This non-local and non-equilibrium phonon transport across interfaces is one of the challenges to define local temperature and understand thermal transport across interfaces. Similar phenomenon was observed in AlN-GaN superlattices before.[61] Our work is important since it may be necessary to design the superlattices not only for the creation of the channel 2DEG, but also for more efficient thermal dissipation through the structure. This electro-thermal co-design is truly an important feature for future wide bandgap devices which require enhancements in heat dissipation within the devices.

6.4 Conclusions

This work reports the first temperature-dependent measurement on thermal conductivity of β-$(Al_{0.1}Ga_{0.9})_2O_3/Ga_2O_3$ superlattices from 80 K to 480 K. We observed significantly reduced thermal conductivity (5.7 times reduction) at room temperature comparing with bulk Ga_2O_3. The thermal conductivity of bulk (010) Ga_2O_3 is measured and found to be consistent with literature values. By calculating the inverse thermal diffusivity of both the superlattice and bulk Ga_2O_3, we qualitatively identify the relative contribution of scattering intensity of phonon-phonon scattering and phonon-structural

imperfection scattering. We estimated the scattering length as 3.1 nm, which is close to the layer thickness of the superlattice by considering additional alloy scattering. The estimated minimum TBC of β-$(Al_{0.1}Ga_{0.9})_2O_3/Ga_2O_3$ interfaces is found to be larger than the Ga_2O_3 maximum TBC. This result shows that some phonons could transmit through several interfaces before scattering with other phonons or structural imperfections. This study is not only important for Ga_2O_3 electronics applications especially for high power and high frequency applications, but also for the fundamental thermal science of phonon transport across interfaces and in superlattices.

CHAPTER 7. THERMAL CONDUCTANCE ACROSS B-Ga_2O_3-DIAMOND INTERFACES

7.1 Introduction

As an emerging ultra-wide bandgap semiconductor material, β-Ga_2O_3 has shown favorable properties for use in power electronics applications, such as an ultra-wide bandgap (4.8 eV) and high critical electric field (8 MV/cm), which predict a Baliga figure of merit that is 3214 times that of Si.[38] However, the thermal conductivity of bulk β-Ga_2O_3 (10-30 W/m-K, depending on crystal orientation) is at least one order of magnitude lower than those of other wide bandgap semiconductors, for instance, GaN (230 W/m-K), 4H-SiC (490 W/m-K), and diamond (>2000 W/m-K).[2,198] To utilize Ga_2O_3 in high frequency and high power switching applications, proper thermal management is essential to avoid device degradation due to poor thermal reliability. This will require the use of high thermal conductivity pathways to pull the heat out of the Ga_2O_3 devices efficiently through interfacial contacts with low thermal boundary resistance. With its ultra-high thermal conductivity, diamond, which has been extensively studied to dissipate localized self-heating from electronics such as AlGaN/GaN HEMTs, is a possible solution for Ga_2O_3 devices as well.[12,28,189,199]

Recently, mechanically exfoliated Ga_2O_3 nano-membranes have been utilized to fabricate high-current transistors.[200-205] A record high drain current has been achieved in an exfoliated Ga_2O_3 field-effect transistor with diamond substrates.[206] This work demonstrates good device performance but has not quantified the heat transport across the Ga_2O_3-diamond interface as the Ga_2O_3 nano-membranes were adhered to diamond via Van

der Waals forces. The TBC of mechanically joined materials could be as low as 0.1 MW/m^2-K while the interfacial thermal conductance of transfer-printed metal films is in the range of 10-40 MW/m^2-K.[76,207-210] Thermal transport across Van der Waals interfaces is limited by the real contact area and low phonon transmission due to weak adhesion energy even if there exists the possibility to achieve a high TBC.[66,211,212] Thermal transport across these interfaces remains an open issue due to the limited amount of experimental data available in the literature. Therefore, it is of great significance to study the thermal conductance across Ga_2O_3-diamond interfaces for both real-world power electronics applications and fundamental thermal science of heat transport across Van der Waals interfaces.

7.2 Transferred Ga_2O_3 on Single Crystal Diamond

In this work, we have mechanically exfoliated a (100) oriented Ga_2O_3 nano-membrane from an EFG-grown commercial (-201) Ga_2O_3 substrate (Novel Crystal Technology, Japan) with medium-tack dicing saw tape and transferred it on a single crystal (100) CVD diamond substrate (Element Six).[213] TDTR was used to measure the Ga_2O_3-diamond TBC and Ga_2O_3 thermal conductivity. Moreover, by combining picosecond acoustic technique and the membrane thickness measured by an Atomic Force Microscopy (AFM), the phonon group velocity across the membrane thickness direction is obtained. Moreover, we use a Landauer approach to calculate phonon transport across Ga_2O_3-diamond interfaces. Additionally, the effects of Ga_2O_3-substrate TBC and substrate thermal conductivity on thermal performance of a power electronics are modelled by an analytical solution.

Figure 7.1(a) shows a part of the sample scanned by AFM. A blanket layer of Al (~80 nm) was deposited to serve as the TDTR transducer. As the size of the Ga_2O_3 nano-membrane was approximately 11 μm x 70 μm, a CCD camera integrated in the TDTR system was used to help locate the sample. To obtain the thermal conductivity of the diamond substrate, TDTR was performed on the area which was not covered by the Ga_2O_3 nano-membrane. The thermal conductivity of the single crystal diamond substrate was determined to be 2169 ±130 W/m-K, which is very close to other values reported in the literature.[214] This value was used in the data analysis and parameter fittings from the TDTR measurements on the Ga_2O_3 bonded to diamond. The Al-diamond TBC is also determined in the measurement to be 34 MW/m^2-K. Figure 7.1(b) shows the picosecond acoustic echoes obtained during TDTR measurements. The observed echoes correspond to strain waves that are reflected at interfaces.[125] Figure 7.1(c) shows the strain wave traveling distance for each echo. For echo 1, a small valley shows up before a peak, indicating the loose bonding of Van der Waals forces at the interface. In this scenario, we pick the middle point of the valley and peak as the echo point (t_1=25 ps).[125] The sound speed of Al is 6420 m/s[125] so the Al thickness was determined to be 80 nm ($d_1 = v_{Al} * t_1/2$). For echo 2 (154 ps=25 ps+129 ps), it relates to the Ga_2O_3-diamond interface. The travelling time in Ga_2O_3 is 129 ps. The thickness of the Ga_2O_3 layer was determined as 427±3 nm by an AFM. Then the longitudinal phonon group velocity of Ga_2O_3 in the direction perpendicular to (100) plane is determined as 6620 m/s, which matched very well with DFT-calculated value (6809 m/s) we will discuss more later. Echo 3 is the strain wave bouncing back from the Al-air interface after coming back from the Ga_2O_3-diamond interface. The strain wave

travels across Al layer again and bounces back from the Al-Ga_2O_3 interface. The traveling time equals 179 ps (=25 ps+129 ps+25 ps).

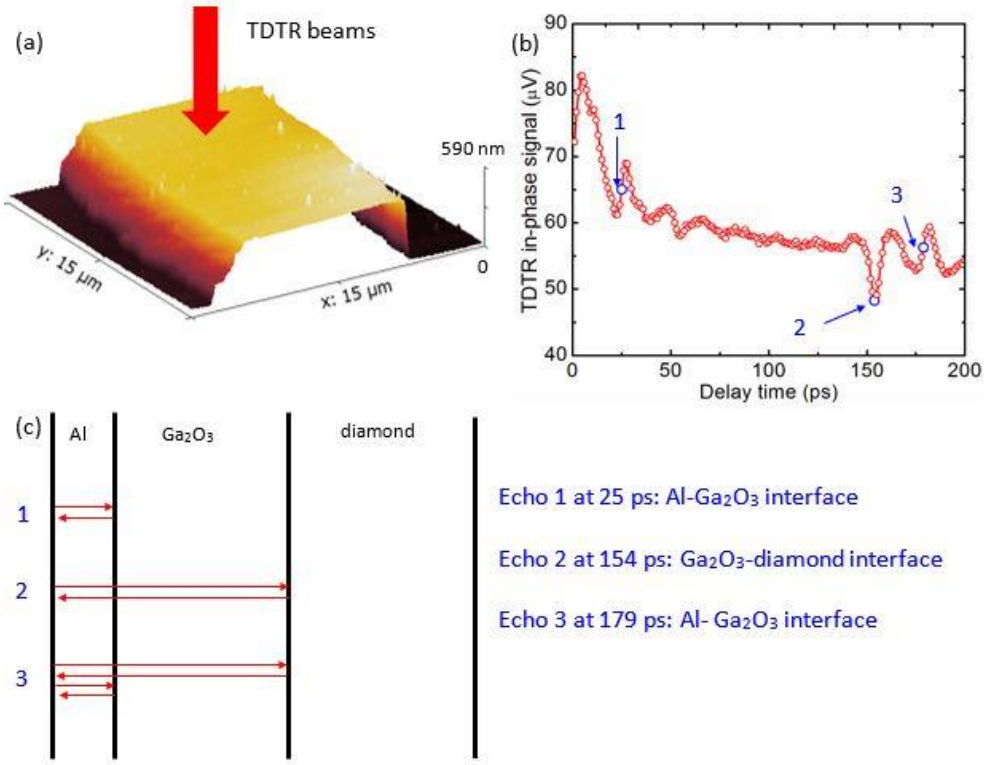

Figure. 7.1. (a) AFM image of the center of the Ga_2O_3 sample. (b) Picosecond acoustic echoes obtained in the TDTR measurements. (c) Echoes which relate to strain wave bouncing back at interfaces.

The surface roughness of the two surfaces affects the real contact area, and correspondingly, the thermal conductance across this interface. To measure the surface roughness, AFM was used to scan the diamond substrate surface and the top surface of the Ga_2O_3 membrane. The bottom surface of the Ga_2O_3 membrane should be similar to or smoother than the top surface.[215,216] The surface images are shown in Figure 7.2(a-b). The RMS roughness of diamond and Ga_2O_3 surfaces are 3.39 ±0.91 nm and 3.23±0.93 nm,

respectively. The sensitivity of our TDTR measurements was determined by considering a fractional change in the thermoreflectance signal due to a fractional change in the independent parameters.[28] Figure 7.2(c) shows the TDTR sensitivity of the TBC of the Ga_2O_3-diamond interface, thermal conductivity of the Ga_2O_3 membrane, and the TBC of the Al-Ga_2O_3 interface with a modulation frequency of 2.2 MHz and a 20 X objective (pump radius 4.9 μm and probe radius 3.0 μm). The sensitivity of the TBC of the Ga_2O_3-diamond interface is very large, resulting in accurate measurements of this parameter. Figure 7.2(d) shows good agreement between the experimental data (red circles) and the fitted curve (blue curve).

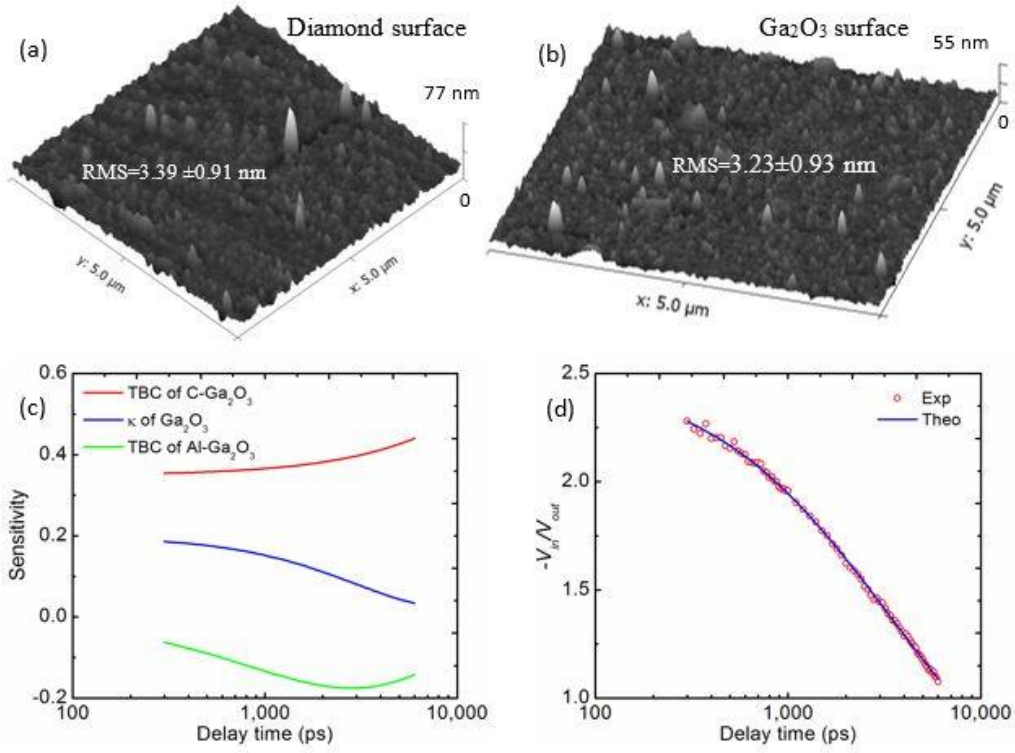

Figure 7.2. (a) AFM scanned surface roughness of the diamond substrate. (b) AFM scanned surface roughness of the top surface of the Ga_2O_3 nano-membrane. (c) TDTR sensitivity of TBC of the Ga_2O_3-diamond interface, thermal conductivity of Ga_2O_3, and the

TBC of Al- Ga_2O_3 interface with a modulation frequency of 2.2 MHz and a 20 X objective. (d) TDTR data fitting with modulation frequency of 2.2 MHz and 20 X objective.

The TBC of the Ga_2O_3-diamond interface was measured to be 17 -1.7/+2.0 MW/m^2-K and is compared with the TBC of several other diamond interfaces and transferred interfaces in Table 7.1. The error bars (low bar -1.7 MW/m^2-K and up bar +2.0 MW/m^2-K) of TDTR measurements is estimated by a Monte Carlo method.[46] The Ga_2O_3-diamond TBC is in the TBC range of the transferred metal films on silicon, SiO_2, and sapphire substrates (Van der Waals force bonded) and is comparable to the TBC of several physical-vapor-deposited metals on diamond (covalent force bonded). The Ga_2O_3-diamond TBC is mainly affected by three factors: the weak Van der Waals force between Ga_2O_3 and diamond (covalent bonding is much stronger), the small contact area at the interface, and the large phonon density of states (DOS) mismatch between Ga_2O_3 and diamond. For the Ga_2O_3-diamond interface, the two materials are bonded by the Van der Waals force. Interfacial bonding affects thermal conductance significantly.[94] For instance, the TBC of covalent bonded interfaces is much larger than that of the Van der Waals force bonded interfaces because phonon transmission is very low due to the weak adhesion energy of Van der Waals interfaces.[94,212,217] Moreover, diamond is non-polar, so no dipolar-dipolar attraction exists at the interface. The Van der Waals force at the Ga_2O_3-diamond interface should be weaker than those of other polar material interfaces. This further decreases the TBC. In terms of the real contact area at the interface, there are no good methods to measure it. Some calculations indicate that the fractional areal coverage of transferred metal films on silicon or sapphire substrates could reach 25% because of plastic deformation and capillary forces.[211] The transferred metal thin films (Au) are very soft so the contact area

between the metals and substrates could be very large under pressure during the transfer process. However, for the Ga_2O_3-diamond interface, diamond is known as one of the hardest materials and Ga_2O_3 is much harder than Au. We can see very small pillars forming surface roughness of both the Ga_2O_3 and diamond surfaces according to the AFM images. We speculate these pillars may enlarge the contact area at the interface and enhances thermal transport. Surface-roughness insensitive TBC was observed in Van der Waals interfaces before.[76] Our measured Ga_2O_3-diamond TBC is comparable to the TBC of several physical-vapor-deposited metals on diamond and reaches more than one fourth of the TBC of the chemical-vapor-deposited diamond on silicon even though the contact area of these deposited interfaces are much larger than that of Ga_2O_3-diamond interface. Diamond-Si TBC is higher than those of the other interfaces in Table 7.1 because of its large contact area and relatively good phonon DOS match.

Here, we define "diamond interface" as any interface one side of which is diamond. Diamond has ultra-high thermal conductivity due to the light carbon atom and strong covalent bond among carbon atom, which leads to an ultra-high Debye frequency and cutoff frequency. As a result, the phonon DOS match of diamond and other materials are very poor and the TBC of diamond interfaces are very low. When integrating diamond with other materials to take advantage of its high thermal conductivity, the low TBC of diamond interfaces is usually the bottleneck. This highlights the motivation to study thermal transport across diamond interfaces for both fundamental science and real-world applications. By taking all these into consideration, we could conclude that the measured Ga_2O_3-diamond TBC is relatively quite high. On one hand, this relatively high TBC helps to explain why a Ga_2O_3 field-effect transistor observed record-high drain current on

diamond.[206] On the other hand, it shows that thermal transport across Van der Waals interfaces are relatively good from a fundamental viewpoint.

Table 7.1. TBC of several diamond interfaces and transferred interfaces.

	Interfaces	**TBC** (MW/m^2-K)	**Fabrication Conditions**
Our work	Ga_2O_3-diamond	17	Transferred van der Waals interfaces
Ref.[76]	Au-Si/SiO_2/Al_2O_3	10-40	Transferred van der Waals interfaces
Ref.[85]	Bi-H-diamond	8	Physical vapor deposition
Ref.[85]	Pb-diamond	19	Physical vapor deposition
Ref.[85]	Pb-H-diamond	15	Physical vapor deposition
Ref.[189]	Si-diamond	63	Chemical vapor deposition

The thermal conductivity of the Ga_2O_3 nano-membrane was measured as 8.4 ±1.0W/m-K, which is lower than the value of bulk Ga_2O_3 in this direction (about 13 W/m-K).[198] The anisotropic crystal structure results in anisotropic properties.[192,218] Here, TDTR is more sensitive to cross-plane thermal conductivity instead of in-plane ones. The thickness dependent thermal conductivity of Ga_2O_3 thin films from literature and this work are summarized in Figure 7.3. For a certain crystal orientation, the thermal conductivity of Ga_2O_3 thin films decreases with film thickness. The phonon mean free path in bulk Ga_2O_3 ranges from several nm to several um.[193] Phonons with long mean free path scatter with film boundaries. The additional film boundary scattering reduces phonon mean free path and reduces thermal conductivity. For instance, the thickness of our Ga_2O_3 nano-membrane is 427 nm. The phonons with mean free path larger than 427 nm have large possibility to scatter with the film boundaries. The film boundary scattering limits the phonon mean free

path in the cross-plane direction and correspondingly reduces cross-plane thermal conductivity. Size effects in nanoscale Ga_2O_3 electronics would result in further-reduced thermal conductivity, leading to heat dissipation problems in these devices. This highlights the demand of proper thermal management for Ga_2O_3 electronics.

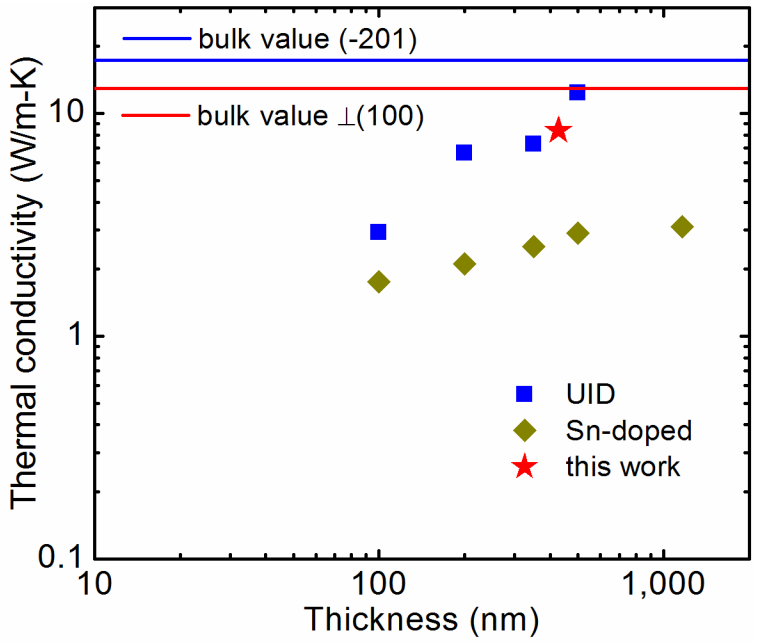

Figure 7.3. Thickness dependent thermal conductivity of Ga_2O_3 thin films. The data for the unintentionally doped (UID) and Sn-doped (-201) orientated thin films is from reference.[219] The blue and red lines are the bulk values in (-201) orientation and perpendicular to (100) orientation.[198,219]

The calculated phonon transmission coefficients based a Landauer approach are shown in Figure 7.4 (a). The phonon properties of diamond are obtained from first principles calculation with VASP, and the phonon properties of Ga_2O_3 are from Materials Project.[220-222] The low transmission coefficients at low frequency is derived from the acoustic branches. The number of phonon modes of three dimensional material is

proportional to the square of wavenumber, which equals to phonon angular frequency over group velocity for acoustic branches at low frequency, as the phonon dispersion relation is almost linear near the Gamma point. For the longitudinal acoustic (LA) polarization, the phonon group velocity of diamond perpendicular to the (100) plane is 17553 m/s, while the phonon group velocity of Ga_2O_3 perpendicular to the (100) plane is 6809 m/s, which means that the group velocity of diamond is 2.58 times that of Ga_2O_3, and the number of modes of diamond LA at low frequencies is only 15% of that of Ga_2O_3. As a result of the large difference between the acoustic group velocities, the phonon transmission coefficient is very low at low frequencies. For most interfaces involving diamond, the transmission is usually low because of the large phonon group velocity and high cutoff frequency of diamond. At high frequencies, the wavenumber of Ga_2O_3 at a certain frequency is relatively close to that of diamond, and the transmission coefficient increases.

The calculated TBC from the Landauer approach is 312 MW/m^2-K as shown in Figure 7.4 (b) at the Ga_2O_3 cutoff frequency. Because of the complex crystalline structure (large unit cell) of Ga_2O_3, there are a large number of optical phonon modes. As a result, acoustic phonons of Ga_2O_3 only contribute to about 8% of the total TBC while optical phonons contribute to about 92%. The calculated TBC is significantly larger than the measured value. The difference between the theoretical TBC and the measured TBC is attributed to the interfacial bonding and real contact area at the interface as discussed above. The van der Waals bonding at Ga_2O_3-diamond interface is much weaker than covalent bonds, which reduces TBC significantly.[76,94,211,217] We also calculated the radiation limit of TBC of Ga_2O_3-diamond interface as 426 MW/m^2-K.[53,223] The radiation limit assumes the phonon transmission coefficient as one from one side of the interface to

the other side when phonons at a certain frequency from that side have lower number of modes. Phonon density of states of Ga_2O_3 and diamond are from their phonon dispersion relations. Both DMM-based Landauer and radiation limit cannot capture inelastic scatterings, however, the calculated results shed light on the possible TBC with perfect interface, which guide the material growth and device design.

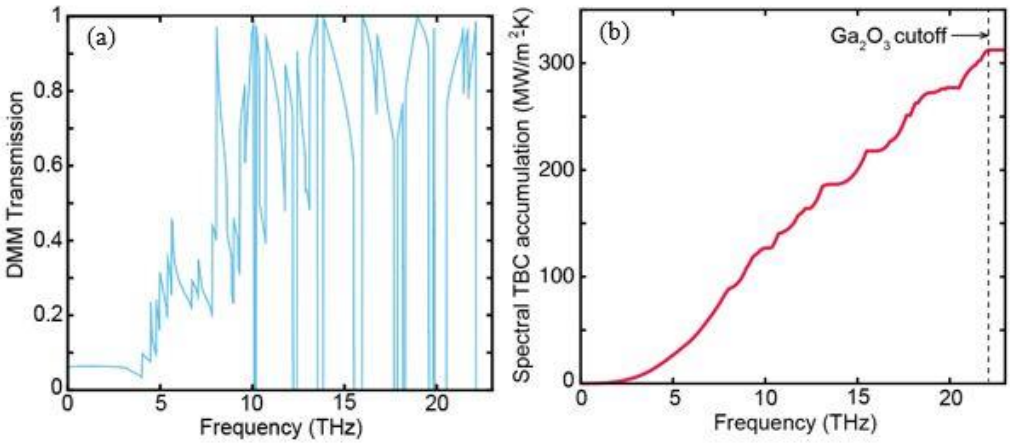

Figure 7.4. (a) The transmission coefficient from DMM at Ga_2O_3-diamond interface. (b) The spectral TBC accumulation at Ga_2O_3-diamond interface from Landauer approach.

To understand the impact of the Ga_2O_3–substrate TBC on the thermal performance of a power device, we use an analytical solution for the temperature rise in multilayer structures with discrete heat sources.[135] The modeled device consisted of a 500-nm (100) Ga_2O_3 layer atop a substrate consisting of either high quality diamond, SiC, or Si. The Ga_2O_3 layer was prescribed an anisotropic thermal conductivity with k_z = 12 W/m-K and k_r = 21 W/m-K in accordance with published values.[193] The modeled device structure was a 10 finger device with 50 µm gate-to-gate spacing. The heat sources were each assumed to be 4 x 150 µm and the total domain was 2000 x 2000 µm. A total power density of 10 W/mm was applied to the simulated device. The device structure and simulated heating

can be seen in Figure 7.5 (a-b). Figure 7.5(a) shows the schematic diagram of the modeled device demonstrating the cross section and heat source spacing. Figure 7.5(b) shows the top view of the simulated device (a Ga_2O_3-diamond TBC of 100 MW/m^{2}K on a diamond substrate with a thermal conductivity of 2000 W/m-K). As expected, the applied power leads to an increase in peak temperature at each Ga_2O_3 finger.

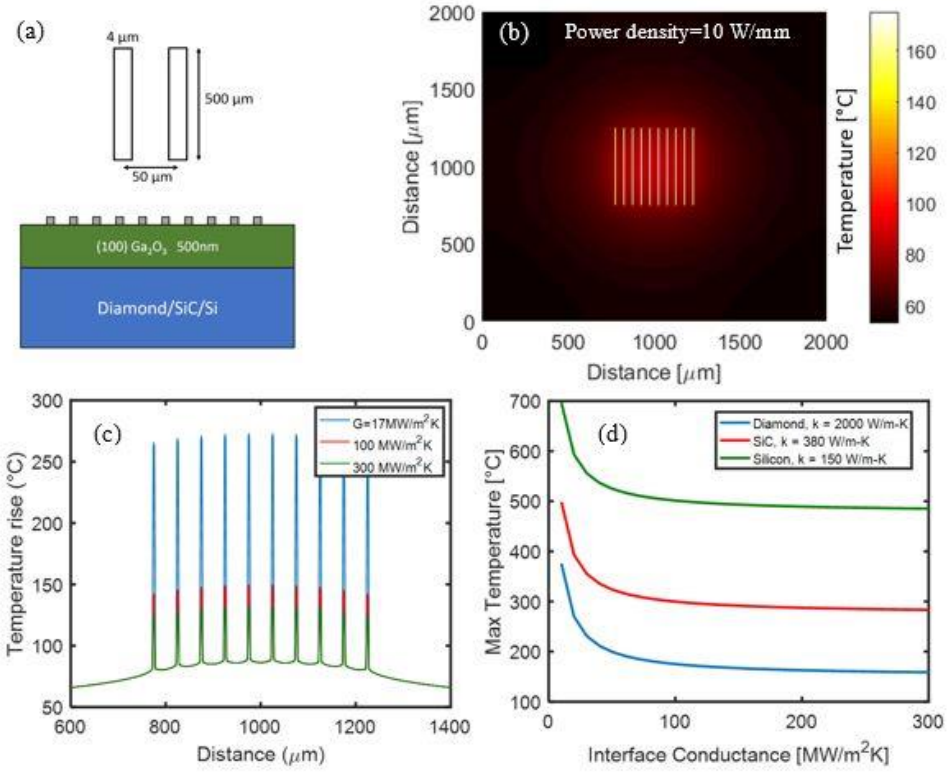

Figure 7.5. (a) Schematic of the modeled device. (b) Top view temperature field of the simulated device. (c) Heating profile of Ga_2O_3 on diamond devices with a TBC value of 17, 100, and 300 MW/m^{2}K, respectively. (d) The maximum temperature of the device for a diamond, SiC, or Si substrate as a function of varying TBC between Ga_2O_3 and substrates.

The impact of the Ga_2O_3-substrate TBC was evaluated by adjusting its value in the model from 10 to 300 MW/m^{2}K for each substrate material. Figure 7.5(c) shows the device

temperature distribution across the center of the fingers for a simulated Ga_2O_3 on diamond device with a TBC value of 17, 100, and 300 MW/m^{2}K, respectively. The decrease in TBC would increase the temperature rise significantly, especially when the TBC is not large. As shown in Figure 7.5(d), when the Ga_2O_3-substrate TBC is small, TBC is the dominant factor limiting heat dissipation. When TBC goes beyond 70 MW/m^2-K, substrate thermal conductivity is the dominant factor which limits device thermal dissipation. Additionally, as long as the TBC value is not too low, it is crucial to have a high thermal conductivity substrate. For instance, a SiC substrate with a TBC of 300 MW/m^{2}K shows a maximum temperature of 283 °C, while using a diamond substrate with a TBC of 17 MW/m^{2}K (much lower than 300 MW/m^{2}K), as measured in this work, results in a similar maximum temperature rise. This result demonstrates the importance of implementing a high thermal conductivity substrate such as diamond into Ga_2O_3 power devices. Because of the relatively low thermal conductivity of Ga_2O_3, even a relatively low TBC value (but equal to or larger than 17 MW/m^{2}K) for a device on diamond will outperform a device on a SiC substrate with an exceptional TBC. This will be useful in guiding device design when integrating Ga_2O_3 with high thermal conductivity substrates.

7.3 Atomic-Layer-Deposited Ga_2O_3 on Single Crystal Diamond

ALD growth relies on the sequential self-limiting reactions between surface adsorbed metal organic molecules and oxidizing molecules. Single crystalline (100) diamond substrates were obtained commercially (Element Six, thermal grade) and cleaned using a sequence of treatments intended to remove metal and non-diamond carbon contamination: HNO_3:HCl, HNO_3:H_2SO_4, ultrasonic clean in ethanol, and finally an HF etch. The substrates were stored in ethanol and were dried in N_2 immediately prior to

transfer into the Ga_2O_3 growth reactor. Thin films (~30-115 nm) were deposited on single crystal (100) diamond substrates in a Fiji 200 G2 reactor at 295°C using alternating cycles of trimethylgallium (TMG, STREM PURATREM) as the Ga precursor and a remote pure oxygen plasma as the oxidizing source. All samples utilized a turbo pump to drop the pressure in the chamber to 8 mTorr during plasma exposure. Under these conditions, the growth rate was 0.65Å/cycle. All the samples are undoped.

To measure the thermal conductivity of the Ga_2O_3 film, a thick sample (about 120 nm Ga_2O_3) was grown on a single crystal diamond substrate (Samp1). Since this layer is too thick for our thermal measurement system to be sensitive to the interface TBC, thinner (~30nm) layers of Ga_2O_3 were grown onto other diamond substrates. In addition, the diamond substrates were given different in-situ surface pretreatments prior to growth to investigate the effect on TBC. The surface of Samp2 was pretreated with a Ga flashoff process to emulate the one typically used to clean surfaces in MBE. This consists of dosing with TMG to create a gallium sub-oxide at the surface that is subsequently exposed and removed with a hydrogen plasma pulse. The surface of Samp3 was initiated by super saturating with 10 consecutive Ga pulses prior to growth, while the surface of Samp4 received 10, 10s O_2 plasma pulses in-situ treatment prior to growth. The details of each sample is summarized in Table 7.2. A layer of Al (~84 nm) was deposited on the sample surface as a transducer for TDTR measurements. The thickness of the Al layer was determined by the picosecond acoustic technique during TDTR measurements. The thickness of Ga_2O_3 films are determined with TEM.

A modulated pump beam (400 nm) heats the sample surface while a delayed probe beam (800 nm) detects the temperature variation of the sample surface. After being picked

up by a photodetector and a lock-in amplifier, the signal is fitted with an analytical heat transfer solution to infer the unknown parameters.[74,105,190,224] Each of the four samples in this work includes three layers: an Al layer, a Ga_2O_3 layer, and a diamond substrate. The thermal conductivity of a bare single crystal diamond substrate was measured as 2169 W/m-K first and then input as a known parameter in the data fitting of the Ga_2O_3-on-diamond samples. There are three unknown parameters: the Ga_2O_3-diamond TBC, the Ga_2O_3 thermal conductivity, the Al-Ga_2O_3 TBC. The heat capacity of Al, Ga_2O_3 and diamond used in the data fitting are from literature.[21,74,224] The values reported in this work are average values of four different spots measured on each sample with modulation frequencies of 3.6 MHz and 6.3 MHz. The standard derivations of the measured TBC of each sample are smaller than 8% (eight measurements per sample). The pump and probe diameters are 19.0 μm and 13.3 μm. The experimental data is fitted with an analytical heat transfer solution of the three-layer structure to infer the unknown parameters. The detailed derivation of the analytical heat transfer solution can be found in references.[41,42]

Table 7.2. Sample structures and thermal properties

	Al	**Ga_2O_3**	**Diamond surface pretreatment**	**Ga_2O_3-C TBC**	**Ga_2O_3 *k***
Samp1	88 nm	115 nm	N/A	N/A	1.76 W/m-K
Samp2	84 nm	29 nm	Ultra-clean	179 MW/m2-K	1.50 W/m-K
Samp3	84 nm	30 nm	Ga-rich	136 MW/m2-K	1.50 W/m-K
Samp4	84 nm	28 nm	O-rich	139 MW/m2-K	1.52 W/m-K

As shown in Table 7.2, the measured thermal conductivity of Samp1 is 1.76 W/m-K, which is much lower than that of bulk β-Ga_2O_3 (10-30 W/m-K).[40] The Ga_2O_3 film is

polycrystalline with grains on the order of 10-20nm. The measured TBC of the ultra-clean (Samp2) interface is 179 MW/m^2-K, about 10 times higher than TBC of a Van der Waals bonded Ga_2O_3-diamond interface, suggesting that covalent bonding facilitates interfacial heat transport better than Van der Waals interfacial bonding.[74] While the other two thinner samples have smaller TBC due to different in-situ pretreatments of the diamond surfaces, they are still much larger than the Van der Waals bonded TBC. This confirms that the type of interface bonding affects TBC significantly, similar to metal-quartz interfaces reported before.[94] Interface chemistry affects the local vibrational modes, resulting in different phonon transport mechanisms at the interface and correspondingly different TBC. Like epitaxy, room-temperature surface activated bonding (SAB) technique bonds independently grown layers with covalent chemical bonding interfaces, resulting in high TBC.[21] Thus, from the results shown here, we expect SAB Ga_2O_3-related interfaces should have high TBC, enabling another possible approach for integrating high-quality β-Ga_2O_3 with high thermal conductivity substrates such as SiC and diamond. Therefore, interface chemistry and bonding are important factors which affects interfacial thermal transport, similar to Al-diamond interfaces reported previously in the literature.[90]

7.4 Conclusions

A possible solution to cool Ga_2O_3 electronics is to integrate thin Ga_2O_3 membranes with diamond to fabricate Ga_2O_3-on-diamond devices by taking advantage of the ultra-high thermal conductivity of diamond. A good understanding of the TBC between Ga_2O_3 and diamond is still lacking. In this work, we measured the TBC of the interfaces of smooth exfoliated Ga_2O_3 and polished single crystal diamond. The longitudinal phonon group velocity in the direction perpendicular to the (100) plane of Ga_2O_3 is 6620 m/s, which

matched very well with DFT-calculated value (6809 m/s). Reduced thermal conductivity of the Ga_2O_3 nano-membrane (8.4 ±1.0W/m-K) was observed and attributed to size effects (phonon-boundary scatterings). The Van der Waals Ga_2O_3-diamond TBC was measured to be 17 -1.7/+2.0 MW/m^2-K, which is in the TBC range of transfer-printed metal films and comparable to the TBC of several physical-vapor-deposited diamond interfaces. This value is relatively quite high by taking the weak bonding strength and small contact area into consideration. The TBC calculated with a Landauer approach and DMM is 312 MW/m^2-K, which sheds light on the possible TBC we can achieve. Additionally, we grow Ga_2O_3 on diamond by ALD. The measured TBC of the ultra-clean interface is 179 MW/m^2-K, about 10 times higher than TBC of a Van der Waals bonded Ga_2O_3-diamond interface, suggesting that covalent bonding facilitates interfacial heat transport better than Van der Waals interfacial bonding.

CHAPTER 8. SUMMARY AND CONCLUSIONS

8.1 Summary of Contributions

This thesis shows a new method (room-temperature surface-activated bonding technique) to integrate ultrawide and wide bandgap semiconductors with high thermal boundary conductance. The bonding of GaN with SiC and single crystal diamond were demonstrated to achieve high TBC to facilitate excellent heat dissipation of power and RF electronics. This results will also push forward the development of 3D microchips packing in which thermal management is one of the key challenges. Additionally, nanoscale graphoepitaxy is used to enhance both the thermal conductivity of CVD diamond and Si-diamond TBC significantly, which sheds light on enhancing the TBC of diamond related interfaces.

The temperature-dependence of thermal conductivity of β-$(Al_{0.1}Ga_{0.9})_2O_3/Ga_2O_3$ superlattices were measured and significantly reduced thermal conductivity (5.7 times reduction) at room temperature was observed comparing with bulk Ga_2O_3. The estimated minimum TBC of β-$(Al_{0.1}Ga_{0.9})_2O_3/Ga_2O_3$ interfaces is found to be larger than the Ga_2O_3 maximum TBC, which shows that some phonons could transmit through several interfaces as possible evidence of phonon coherence. To address the challenges of thermal management of Ga_2O_3-based devices, Ga_2O_3 was integrated with single crystal diamond by exfoliation-transferring and ALD-growth. The Van der Waals Ga_2O_3-diamond TBC was measured to be 17 -1.7/+2.0 MW/m^2-K while the TBC calculated with a Landauer approach and DMM is 312 MW/m^2-K, which sheds light on the possible TBC achievable. The measured TBC of the grown ultra-clean interface is 179 MW/m^2-K, about 10 times

higher than TBC of a Van der Waals bonded Ga_2O_3-diamond interface, suggesting that covalent bonding facilitates interfacial heat transport better than Van der Waals interfacial bonding.

8.2 Future Work

This thesis shows excellent interfacial thermal conductance across new bonded interfaces. This bonding methods can be applied to other interfaces as well and possibly solve the thermal problems of semiconductor interfaces. The detailed understanding of phonon transport across these bonded interfaces is still lacking. The bonding method opens a door for creating heterogeneous interfaces which are impossible before by growth. The local chemistry of the bonded interfaces can be tuned, making them an excellent platform to stimulate the development of new theories of interfacial heat transfer. The Ar distribution can be controlled by annealing and can be replaced by other ions. All these will enable both theoretical and experimental studies of thermal physics in these interfaces.

Recording high TBC is expected for some interfaces such as diamond-silicon, silicon and germanium. Si can be bonded to diamond and Ge easily with any oxide and contamination, which is very difficult for any growth methods. Molecular dynamic simulation has available potentials for Ge, diamond and Si. The combination of measurements and modeling could advance the field significantly.

In terms of the applications, device fabrication needs to be demonstrated to show the excellent performance. For integration of Ga_2O_3 with high thermal conductivity substrates, surface activated bonding can be used with the help of ion-implantation-based smart-cut technique which exfoliates wafer-scale thin Ga_2O_3 membrane. Furthermore,

devices can be fabricated on these exfoliated thin Ga_2O_3 membranes which have been bonded on high thermal conductivity substrates. GaN-on-diamond devices based on the bonding technique should be fabricated to take the full advantage of the high thermal conductivity of single crystal diamond.

Additionally, for thermal measurements, transducer-less TDTR or other modifications need to be developed to gain better sensitivity of the TBC of buried interfaces. High-throughput measurements and TBC mapping are in demand to build a large TBC database which will stimulate the study of big data and machine learning about thermal science and engineering applications.

REFERENCES

1 Tsao, J. *et al.* Ultrawide-Bandgap Semiconductors: Research Opportunities and Challenges. *Advanced Electronic Materials* **4**, 1600501 (2018).

2 Pearton, S. *et al.* A review of Ga2O3 materials, processing, and devices. *Applied Physics Reviews* **5**, 011301 (2018).

3 Kneissl, M., Seong, T.-Y., Han, J. & Amano, H. The emergence and prospects of deep-ultraviolet light-emitting diode technologies. *Nature Photonics* **13**, 233 (2019).

4 Amano, H. *et al.* The 2018 GaN power electronics roadmap. *Journal of Physics D: Applied Physics* **51**, 163001 (2018).

5 Higashiwaki, M., Sasaki, K., Kuramata, A., Masui, T. & Yamakoshi, S. Gallium oxide (Ga2O3) metal-semiconductor field-effect transistors on single-crystal β-Ga2O3 (010) substrates. *Applied Physics Letters* **100**, 013504 (2012).

6 Lu, B., Piedra, D. & Palacios, T. in *The Eighth International Conference on Advanced Semiconductor Devices and Microsystems.* 105-110 (IEEE).

7 Wu, Y.-F., Moore, M., Saxler, A., Wisleder, T. & Parikh, P. in *2006 64th Device Research Conference.* 151-152 (IEEE).

8 Cho, J. *et al.* Improved thermal interfaces of GaN–diamond composite substrates for HEMT applications. *IEEE Transactions on Components, Packaging and Manufacturing Technology* **3**, 79-85 (2013).

9 Faili, F., Palmer, N. L., Oh, S. & Twitchen, D. J. in *ITherm* (Orlando, Florida, US, 2017).

10 Suckling, C. & Nguyen, D. in *ARMMS Conference of RF and Microwave Society.*

11 Pomeroy, J. W., Bernardoni, M., Dumka, D., Fanning, D. & Kuball, M. Low thermal resistance GaN-on-diamond transistors characterized by three-dimensional Raman thermography mapping. *Applied Physics Letters* **104**, 083513 (2014).

12 Yates, L. *et al.* in *Compound Semiconductor Integrated Circuit Symposium (CSICS), 2016 IEEE.* 1-4 (IEEE).

13 Rougher, T. L. *et al.* in *Thermal and Thermomechanical Phenomena in Electronic Systems (ITherm), 2017 16th IEEE Intersociety Conference on.* 30-38 (IEEE).

14 Cheaito, R. *et al.* in *Thermal and Thermomechanical Phenomena in Electronic Systems (ITherm), 2017 16th IEEE Intersociety Conference on.* 706-710 (IEEE).

15 Anaya, J. *et al.* Simultaneous determination of the lattice thermal conductivity and grain/grain thermal resistance in polycrystalline diamond. *Acta Materialia* (2017).

16 Berman, R. Thermal conductivity of isotopically enriched diamonds. *Physical Review B* **45**, 5726 (1992).

17 Graebner, J. *et al.* Anisotropic thermal conductivity in chemical vapor deposition diamond. *Journal of applied physics* **71**, 5353-5356 (1992).

18 Graebner, J., Jin, S., Kammlott, G., Herb, J. & Gardinier, C. Unusually high thermal conductivity in diamond films. *Applied physics letters* **60**, 1576-1578 (1992).

19 Graebner, J. *et al.* Phonon scattering in chemical-vapor-deposited diamond. *Physical Review B* **50**, 3702 (1994).

20 Manoi, A., Pomeroy, J. W., Killat, N. & Kuball, M. Benchmarking of thermal boundary resistance in AlGaN/GaN HEMTs on SiC substrates: Implications of the nucleation layer microstructure. *IEEE Electron Device Letters* **31**, 1395-1397 (2010).

21 Mu, F. *et al.* High Thermal Boundary Conductance across Bonded Heterogeneous GaN-SiC Interfaces. *arXiv preprint arXiv:1905.04171* (2019).

22 Cho, J. *et al.* Phonon scattering in strained transition layers for GaN heteroepitaxy. *Physical Review B* **89**, 115301 (2014).

23 Pengelly, R. S., Wood, S. M., Milligan, J. W., Sheppard, S. T. & Pribble, W. L. A review of GaN on SiC high electron-mobility power transistors and MMICs. *IEEE Transactions on Microwave Theory and Techniques* **60**, 1764-1783 (2012).

24 Sood, A. *et al.* Anisotropic and inhomogeneous thermal conduction in suspended thin-film polycrystalline diamond. *Journal of Applied Physics* **119**, 175103 (2016).

25 Anaya, J. *et al.* Control of the in-plane thermal conductivity of ultra-thin nanocrystalline diamond films through the grain and grain boundary properties. *Acta Materialia* **103**, 141-152 (2016).

26 Goodson, K. E. Thermal conduction in nonhomogeneous CVD diamond layers in electronic microstructures. *Journal of Heat Transfer* **118**, 279-286 (1996).

27 Bozorg-Grayeli, E. *et al.* Thermal conduction inhomogeneity of nanocrystalline diamond films by dual-side thermoreflectance. *Applied Physics Letters* **102**, 111907 (2013).

28 Cheng, Z. *et al.* Probing Growth-Induced Anisotropic Thermal Transport in High-Quality CVD Diamond Membranes by Multi-frequency and Multi-spot-size Time-Domain Thermoreflectance. *ACS applied materials & interfaces* (2018).

29 Moelle, C. *et al.* Measurement and calculation of the thermal expansion coefficient of diamond. *Diamond and Related Materials* **6**, 839-842 (1997).

30 Reeber, R. R. & Wang, K. Lattice parameters and thermal expansion of GaN. *Journal of Materials Research* **15**, 40-44 (2000).

31 Hancock, B. L. *et al.* Ultraviolet micro-Raman spectroscopy stress mapping of a 75-mm GaN-on-diamond wafer. *Applied Physics Letters* **108**, 211901 (2016).

32 Siddique, A. *et al.* Structure and Interface Analysis of Diamond on an AlGaN/GaN HEMT Utilizing an in Situ SiN x Interlayer Grown by MOCVD. *ACS Applied Electronic Materials* (2019).

33 Tripathy, S., Chua, S., Chen, P. & Miao, Z. Micro-Raman investigation of strain in GaN and Al x Ga 1− x N/GaN heterostructures grown on Si (111). *Journal of Applied Physics* **92**, 3503-3510 (2002).

34 Choi, S., Heller, E., Dorsey, D., Vetury, R. & Graham, S. The impact of mechanical stress on the degradation of AlGaN/GaN high electron mobility transistors. *Journal of Applied Physics* **114**, 164501 (2013).

35 Kang, B. *et al.* Effect of external strain on the conductivity of AlGaN/GaN high-electron-mobility transistors. *Applied physics letters* **83**, 4845-4847 (2003).

36 Lee, E., Zhang, T., Yoo, T., Guo, Z. & Luo, T. Nanostructures Significantly Enhance Thermal Transport across Solid Interfaces. *ACS applied materials & interfaces* **8**, 35505-35512 (2016).

37 Goodson, K., Käding, O., Rösler, M. & Zachai, R. Experimental investigation of thermal conduction normal to diamond-silicon boundaries. *Journal of Applied Physics* **77**, 1385-1392 (1995).

38 Higashiwaki, M. & Jessen, G. H. (AIP Publishing, 2018).

39 Reese, S. B., Remo, T., Green, J. & Zakutayev, A. How Much Will Gallium Oxide Power Electronics Cost? *Joule* (2019).

40 Cheng, Z. *et al.* Significantly Reduced Thermal Conductivity in Beta-(Al0. 1Ga0. 9) 2O3/Ga2O3 Superlattices. *Applied Physics Letter* **115** (2019).

41 Cahill, D. G. Analysis of heat flow in layered structures for time-domain thermoreflectance. *Review of scientific instruments* **75**, 5119-5122 (2004).

42 Schmidt, A. J. Pump-probe thermoreflectance. *Annual Review of Heat Transfer* **16** (2013).

43 Cheng, Z. *et al.* Tunable Thermal Energy Transport across Diamond Membranes and Diamond-Si Interfaces by Nanoscale Graphoepitaxy. *ACS applied materials & interfaces* (2019).

44 Jiang, P., Huang, B. & Koh, Y. K. Accurate measurements of cross-plane thermal conductivity of thin films by dual-frequency time-domain thermoreflectance (TDTR). *Review of Scientific Instruments* **87**, 075101 (2016).

45 Feser, J. P. & Cahill, D. G. Probing anisotropic heat transport using time-domain thermoreflectance with offset laser spots. *Review of Scientific Instruments* **83**, 104901 (2012).

46 Bougher, T. L. *et al.* Thermal boundary resistance in GaN films measured by time domain thermoreflectance with robust Monte Carlo uncertainty estimation. *Nanoscale and Microscale Thermophysical Engineering* **20**, 22-32 (2016).

47 Kapitza, P. The study of heat transfer in helium II. *J. Phys.(Moscow)* **4**, 181 (1941).

48 Pollack, G. L. Kapitza resistance. *Reviews of Modern Physics* **41**, 48 (1969).

49 Swartz, E. & Pohl, R. Thermal resistance at interfaces. *Applied Physics Letters* **51**, 2200-2202 (1987).

50 Swartz, E. T. & Pohl, R. O. Thermal boundary resistance. *Reviews of modern physics* **61**, 605 (1989).

51 Stoner, R. & Maris, H. Kapitza conductance and heat flow between solids at temperatures from 50 to 300 K. *Physical Review B* **48**, 16373 (1993).

52 Paddock, C. A. & Eesley, G. L. Transient thermoreflectance from thin metal films. *Journal of Applied Physics* **60**, 285-290 (1986).

53 Monachon, C., Weber, L. & Dames, C. Thermal boundary conductance: A materials science perspective. *Annual Review of Materials Research* **46**, 433-463 (2016).

54 Cola, B. A. *et al.* Photoacoustic characterization of carbon nanotube array thermal interfaces. *Journal of applied physics* **101**, 054313 (2007).

55 Wang, X. *et al.* Photoacoustic technique for thermal conductivity and thermal interface measurements. *Annual Review of Heat Transfer* **16** (2013).

56 Wasniewski, J. R. *et al.* Characterization of metallically bonded carbon nanotube-based thermal interface materials using a high accuracy 1D steady-state technique. *Journal of Electronic Packaging* **134**, 020901 (2012).

57 Dames, C. Measuring the thermal conductivity of thin films: 3 omega and related electrothermal methods. *Annual Review of Heat Transfer* **16** (2013).

58 Lee, S.-M. & Cahill, D. G. Influence of interface thermal conductance on the apparent thermal conductivity of thin films. *Microscale Thermophysical Engineering* **1**, 47-52 (1997).

59 Cahill, D. G. Heat transport in dielectric thin films and at solid-solid interfaces. *Microscale Thermophysical Engineering* **1**, 85-109 (1997).

60 Chen, Z., Jang, W., Bao, W., Lau, C. & Dames, C. Thermal contact resistance between graphene and silicon dioxide. *Applied Physics Letters* **95**, 161910 (2009).

61 Koh, Y. K., Cao, Y., Cahill, D. G. & Jena, D. Heat-Transport Mechanisms in Superlattices. *Advanced Functional Materials* **19**, 610-615 (2009).

62 Hopkins, P. E. *et al.* Effect of dislocation density on thermal boundary conductance across GaSb/GaAs interfaces. *Applied Physics Letters* **98**, 161913 (2011).

63 Losego, M. D., Blitz, I. P., Vaia, R. A., Cahill, D. G. & Braun, P. V. Ultralow thermal conductivity in organoclay nanolaminates synthesized via simple self-assembly. *Nano letters* **13**, 2215-2219 (2013).

64 Wilson, R., Apgar, B. A., Hsieh, W.-P., Martin, L. W. & Cahill, D. G. Thermal conductance of strongly bonded metal-oxide interfaces. *Physical Review B* **91**, 115414 (2015).

65 Ziade, E. *et al.* Thermal transport through GaN–SiC interfaces from 300 to 600 K. *Applied Physics Letters* **107**, 091605 (2015).

66 Schroeder, D. *et al.* Thermal resistance of transferred-silicon-nanomembrane interfaces. *Physical review letters* **115**, 256101 (2015).

67 Fong, S. *et al.* Thermal conductivity measurement of amorphous dielectric multilayers for phase-change memory power reduction. *Journal of Applied Physics* **120**, 015103 (2016).

68 Giri, A. *et al.* Heat-transport mechanisms in molecular building blocks of inorganic/organic hybrid superlattices. *Physical Review B* **93**, 115310 (2016).

69 Zheng, K. *et al.* Enhancing the thermal conductance of polymer and sapphire interface via self-assembled monolayer. *ACS nano* **10**, 7792-7798 (2016).

70 Kimling, J., Philippi-Kobs, A., Jacobsohn, J., Oepen, H. P. & Cahill, D. G. Thermal conductance of interfaces with amorphous SiO 2 measured by time-resolved magneto-optic Kerr-effect thermometry. *Physical Review B* **95**, 184305 (2017).

71 Gaskins, J. T. *et al.* Thermal Boundary Conductance Across Heteroepitaxial ZnO/GaN Interfaces: Assessment of the Phonon Gas Model. *Nano letters* **18**, 7469-7477 (2018).

72 Giri, A. *et al.* Interfacial Defect Vibrations Enhance Thermal Transport in Amorphous Multilayers with Ultrahigh Thermal Boundary Conductance. *Advanced Materials* **30**, 1804097 (2018).

73 Mu, F. *et al.* High Thermal Boundary Conductance across Bonded Heterogeneous GaN–SiC Interfaces. *ACS applied materials & interfaces* **11**, 33428-33434 (2019).

74 Cheng, Z. *et al.* Thermal conductance across β-Ga2O3-diamond van der Waals heterogeneous interfaces. *APL Materials* **7**, 031118 (2019).

75 Costescu, R. M., Wall, M. A. & Cahill, D. G. Thermal conductance of epitaxial interfaces. *Physical Review B* **67**, 054302 (2003).

76 Oh, D. W., Kim, S., Rogers, J. A., Cahill, D. G. & Sinha, S. Interfacial Thermal Conductance of Transfer-Printed Metal Films. *Advanced Materials* **23**, 5028-5033 (2011).

77 Wilson, R. & Cahill, D. G. Anisotropic failure of Fourier theory in time-domain thermoreflectance experiments. *Nature communications* **5**, 5075 (2014).

78 Liu, D., Xie, R., Yang, N., Li, B. & Thong, J. T. Profiling nanowire thermal resistance with a spatial resolution of nanometers. *Nano letters* **14**, 806-812 (2014).

79 Hohensee, G. T., Wilson, R. & Cahill, D. G. Thermal conductance of metal–diamond interfaces at high pressure. *Nature communications* **6**, 6578 (2015).

80 Ye, N. *et al.* Thermal transport across metal silicide-silicon interfaces: An experimental comparison between epitaxial and nonepitaxial interfaces. *Physical Review B* **95**, 085430 (2017).

81 Stoner, R., Maris, H., Anthony, T. & Banholzer, W. Measurements of the Kapitza conductance between diamond and several metals. *Physical Review Letters* **68**, 1563 (1992).

82 Stevens, R. J., Smith, A. N. & Norris, P. M. Measurement of thermal boundary conductance of a series of metal-dielectric interfaces by the transient thermoreflectance technique. *Journal of Heat Transfer* **127**, 315-322 (2005).

83 Ge, Z., Cahill, D. G. & Braun, P. V. Thermal conductance of hydrophilic and hydrophobic interfaces. *Physical review letters* **96**, 186101 (2006).

84 Wang, R. Y., Segalman, R. A. & Majumdar, A. Room temperature thermal conductance of alkanedithiol self-assembled monolayers. *Applied Physics Letters* **89**, 173113 (2006).

85 Lyeo, H.-K. & Cahill, D. G. Thermal conductance of interfaces between highly dissimilar materials. *Physical Review B* **73**, 144301 (2006).

86 Hopkins, P. E., Norris, P. M., Stevens, R. J., Beechem, T. E. & Graham, S. Influence of interfacial mixing on thermal boundary conductance across a chromium/silicon interface. *Journal of Heat Transfer* **130**, 062402 (2008).

87 Hopkins, P. E., Norris, P. M. & Stevens, R. J. Influence of inelastic scattering at metal-dielectric interfaces. *Journal of Heat Transfer* **130**, 022401 (2008).

88 Hanisch, A., Krenzer, B., Pelka, T., Möllenbeck, S. & Horn-von Hoegen, M. Thermal response of epitaxial thin Bi films on Si (001) upon femtosecond laser excitation studied by ultrafast electron diffraction. *Physical Review B* **77**, 125410 (2008).

89 Schmidt, A. J., Collins, K. C., Minnich, A. J. & Chen, G. Thermal conductance and phonon transmissivity of metal–graphite interfaces. *Journal of Applied Physics* **107**, 104907 (2010).

90 Collins, K. C., Chen, S. & Chen, G. Effects of surface chemistry on thermal conductance at aluminum–diamond interfaces. *Applied Physics Letters* **97**, 083102 (2010).

91 Hsieh, W.-P., Lyons, A. S., Pop, E., Keblinski, P. & Cahill, D. G. Pressure tuning of the thermal conductance of weak interfaces. *Physical Review B* **84**, 184107 (2011).

92 Duda, J. C. & Hopkins, P. E. Systematically controlling Kapitza conductance via chemical etching. *Applied Physics Letters* **100**, 111602 (2012).

93 Hopkins, P. E. *et al.* Manipulating thermal conductance at metal–graphene contacts via chemical functionalization. *Nano letters* **12**, 590-595 (2012).

94 Losego, M. D., Grady, M. E., Sottos, N. R., Cahill, D. G. & Braun, P. V. Effects of chemical bonding on heat transport across interfaces. *Nature materials* **11**, 502-506 (2012).

95 O'Brien, P. J. *et al.* Bonding-induced thermal conductance enhancement at inorganic heterointerfaces using nanomolecular monolayers. *Nature materials* **12**, 118-122 (2013).

96 Monachon, C. & Weber, L. Influence of diamond surface termination on thermal boundary conductance between Al and diamond. *Journal of Applied Physics* **113**, 183504 (2013).

97 Duda, J. *et al.* Influence of interfacial properties on thermal transport at gold: silicon contacts. *Applied Physics Letters* **102**, 081902 (2013).

98 Monachon, C. & Weber, L. Thermal boundary conductance between refractory metal carbides and diamond. *Acta Materialia* **73**, 337-346 (2014).

99 Sun, F. *et al.* Molecular Bridge Enables Anomalous Enhancement in Thermal Transport across Hard-Soft Material Interfaces. *Advanced Materials* **26**, 6093-6099 (2014).

100 Freedman, J. P., Yu, X., Davis, R. F., Gellman, A. J. & Malen, J. A. Thermal interface conductance across metal alloy–dielectric interfaces. *Physical Review B* **93**, 035309 (2016).

101 Hua, C., Chen, X., Ravichandran, N. K. & Minnich, A. J. Experimental metrology to obtain thermal phonon transmission coefficients at solid interfaces. *Physical Review B* **95**, 205423 (2017).

102 Saha, D. *et al.* Impact of metal adhesion layer diffusion on thermal interface conductance. *Physical Review B* **99**, 115418 (2019).

103 Gundrum, B. C., Cahill, D. G. & Averback, R. S. Thermal conductance of metal-metal interfaces. *Physical Review B* **72**, 245426 (2005).

104 Wilson, R. & Cahill, D. G. Experimental validation of the interfacial form of the Wiedemann-Franz law. *Physical review letters* **108**, 255901 (2012).

105 Jiang, P., Qian, X. & Yang, R. Tutorial: Time-domain thermoreflectance (TDTR) for thermal property characterization of bulk and thin film materials. *Journal of Applied Physics* **124**, 161103 (2018).

106 Yuan, C., Pomeroy, J. W. & Kuball, M. Above bandgap thermoreflectance for non-invasive thermal characterization of GaN-based wafers. *Applied Physics Letters* **113**, 102101 (2018).

107 Braun, J. L. & Hopkins, P. E. Upper limit to the thermal penetration depth during modulated heating of multilayer thin films with pulsed and continuous wave lasers: A numerical study. *Journal of Applied Physics* **121**, 175107 (2017).

108 Kothari, K., Malhotra, A. & Maldovan, M. Unconventional thermal transport in thin film-on-substrate systems. *Journal of Physics D: Applied Physics* **51**, 365302 (2018).

109 Malhotra, A., Kothari, K. & Maldovan, M. Enhancing Thermal Transport in Layered Nanomaterials. *Scientific Reports* **8**, 1880 (2018).

110 Mu, F. *et al.* A comparison study: Direct wafer bonding of SiC–SiC by standard surface-activated bonding and modified surface-activated bonding with Si-containing Ar ion beam. *Applied Physics Express* **9**, 081302 (2016).

111 Plößl, A. & Kräuter, G. Wafer direct bonding: tailoring adhesion between brittle materials. *Materials Science and Engineering: R: Reports* **25**, 1-88 (1999).

112 Won, Y., Cho, J., Agonafer, D., Asheghi, M. & Goodson, K. E. Fundamental cooling limits for high power density gallium nitride electronics. *IEEE Transactions on Components, Packaging and Manufacturing Technology* **5**, 737-744 (2015).

113 Liu, T. *et al.* 3-inch GaN-on-diamond HEMTs with device-first transfer technology. *IEEE Electron Device Letters* **38**, 1417-1420 (2017).

114 Ohki, T. *et al.* An Over 20-W/mm S-Band InAlGaN/GaN HEMT With SiC/Diamond-Bonded Heat Spreader. *IEEE Electron Device Letters* **40**, 287-290 (2018).

115 Yates, L. *et al.* Low Thermal Boundary Resistance Interfaces for GaN-on-Diamond Devices. *ACS applied materials & interfaces* **10**, 24302-24309 (2018).

116 Tadjer, M. J. *et al.* GaN-On-Diamond HEMT Technology With T AVG= 176° C at P DC, max= 56 W/mm Measured by Transient Thermoreflectance Imaging. *IEEE Electron Device Letters* **40**, 881-884 (2019).

117 Sun, H. *et al.* Temperature-dependent thermal resistance of GaN-on-diamond HEMT wafers. *IEEE Electron Device Letters* **37**, 621-624 (2016).

118 Hines, N. J. *Advanced Solutions for Thermal Management and Reliability of Gallium Nitride-Based High Electron Mobility Transistors on Diamond Substrates*, Georgia Institute of Technology, (2019).

119 Ahmad, I., Holtz, M., Faleev, N. & Temkin, H. Dependence of the stress–temperature coefficient on dislocation density in epitaxial GaN grown on α-Al 2 O 3 and 6H–SiC substrates. *Journal of applied physics* **95**, 1692-1697 (2004).

120 Cho, J. *et al.* Improved thermal interfaces of GaN–diamond composite substrates for HEMT applications. *IEEE Transactions on Components, Packaging and Manufacturing Technology* **3**, 79-85 (2012).

121 Francis, D. *et al.* Formation and characterization of 4-inch GaN-on-diamond substrates. *Diamond and Related Materials* **19**, 229-233 (2010).

122 Chao, P.-C. *et al.* Low-temperature bonded GaN-on-diamond HEMTs with 11 W/mm output power at 10 GHz. *IEEE Transactions on Electron Devices* **62**, 3658-3664 (2015).

123 Mu, F., He, R. & Suga, T. Room temperature GaN-diamond bonding for high-power GaN-on-diamond devices. *Scripta Materialia* **150**, 148-151 (2018).

124 Zheng, Q. *et al.* Thermal conductivity of GaN, GaN 71, and SiC from 150 K to 850 K. *Physical Review Materials* **3**, 014601 (2019).

125 Hohensee, G. T., Hsieh, W.-P., Losego, M. D. & Cahill, D. G. Interpreting picosecond acoustics in the case of low interface stiffness. *Review of Scientific Instruments* **83**, 114902 (2012).

126 Ward, A., Broido, D., Stewart, D. A. & Deinzer, G. Ab initio theory of the lattice thermal conductivity in diamond. *Physical Review B* **80**, 125203 (2009).

127 Inyushkin, A. *et al.* Thermal conductivity of high purity synthetic single crystal diamonds. *Physical Review B* **97**, 144305 (2018).

128 Lindsay, L., Broido, D. & Reinecke, T. Thermal conductivity and large isotope effect in GaN from first principles. *Physical review letters* **109**, 095901 (2012).

129 Simon, R. B., Anaya, J. & Kuball, M. Thermal conductivity of bulk GaN—Effects of oxygen, magnesium doping, and strain field compensation. *Applied Physics Letters* **105**, 202105 (2014).

130 Ziade, E. *et al.* Thickness dependent thermal conductivity of gallium nitride. *Applied Physics Letters* **110**, 031903 (2017).

131 Kazan, M. Interpolation between the acoustic mismatch model and the diffuse mismatch model for the interface thermal conductance: Application to inn/gan superlattice. *Journal of heat transfer* **133**, 112401 (2011).

132 Roder, C., Einfeldt, S., Figge, S. & Hommel, D. Temperature dependence of the thermal expansion of GaN. *Physical Review B* **72**, 085218 (2005).

133 Lee, E. & Luo, T. The role of optical phonons in intermediate layer-mediated thermal transport across solid interfaces. *Physical Chemistry Chemical Physics* **19**, 18407-18415 (2017).

134 Zhou, Y. *et al.* Barrier-Layer Optimization for Enhanced GaN-on-Diamond Device Cooling. *ACS Applied Materials & Interfaces* **9**, 34416-34422 (2017).

135 Bagnall, K. R., Muzychka, Y. S. & Wang, E. N. Analytical solution for temperature rise in complex multilayer structures with discrete heat sources. *IEEE Transactions on Components, Packaging and Manufacturing Technology* **4**, 817-830 (2014).

136 Cho, J., Li, Z., Asheghi, M. & Goodson, K. E. Near-junction thermal management: Thermal conduction in gallium nitride composite substrates. *Annual Review of Heat Transfer* **18** (2015).

137 Dumka, D. *et al.* in *2013 IEEE Compound Semiconductor Integrated Circuit Symposium (CSICS).* 1-4 (IEEE).

138 Cho, J., Won, Y., Francis, D., Asheghi, M. & Goodson, K. E. in *2014 IEEE Compound Semiconductor Integrated Circuit Symposium (CSICS).* 1-4 (IEEE).

139 Sun, H. *et al.* Reducing GaN-on-diamond interfacial thermal resistance for high power transistor applications. *Applied Physics Letters* **106**, 111906 (2015).

140 Cho, J., Francis, D., Altman, D. H., Asheghi, M. & Goodson, K. E. Phonon conduction in GaN-diamond composite substrates. *Journal of Applied Physics* **121**, 055105 (2017).

141 Cahill, D. G. *et al.* Nanoscale thermal transport. II. 2003–2012. *Applied Physics Reviews* **1**, 011305 (2014).

142 Moore, A. L. & Shi, L. Emerging challenges and materials for thermal management of electronics. *Materials Today* **17**, 163-174 (2014).

143 Pop, E. Energy dissipation and transport in nanoscale devices. *Nano Research* **3**, 147-169 (2010).

144 Majumdar, S. *et al.* Vibrational mismatch of metal leads controls thermal conductance of self-assembled monolayer junctions. *Nano letters* **15**, 2985-2991 (2015).

145 Hu, M., Zhang, X., Poulikakos, D. & Grigoropoulos, C. P. Large "near junction" thermal resistance reduction in electronics by interface nanoengineering. *International Journal of Heat and Mass Transfer* **54**, 5183-5191 (2011).

146 Zhou, X. W., Jones, R. E., Kimmer, C. J., Duda, J. C. & Hopkins, P. E. Relationship of thermal boundary conductance to structure from an analytical model plus molecular dynamics simulations. *Physical Review B* **87**, 094303 (2013).

147 Lee, E., Zhang, T., Hu, M. & Luo, T. Thermal boundary conductance enhancement using experimentally achievable nanostructured interfaces–analytical study combined with molecular dynamics simulation. *Physical Chemistry Chemical Physics* **18**, 16794-16801 (2016).

148 Hopkins, P. E., Duda, J. C., Petz, C. W. & Floro, J. A. Controlling thermal conductance through quantum dot roughening at interfaces. *Physical Review B* **84**, 035438 (2011).

149 Smith, H. I. & Flanders, D. Oriented crystal growth on amorphous substrates using artificial surface-relief gratings. *Applied Physics Letters* **32**, 349-350 (1978).

150 Geis, M., Tsaur, B. Y. & Flanders, D. Graphoepitaxy of germanium on gratings with square-wave and sawtooth profiles. *Applied Physics Letters* **41**, 526-529 (1982).

151 Geis, M., Flanders, D., Antoniadis, D. & Smith, H. in *Electron Devices Meeting, 1979 Internationa.* 210-212 (IEEE).

152 Geis, M., Flanders, D. & Smith, H. I. Crystallographic orientation of silicon on an amorphous substrate using an artificial surface-relief grating and laser crystallization. *Applied Physics Letters* **35**, 71-74 (1979).

153 Segalman, R. A., Yokoyama, H. & Kramer, E. J. Graphoepitaxy of spherical domain block copolymer films. *Advanced Materials* **13**, 1152-1155 (2001).

154 Bita, I. *et al.* Graphoepitaxy of self-assembled block copolymers on two-dimensional periodic patterned templates. *Science* **321**, 939-943 (2008).

155 Ismach, A., Kantorovich, D. & Joselevich, E. Carbon nanotube graphoepitaxy: Highly oriented growth by faceted nanosteps. *Journal of the American Chemical Society* **127**, 11554-11555 (2005).

156 Liu, J. *et al.* Simultaneous measurement of thermal conductivity and heat capacity of bulk and thin film materials using frequency-dependent transient thermoreflectance method. *Review of Scientific Instruments* **84**, 034902 (2013).

157 Daly, B., Kang, K., Wang, Y. & Cahill, D. G. Picosecond ultrasonic measurements of attenuation of longitudinal acoustic phonons in silicon. *Physical Review B* **80**, 174112 (2009).

158 Asheghi, M., Touzelbaev, M., Goodson, K., Leung, Y. & Wong, S. Temperature-dependent thermal conductivity of single-crystal silicon layers in SOI substrates. *Journal of Heat Transfer* **120**, 30-36 (1998).

159 Plimpton, S. Fast parallel algorithms for short-range molecular dynamics. *Journal of computational physics* **117**, 1-19 (1995).

160 Baskes, M., Nelson, J. & Wright, A. Semiempirical modified embedded-atom potentials for silicon and germanium. *Physical Review B* **40**, 6085 (1989).

161 Landauer, R. Spatial variation of currents and fields due to localized scatterers in metallic conduction. *IBM Journal of Research and Development* **1**, 223-231 (1957).

162 Little, W. The transport of heat between dissimilar solids at low temperatures. *Canadian Journal of Physics* **37**, 334-349 (1959).

163 Fisher, T. S. *Thermal energy at the nanoscale*. Vol. 3 (World Scientific Publishing Company, 2013).

164 Cheng, Z. *et al.* Thermal Conductance across beta-Ga2O3-diamond Van der Waals Heterogeneous Interfaces. *arXiv preprint arXiv:1901.02961* (2019).

165 Giri, A. & Hopkins, P. E. Role of interfacial mode coupling of optical phonons on thermal boundary conductance. *Scientific reports* **7**, 11011 (2017).

166 Murakami, T., Hori, T., Shiga, T. & Shiomi, J. Probing and tuning inelastic phonon conductance across finite-thickness interface. *Applied Physics Express* **7**, 121801 (2014).

167 Gordiz, K. & Henry, A. Phonon transport at interfaces: Determining the correct modes of vibration. *Journal of Applied Physics* **119**, 015101 (2016).

168 Gordiz, K. & Henry, A. Phonon transport at crystalline Si/Ge interfaces: the role of interfacial modes of vibration. *Scientific reports* **6**, 23139 (2016).

169 Kittel, C. *Introduction to solid state physics*. (Wiley, 2005).

170 Liu, Z.-K., Wang, Y. & Shang, S. Thermal expansion anomaly regulated by entropy. *Scientific reports* **4** (2014).

171 Wang, Y. *et al.* A mixed-space approach to first-principles calculations of phonon frequencies for polar materials. *Journal of Physics: Condensed Matter* **22**, 202201 (2010).

172 Goodson, K., Käding, O., Rösner, M. & Zachai, R. Thermal conduction normal to diamond-silicon boundaries. *Applied physics letters* **66**, 3134-3136 (1995).

173 Mohr, M. *et al.* Influence of grain boundaries on elasticity and thermal conductivity of nanocrystalline diamond films. *Acta Materialia* **122**, 92-98 (2017).

174 Khosravian, N. *et al.* Molecular dynamic simulation of diamond/silicon interfacial thermal conductance. *Journal of Applied Physics* **113**, 024907 (2013).

175 Gordiz, K. & Henry, A. Phonon transport at interfaces between different phases of silicon and germanium. *Journal of Applied Physics* **121**, 025102 (2017).

176 Chalopin, Y. & Volz, S. A microscopic formulation of the phonon transmission at the nanoscale. *Applied Physics Letters* **103**, 051602 (2013).

177 Feng, T., Zhong, Y., Shi, J. & Ruan, X. Unexpected high inelastic phonon transport across solid-solid interface: Modal nonequilibrium molecular dynamics simulations and Landauer analysis. *Physical Review B* **99**, 045301 (2019).

178 Sood, A. *et al.* Direct Visualization of Thermal Conductivity Suppression Due to Enhanced Phonon Scattering Near Individual Grain Boundaries. *Nano letters* (2018).

179 Gu, C., Jiang, X. & Jin, Z. The preparation of high quality oriented diamond thin films via low temperature and hydrogen ion etched nucleation. *Diamond and related materials* **8**, 262-266 (1999).

180 Liu, T., Raabe, D. & Mao, W.-M. A review of crystallographic textures in chemical vapor-deposited diamond films. *Frontiers of Materials Science in China* **4**, 1-16 (2010).

181 Smereka, P., Li, X., Russo, G. & Srolovitz, D. J. Simulation of faceted film growth in three dimensions: microstructure, morphology and texture. *Acta Materialia* **53**, 1191-1204 (2005).

182 Dong, H., Wen, B. & Melnik, R. Relative importance of grain boundaries and size effects in thermal conductivity of nanocrystalline materials. *Scientific reports* **4**, 7037 (2014).

183 Jiang, P., Qian, X., Li, X. & Yang, R. Three-dimensional anisotropic thermal conductivity tensor of single crystalline β-Ga2O3. *Applied Physics Letters* **113**, 232105 (2018).

184 Krishnamoorthy, S. *et al.* Modulation-doped β-(Al0. 2Ga0. 8) 2O3/Ga2O3 field-effect transistor. *Applied Physics Letters* **111**, 023502 (2017).

185 Zhang, Y. *et al.* Demonstration of high mobility and quantum transport in modulation-doped β-(AlxGa1-x) 2O3/Ga2O3 heterostructures. *Applied Physics Letters* **112**, 173502 (2018).

186 Ahmadi, E. *et al.* Demonstration of β-(Al x Ga1− x) 2O3/β-Ga2O3 modulation doped field-effect transistors with Ge as dopant grown via plasma-assisted molecular beam epitaxy. *Applied Physics Express* **10**, 071101 (2017).

187 Oshima, T. *et al.* Carrier confinement observed at modulation-doped β-(Al x Ga1− x) 2O3/Ga2O3 heterojunction interface. *Applied Physics Express* **10**, 035701 (2017).

188 Zhang, Y. *et al.* Demonstration of β-(AlxGa1-x) 2O3/Ga2O3 double heterostructure field effect transistors. *Applied Physics Letters* **112**, 233503 (2018).

189 Cheng, Z. *et al.* Enhancing Heat Transport across Chemical-vapor-deposited Diamond-Si Interfaces by Nanoscale Patterning. *arXiv preprint arXiv:1807.11400* (2018).

190 Cheng, Z. *et al.* Diffuson-driven ultralow thermal conductivity in amorphous N b 2 O 5 thin films. *Physical Review Materials* **3**, 025002 (2019).

191 Chavez-Angel, E. *et al.* Subamorphous thermal conductivity of crystalline half-Heusler superlattices. *Nanoscale and Microscale Thermophysical Engineering* **23**, 1-9 (2019).

192 Guo, Z. *et al.* Anisotropic thermal conductivity in single crystal β-gallium oxide. *Applied Physics Letters* **106**, 111909 (2015).

193 Santia, M. D., Tandon, N. & Albrecht, J. Lattice thermal conductivity in β-Ga 2 O 3 from first principles. *Applied Physics Letters* **107**, 041907 (2015).

194 Liu, J., Xu, Z., Cheng, Z., Xu, S. & Wang, X. Thermal Conductivity of Ultra-high Molecular Weight Polyethylene Crystal: Defect-effect Uncovered by 0 K limit Phonon Diffusion. *ACS applied materials & interfaces* (2015).

195 Cheng, Z., Liu, L., Xu, S., Lu, M. & Wang, X. Temperature dependence of electrical and thermal conduction in single silver nanowire. *Scientific reports* **5** (2015).

196 Martin, P., Aksamija, Z., Pop, E. & Ravaioli, U. Impact of phonon-surface roughness scattering on thermal conductivity of thin Si nanowires. *Physical review letters* **102**, 125503 (2009).

197 Wang, Z., Alaniz, J. E., Jang, W., Garay, J. E. & Dames, C. Thermal conductivity of nanocrystalline silicon: importance of grain size and frequency-dependent mean free paths. *Nano letters* **11**, 2206-2213 (2011).

198 Jiang, P., Qian, X., Li, X. & Yang, R. Three-Dimensional Anisotropic Thermal Conductivity Tensor of Single Crystalline\b {eta}-Ga2O3. *arXiv preprint arXiv:1809.04762* (2018).

199 Yates, L. *et al.* in *ASME 2017 International Technical Conference and Exhibition on Packaging and Integration of Electronic and Photonic Microsystems collocated with the ASME 2017 Conference on Information Storage and Processing Systems.* V001T004A014-V001T004A014 (American Society of Mechanical Engineers).

200 Hwang, W. S. *et al.* High-voltage field effect transistors with wide-bandgap β-Ga2O3 nanomembranes. *Applied Physics Letters* **104**, 203111 (2014).

201 Mitdank, R. *et al.* Temperature-dependent electrical characterization of exfoliated β-Ga2O3 micro flakes. *physica status solidi (a)* **211**, 543-549 (2014).

202 Ahn, S. *et al.* Effect of front and back gates on β-Ga2O3 nano-belt field-effect transistors. *Applied Physics Letters* **109**, 062102 (2016).

203 Zhou, H., Maize, K., Qiu, G., Shakouri, A. & Ye, P. D. β-Ga2O3 on insulator field-effect transistors with drain currents exceeding 1.5 A/mm and their self-heating effect. *Applied Physics Letters* **111**, 092102 (2017).

204 Zhou, H. *et al.* High-performance depletion/enhancement-mode β-Ga2O3 on insulator (GOOI) field-effect transistors with record drain currents of 600/450 mA/mm. *IEEE Electron Device Lett* **38**, 103-106 (2017).

205 Kim, J., Mastro, M. A., Tadjer, M. J. & Kim, J. Heterostructure WSe2− Ga2O3 Junction Field-Effect Transistor for Low-Dimensional High-Power Electronics. *ACS applied materials & interfaces* **10**, 29724-29729 (2018).

206 Noh, J., Si, M., Zhou, H., Tadjer, M. J. & Peide, D. Y. in *2018 76th Device Research Conference (DRC)*. 1-2 (IEEE).

207 Song, W.-B., Sutton, M. S. & Talghader, J. J. Thermal contact conductance of actuated interfaces. *Applied physics letters* **81**, 1216-1218 (2002).

208 Cho, J., Richards, C., Bahr, D., Jiao, J. & Richards, R. Evaluation of contacts for a MEMS thermal switch. *Journal of Micromechanics and Microengineering* **18**, 105012 (2008).

209 Grimm, D. *et al.* Thermal conductivity of mechanically joined semiconducting/metal nanomembrane superlattices. *Nano letters* **14**, 2387-2393 (2014).

210 Huxtable, S. T., Cahill, D. G. & Phinney, L. M. Thermal contact conductance of adhered microcantilevers. *Journal of applied physics* **95**, 2102-2108 (2004).

211 Seong, M., Singh, P. & Sinha, S. Area of contact and thermal transport across transfer-printed metal-dielectric interfaces. *Journal of Applied Physics* **113**, 024321 (2013).

212 Yang, J. *et al.* Enhanced and switchable nanoscale thermal conduction due to van der Waals interfaces. *Nature Nanotechnology* **7**, 91 (2012).

213 Caldwell, J. D. *et al.* Technique for the dry transfer of epitaxial graphene onto arbitrary substrates. *ACS nano* **4**, 1108-1114 (2010).

214 Wilson, R. & Cahill, D. G. Limits to Fourier theory in high thermal conductivity single crystals. *Applied Physics Letters* **107**, 203112 (2015).

215 Oh, S., Kim, J., Ren, F., Pearton, S. J. & Kim, J. Quasi-two-dimensional β-gallium oxide solar-blind photodetectors with ultrahigh responsivity. *Journal of Materials Chemistry C* **4**, 9245-9250 (2016).

216 Oh, S., Mastro, M. A., Tadjer, M. J. & Kim, J. Solar-blind metal-semiconductor-metal photodetectors based on an exfoliated β-Ga2O3 micro-flake. *ECS Journal of Solid State Science and Technology* **6**, Q79-Q83 (2017).

217 Shi, J., Dong, Y., Fisher, T. & Ruan, X. Thermal transport across carbon nanotube-graphene covalent and van der Waals junctions. *Journal of Applied Physics* **118**, 044302 (2015).

218 Fu, H. *et al.* A Comparative Study on the Electrical Properties of Vertical ($\bar {\sf2} 01$) and (010) $\beta $-Ga 2 O 3 Schottky Barrier Diodes on EFG Single-Crystal Substrates. *IEEE Transactions on Electron Devices* **65**, 3507-3513 (2018).

219 Blumenschein, N. *et al.* in *Oxide-based Materials and Devices IX*.

220 Kresse, G. G. Kresse and J. Furthmüller, Phys. Rev. B 54, 11169 (1996). *Phys. Rev. B* **54**, 11169 (1996).

221 Jain, A. *et al.* Commentary: The Materials Project: A materials genome approach to accelerating materials innovation. *Apl Materials* **1**, 011002 (2013).

222 Petretto, G. *et al.* High-throughput density-functional perturbation theory phonons for inorganic materials. *Scientific data* **5**, 180065 (2018).

223 Monachon, C. Thermal boundary conductance between metals and dielectrics. (EPFL, 2013).

224 Gaskins, J. T. *et al.* Thermal boundary conductance across epitaxial ZnO/GaN interfaces: Assessment of phonon gas models and atomistic Green's function approaches for predicting interfacial phonon transport. *arXiv preprint arXiv:1710.09525* (2017).